NUMERICAL ANALYSIS OF THE DYNAMICS OF NONLINEAR SOLIDS AND STRUCTURES

by

F. ARMERO
University of California at Berkeley
Structural Engineering, Mechanics, and Materials
Department of Civil and Environmental Engineering
713 Davis Hall, Berkeley, CA 94720
Phone: (510)-643 0813 FAX: (510)-643 8928
e-mail: armero@ce.berkeley.edu

Final Report

August 2008

Research supported by the AFOSR under grant
no. FA9550-05-1-0117 with UC Berkeley

The Air Force Office of Scientific Research
Computational Mathematics Program
Dr. Fariba Fahroo
Program Manager
AFOSR/NL
875 North Randolph Street
Suite 325, Room 3112
Arlington, VA 22203

Table of Contents

NUMERICAL ANALYSIS OF THE DYNAMICS OF NONLINEAR SOLIDS AND STRUCTURES

by

F. ARMERO
Structural Engineering, Mechanics, and Materials
Department of Civil and Environmental Engineering
University of California, Berkeley CA 94720

Final Report, August 2008

Research supported by the AFOSR under grant
no. FA9550-05-1-0117 with UC Berkeley

Abstract

This report presents a summary of the research supported by the AFOSR during the period February 1 2005 to May 31 2008 on the formulation and analysis of integration algorithms for the nonlinear dynamics of solids and structures. The project's main focus has been the development of energy-dissipative momentum-conserving time-stepping algorithms (or, in short, EDMC schemes) for finite strain plasticity and nonlinear coupled thermoelasticity. These schemes lead to numerical solutions that exhibit exactly, by design, the conservation laws of linear and angular momenta, as well as the exact physical dissipation characteristic of these inelastic systems. This latter property leads to a much improved numerical stability when compared with classical schemes, avoiding in particular their observed numerical instabilities in the nonlinear range. The design of the new algorithms is based on a complete mathematical analysis of the discrete dynamical system, with the above conservation/dissipation properties incorporated and proven rigorously and for general models and conditions (e.g. independent of the time step). In addition, the observation of the crucial role also played by the spatial discretization has led to the development of new locking-free assumed strain finite element methods for the implementation of energy-momentum schemes.

KEYWORDS: nonlinear dynamics, energy-dissipative momentum-conserving algorithms, finite strain plasticity, nonlinear coupled thermoelasticity, assumed strain finite element methods.

1. Objectives

The research considered in this grant addressed different aspects of the numerical analysis of the dynamics of nonlinear solids and structures. The main goal was the development of stable time-stepping algorithms for nonlinear dynamics. The focus was on inelastic solids, including finite strain elastoplastic and coupled nonlinear thermomelastic models of three-dimensional solids and of structures (like shells). In addition, the project has considered the first steps in the extension of these ideas to the modeling of failure in solids and structures in the dynamic range, through the consideration of finite elements that incorporate strong discontinuities for the modeling of cracks and other similar localized solutions.

This effort significantly extended the range of application of the methods that we have developed previously with the support of the AFOSR for elastic problems. In this way, the main goal can be summarized as the development of time-stepping algorithms that rigorously exhibit the non-negative energy dissipation characteristic of these inelastic systems, while preserving the conservation laws of linear and angular momentum and the associated relative equilibria of the dynamical system. Existing classical techniques were developed in the context of linear problems and do not exhibit these crucial properties when employed in nonlinear applications. In fact, classical time-stepping algorithms (like New mark schemes and their variations) have been observed to numerical instabilities in the nonlinear range. These instabilities are characterized by an unbounded growth of the energy in finite time, despite the dissipative character of the underlying physical systems under consideration. This situation clearly identifies the need for new and improved numerical algorithms, motivating the developments considered in this project.

The completely different nature of inelastic problems, involving the additional set of plastic/damage evolution equations (usually of a unilaterally constrained character due to the presence of the so-called yield/damage surface condition), required the development of new ideas and schemes beyond the ones available for the elastic case. Our approach in addressing these challenges can be summarized in the actual analysis of the discrete equations driving the design of the new numerical schemes, and the exact incorporation (by design) in the discrete system of the energy-momentum response of the underlying physical system. In this way, the rigorous proof of all the conservation/dissipation properties for general material models, accounting also for the finite element interpolation of the governing equations, provides the robustness required to the computational tools for the analysis of the complex practical applications of interest to the Air Force. In this respect, we note that the mathematical analyses of the algorithms identified the need to develop new assumed strain finite element methods that conformed with the dissipative/conservation properties of the temporal approximation. This situation identified a new objective of the project, also successfully achieved.

The improved stability properties of the newly developed integration algorithms are then

supported by rigorous mathematical analyses of the discrete dynamical systems that they generate. We also have given a special attention to the actual implementation of the new algorithms in the context of the finite element method. The combination of all these results has led to powerful novel computational tools, with the sound theoretical basis necessary for the analysis of the complex practical problems of interest to the Air Force.

2. Brief Description of the Accomplishments

The major results accomplished under this project can be summarized as follows:

1. *Energy-dissipative, momentum-conserving algorithms (EDMC schemes) for finite strain multiplicative plasticity.* Continuing with preliminary results of a previous AFOSR research effort, we have developed new integration algorithms for finite strain plasticity that incorporate the characteristic (and critical) property of non-negative energy dissipation in the discrete system, while inheriting also the conservation laws of linear and angular momenta. The construction of the new algorithms makes a crucial use of the arguments employed in the characterization of the the physical and mathematical properties of the continuum model, in the context of modern treatments based on a multiplicative decomposition of the deformation gradient in an elastic and plastic part. The resulting scheme conserves exactly both the linear and angular momenta, and provides the exact physical dissipation predicted by the model, including the exact energy conservation for an elastic step. This leads not only to physically better numerical results, but also to more numerically stable simulations. This improved numerical stability is to be contrasted with the numerical instabilities observed by existing schemes in this strongly nonlinear problem, even with its physically dissipative character. These results appeared in [1,2]† .

2. *Volume-preserving energy-momentum schemes for isochoric plastic models.* Several important applications of elastoplastic models (namely, metals) exhibit an isochoric plastic response, that is, there is no plastic change of volume. This response is a very characteristic physical property of these materials and, as such, crucial to reproduce in the actual numerical simulations. This physical property translates in a very rich geometric structure of the aforementioned multiplicative elastoplastic models, with a key role played by the elastic metric in the intermediate configuration defined by the plastic part of the deformation gradient. We have developed a new time-stepping approximation of this geometric structure that, when combined with the developments summarized above for general elastoplastic models, results in a volume preserving scheme that also exhibits the exact non-negative energy dissipation and momentum conservation laws of the underlying physical system. The improved numerical stability comes then with the added benefit of reproducing the plastic isochoric response of interest. The new algorithm defines a new approximation

† The numbering of the references follows the list of publications presented below in page 14 of this report.

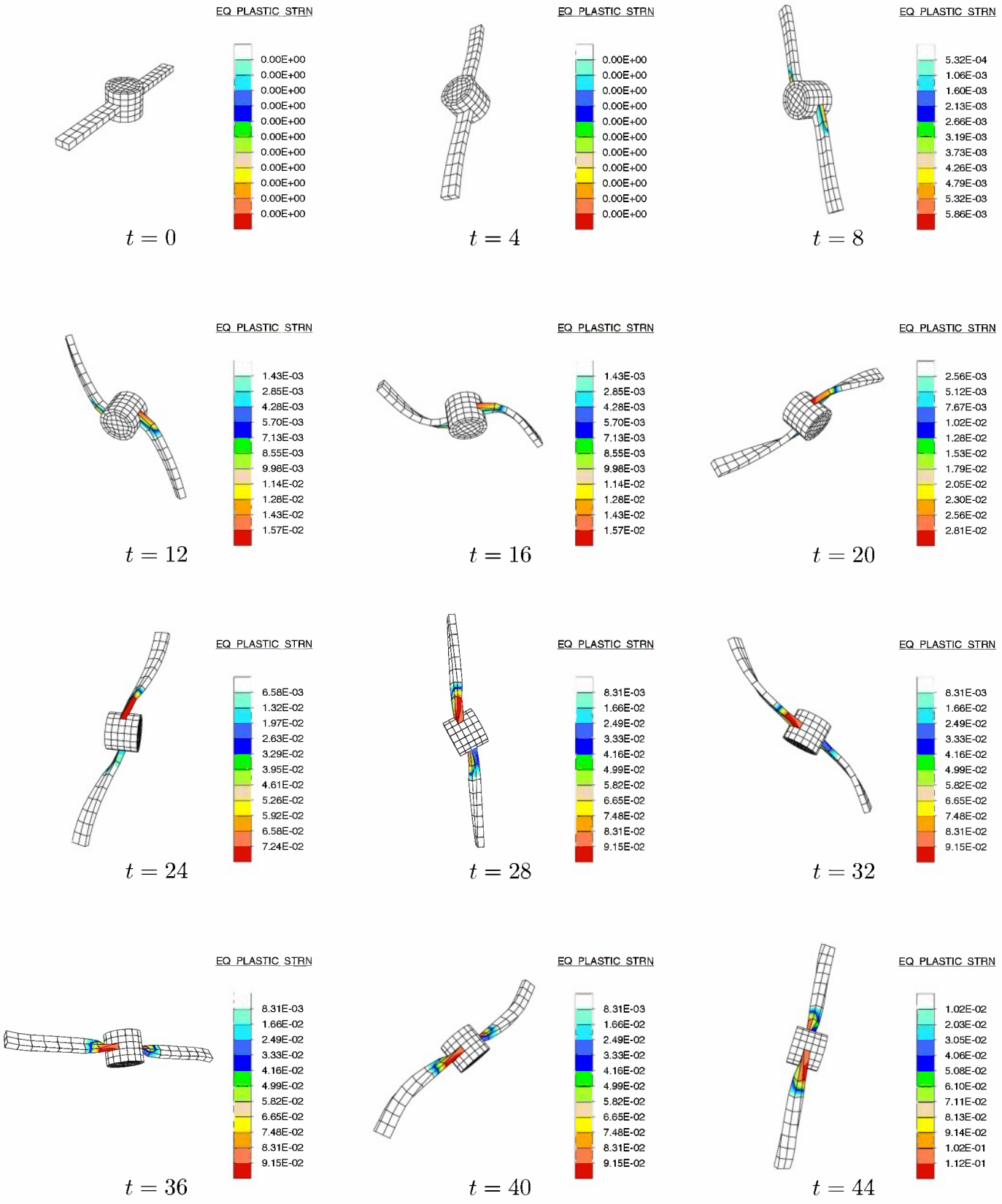

FIGURE 2.1 Three-dimensional elastoplastic solid in free flight. Sequence of deformations in the early stages of the motion with the spatial distribution of the equivalent plastic strain. Solution obtained with the new EDMC scheme.

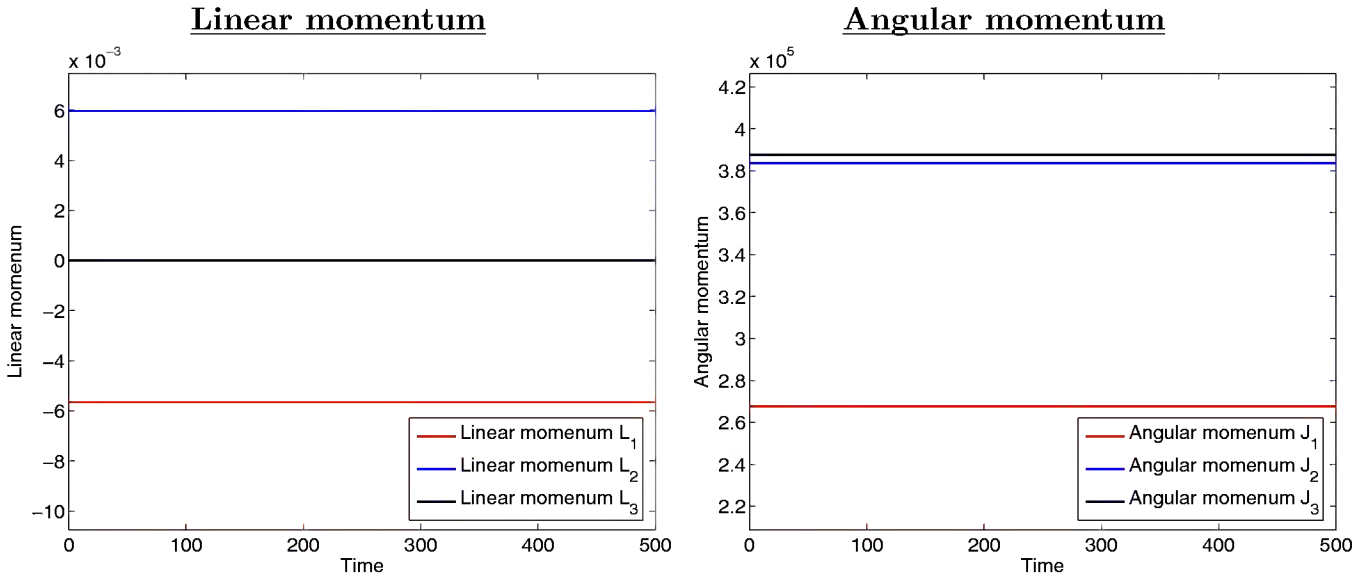

FIGURE 2.2 Three-dimensional elastoplastic solid in free flight. Temporal evolutions of the the three components of the linear momentum (left) and the angular momentum (right) for the solution obtained with the new EDMC scheme, showing the exact conservation of all these quantities. They correspond exactly to the momenta associated with the assumed initial velocities for the assumed undeformed initial configuration.

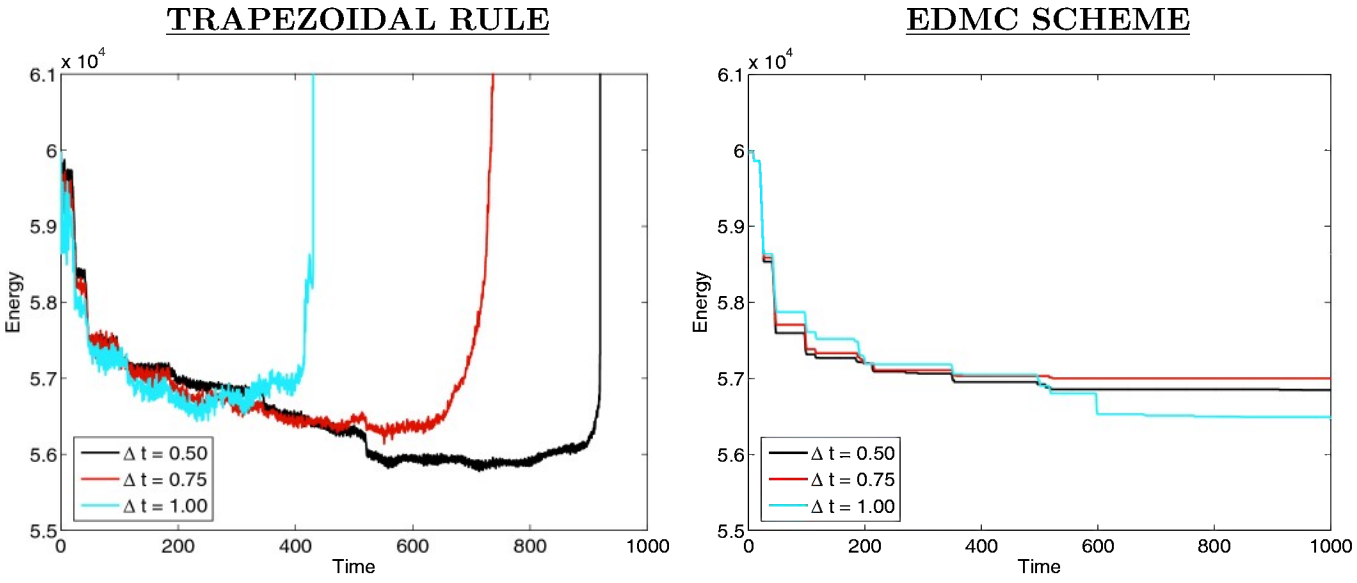

FIGURE 2.3 Three-dimensional elastoplastic solid in free flight. Temporal evolutions of the total energy obtained by the trapezoidal rule (left) and EDMC scheme (right) for different time step. The non-negative energy dissipative character of the new EDMC scheme is to be contrasted with the persistent energy growth observed with the trapezoidal rule leading to the termination of the simulation for a lack of convergence of the Newton-Raphson scheme used in the solution process.

of the aforementioned geometric structure that controls the volumetric strain. The new algorithm is second order accurate in time, as desired.

Figures 2.1, 2.2 and 2.3 illustrate these developments. They show the solution obtained in the modeling of the free flight of a three-dimensional solid consisting of a very stiff elastic cylindrical core and two flexible arms made of an elastoplastic material modeled with J_2-flow theory of finite strain plasticity following the classical Mises yield function. The elastic response is based on Hencky's hyperelastic potential on the logarithmic elastic strains. The change of volume is then entirely elastic, with no plastic volumetric strain. The solid is given an initial velocity corresponding to a rotation around its center. The solid is in free flight afterwards. The total linear and angular momenta are then exactly conserved in this free motion, with the energy being dissipated (reduced) if plastic flow occurs while being fully conserved during purely elastic evolution steps. Figure 2.1 shows the deformed configuration of the solid at different times computed with the new volume-preserving EDMC scheme, depicting also the distribution of the equivalent plastic strain (thus showing the extent of the plastic flow in the material). The large finite deformations are apparent. Figure 2.2 shows the evolution in time of the three components of the linear momentum (left) and angular momentum (right) of the solid, confirming their exact conservation. Figure 2.3 shows the evolution of the total energy of the solution computed with the EDMC scheme and the classical trapezoidal rule (a member of the classical family of Newmark schemes) in combination with an exponential approximation of the plastic evolution equations, all for different time steps. A non-increasing energy evolution should be obtained after the initial stages when the load is applied. We can observe that, despite the dissipative character of the underlying physical system, the trapezoidal rule shows an uncontrolled growth of energy (blow-up) forcing to stop the computation. This numerical instability is observed for different time step sizes. This situation is to be contrasted with the energy evolution for the solution obtained by the new EDMC scheme. The energy dissipation is always strictly non-negative (by design) and, in fact, exact. In particular, full energy conservation is obtained during the elastic steps (again, by design). The significantly improved numerical stability properties of the new scheme are apparent. Furthermore, plots (not shown) confirm the lack of any plastic change of volume in the deformation of the solid, thus exactly reproducing the response of the solid.

We presented the development of the volume-preserving energy-dissipative momentum-conserving algorithms for isochoric models of finite strain plasticity in the papers [3,5]. A summary of these results, with additional details of the ones discussed above, can be found in Appendix I of this final report.

3. *Conserving assumed strain finite elements for continuum problems.* The quasi-incompressible character of the plastic response of metals requires the consideration of locking-free finite elements for their spatial discretization. Assumed strain methods treating the volumetric strain in a separate manner have been proven to be a reliable option in these situations. However, the direct use of existing techniques destroys the conservation/dissipation

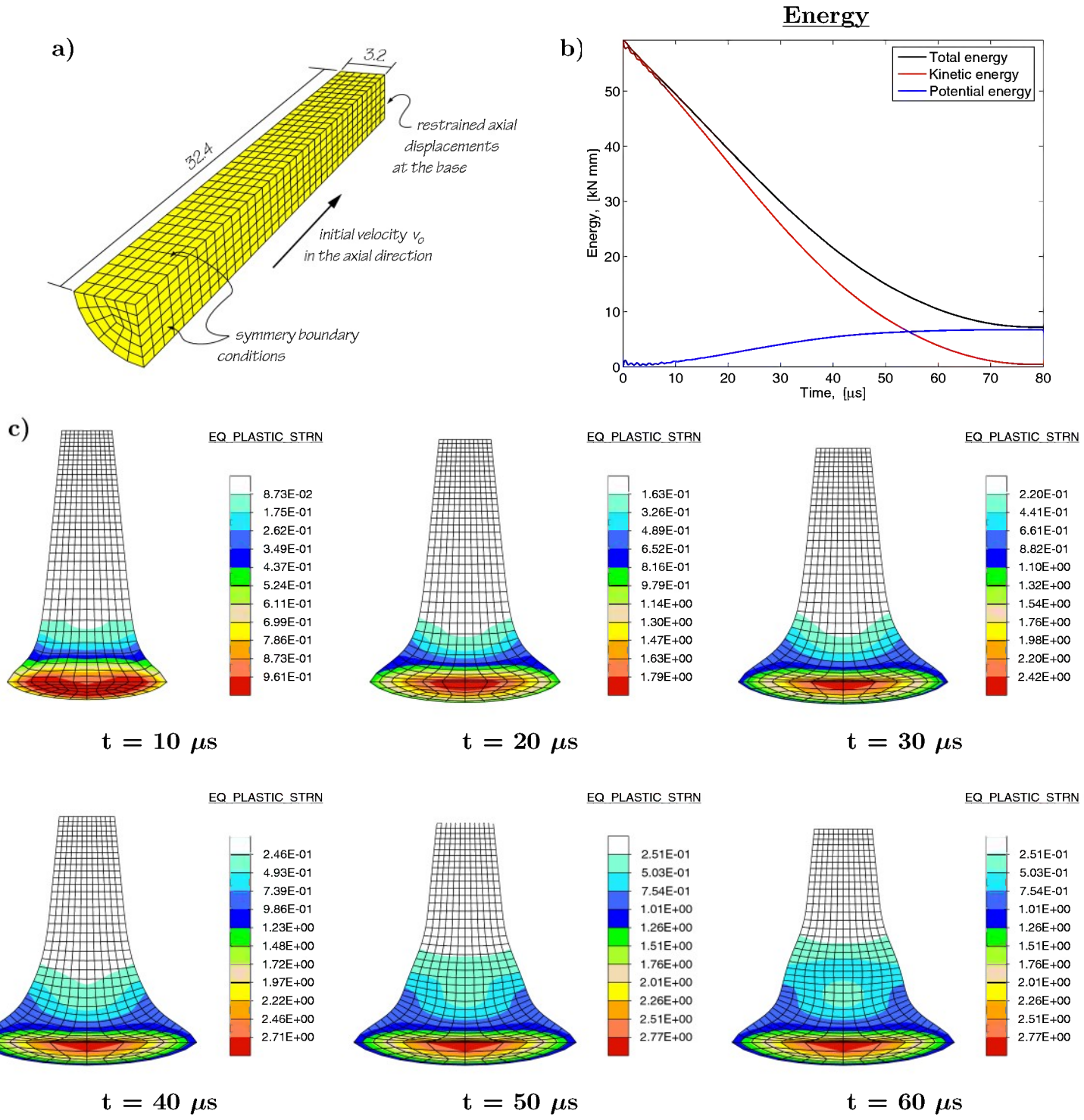

FIGURE 2.4 Impact of a cylindrical copper rod on a rigid wall. **a)** Problem definition (distances in mm), showing a quarter of the specimen discretized with 976 brick elements. The rod is given the initial axial velocity of $v_o = 0.227\ mm/\mu s$, modeling the impact on the rigid wall by imposed axial displacements at its base. **b)** Evolution of the energy (total with potential and kinetic) showing the monotonic decrease of the total energy consequence of the exactly captured plastic dissipation by the new EDMC time-stepping scheme in combination with the new assumed strain finite elements. Existing methods require a large amount of artificial numerical dissipation due to the appearance of highly oscillatory and unstable solutions. **c)** Deformed configurations in time showing the distribution of the equivalent plastic strain (half the specimen shown from below-front). The large strains are apparent (illustrating the lack of locking), and so is the bulging of the specimen as the specimen shortens, agreeing with experimental tests for the considered material of pure copper with large strain hardening.

properties of the temporal discretizations discussed above, thus requiring the development of new alternative techniques. We have developed new assumed strain finite elements based on the classical scaling of the volumetric part of the deformation gradient (i.e. its determinant or Jacobian) by a mixed Jacobian, but requiring an alternative definition of the associated linearized strain operator in the equations of motion. After identifying the conditions for the final scheme to be numerically consistent and to comply with the conservation laws of linear and angular momenta, the associated relative equilibria, and the evolution of the energy, a general strategy for the definition of this "conserving consistent linearization" has been identified. Based on this new approach, we have developed new quadrilateral and triangular elements for plane problems, and brick elements for three-dimensional applications. For example, a fully EDMC trilinear brick with constant volumetric strain (Q1/A0) and quadratic quad with linear volumetric strain (Q2/A1) are now available.

Figure 2.4 illustrates the performance of the newly developed conserving assumed strain finite elements in a typical application with large (isochoric) plastic strains. It shows the results obtained in the classical benchmark problem of the impact of a cylindrical rod on a rigid wall (Taylor's problem). The new EDMC time-stepping algorithms avoid any instabilities in time, in contrast with classical existing schemes that require an excessive amount of numerical dissipation to accomplish a meaningful solution (without spurious oscillations and instabilities). We note again that this is a direct consequence of the new schemes capturing exactly the physical dissipation occurring in the solid. The effectiveness of the new assumed strain finite elements in avoiding volumetric locking is confirmed by the large strains involved and their agreement with experimental observations (not shown). Basic displacement finite element methods would lock in this simulation due to the quasi-incompressible character of the deformation given the isochoric plastic response of the solid. The new elements are locking free while exactly exhibiting the energy dissipation and momentum conservation properties of the EDMC scheme used in the temporal discretization.

These results were presented in the papers [7,8,10]. Additional details can be found in Appendix II of this final report.

4. *Energy-dissipative momentum-conserving algorithms for finite strain thermo-elasticity.* We have developed new time-stepping algorithms for coupled thermo-elasticity that inherit by design the a-priori stability estimates of this physical system and its momenta conservation laws. The stress formula developed previously for uncoupled cases has been extended to account for the temperature coupling, defining in the process the proper temporal approximation of the conjugate entropy field. The proper treatment of the energy evolution equation, including heat conduction, has allowed to arrive to a new numerical scheme that exhibits rigorously the dissipative character of the so-called canonical free energy characteristic of these systems. Complete mathematical analyses are available. These

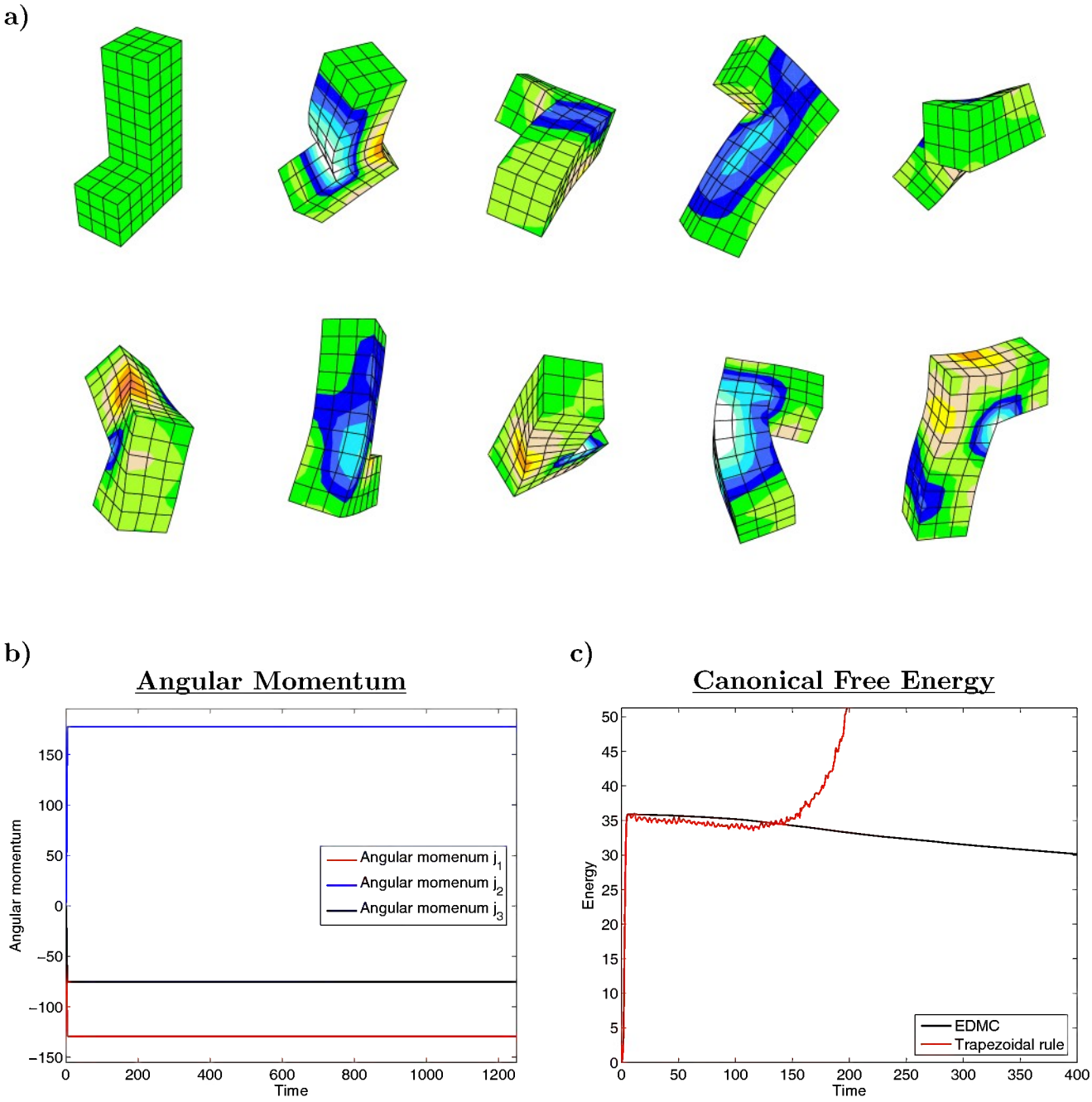

FIGURE 2.5 Tumbling of a L-shaped thermo-elastic block: solution obtained with the new EDMC schemes for thermo-elasticity. **a)** Motion depicted by the configuration of the solid at different times (left to right and down) with the distribution of the temperature. The undeformed solid (first top left frame) is given an initial loading on the top and bottom faces, being in free flight after this initial phase. The series of deformations illustrate the large displacements and strains that the solid is subjected to, with the temperature variation occurring from the associated thermo-elastic coupling. **b)** Evolution of the three components of the angular momentum. After the initial loading phase, the three components are exactly conserved, as they must physically, showing the momentum conserving properties of the new scheme. **c)** Evolution of the canonical free energy with time. The new EDMC scheme conforms with the a-priori stability estimate defined by the monotonic decrease of the canonical free energy, in contrast to the solution obtained by a classical scheme like trapezoidal rule exhibiting a nonlinear numerical instabilities in the form of an unbounded growth of the energy.

schemes can also be incorporated in a staggered (partitioned) solution of the problem. These results have been compiled in [12], with the plans of additional publications. In particular, the extension to coupled thermo-plasticity is also under consideration.

Figure 2.5 illustrates the performance of the new EDMC scheme developed in this part of the project. It includes the deformation and temperature distribution of a L-shaped thermo-elastic block tumbling in space. The conservation of the angular momentum and the monotonic decrease of the canonical free energy due to heat conduction after the initial loading conforms with the same properties of the continuum system. Thermal heat conduction introduces dissipation in the physical system, non-negative from the fundamental second law of thermodynamics, and leading to the monotonic decrease of the so-called canonical free energy. This defines an a-priori stability estimate that the numerical simulation must conform to for numerical stability (in the linear case, the canonical free energy strictly defines a norm of the solution in the displacement, velocity and temperature). The plot shows that the new EDMC does conform with this fundamental energy principle, thus leading to stable simulations of the motions of interest. This property is supported by rigorous mathematical analyses rigorously showing its satisfaction. This situation is to be contrasted with the performance of standard numerical schemes like the classical trapezoidal rule, also shown in the figure. The energy evolution is not monotonic in this case and, in fact, it leads to an unbounded growth, thus showing the instability of these classical schemes in the considered nonlinear range. The simulation blows up in this case, a performance that needs to be contrasted again with the new EDMC scheme. These instabilities are completely and rigorously avoided in the new schemes developed in this project.

5. *Extension to shell models.* We have also considered the application of the newly developed time-stepping algorithms to problems involving shells, as this is one of the main configurations in Air Force applications. In this way, we have developed the implementation of these new methods in reduced-solid shell elements, incorporating also the new assumed strain treatment developed for continuum problems discussed above (Item 3). Enhanced strain treatments for the through-the-thickness shell response as well as the incorporation of common assumed strain treatments of the bending/shear response have been considered. We have considered both plastic and thermoelastic shells. In both cases, the implementation follows the ideas presented in [8] for the construction of assumed strain finite element methods.

Figure 2.6 illustrate these results, currently under further development. It shows the solution obtained in the modeling of the motion of a L-shaped elastoplastic shell. The shell is loaded by transversal tractions along its extreme edges and at the central corner for a period of time, being in free-flight after this initial loading phase. The resulting motion is shown in that figure depicting the deformed configuration of the shell at different times. The large displacement, rotations and strains are apparent. The distribution of

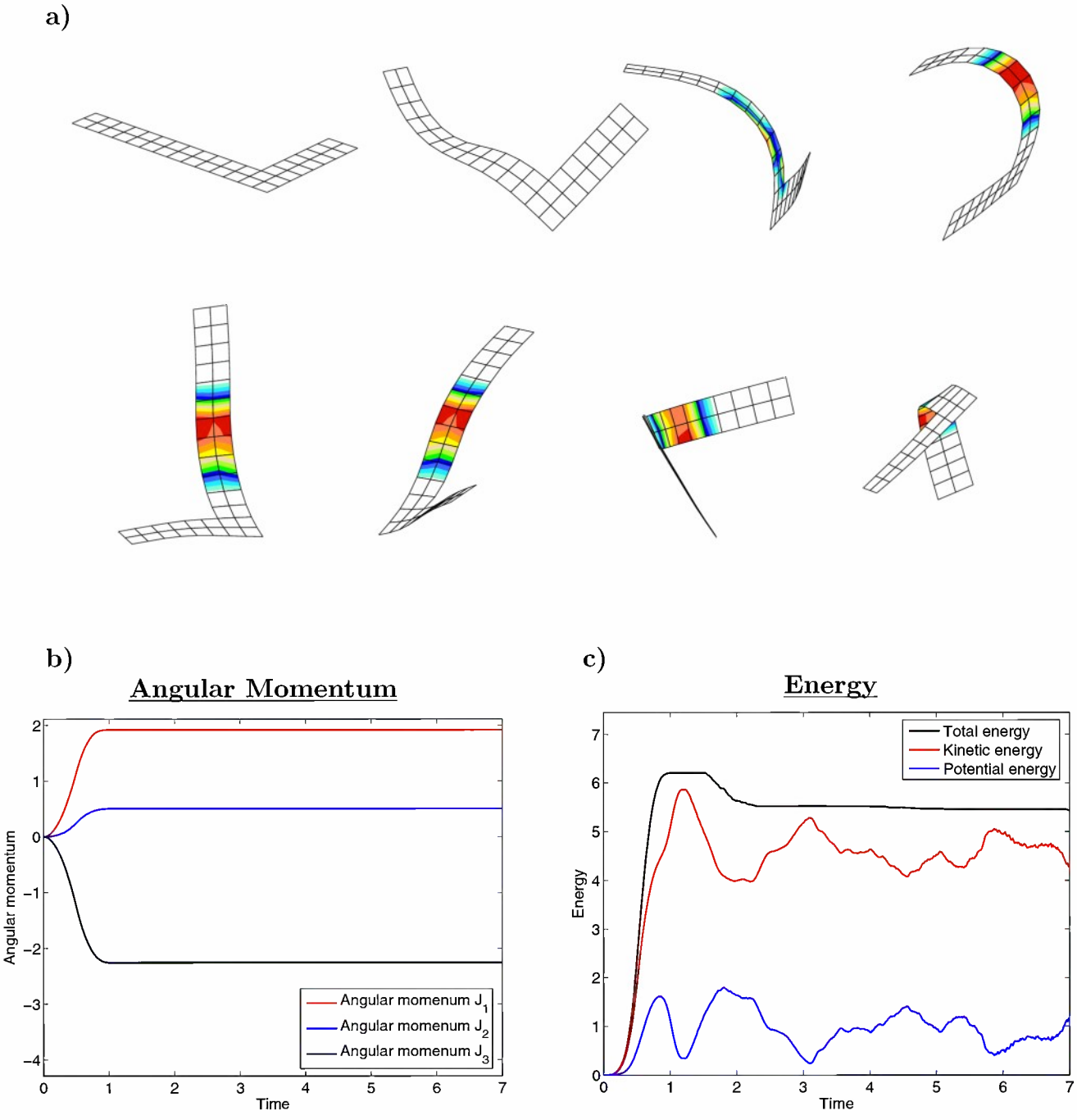

FIGURE 2.6 Tumbling of a L-shaped elastoplastic shell: solution obtained with the new EDMC schemes for finite strain plasticity of nonlinear shells. **a)** Motion depicted by the configuration of the solid at different times (left to right and down) with the distribution of the equivalent plastic strain. The undeformed solid (first top left frame) is loaded with distributed forces at both extreme edges and central corner, being in free-flight after the initial loading phase. The series of deformations illustrate the large displacements and strains that the solid is subjected to, including large plastic strains. **b)** Evolution of the three components of the angular momentum. After the initial loading phase, the three components are exactly conserved as it must happen from physical considerations, hence showing the momentum conserving properties of the new scheme. **c)** Evolution of the total energy and its kinetic and potential (strain plus hardening) energies. The monotonic evolution of the total energy is to be noted, with the energy decrease corresponding to the plastic dissipation captured exactly by the new EDMC scheme.

the equivalent plastic strain is also included, showing the extent of the plasticity. The important aspect is that the new EDMC scheme is able to capture exactly the energy dissipation of this plastic response. The evolution of the energy included in Figure 2.6 confirms this property.

6. *Other results: numerical modeling of fracture and failure through the strong discontinuity approach.* The previous accomplishments defined the main focus of this research project as outlined in the original grant proposal. In addition, we have started exploring the use of finite elements with embedded strong discontinuities for the analysis of dynamic failure of materials. The approach enhances the interpolations of traditional finite elements with the discontinuous solutions characteristic of the ultimate stages of the deformation of solids (e.g. cracks or shear bands). A multiscale approach allows to introduce these solutions (also known as strong discontinuities) into the finite elements at the local level, with enhanced parameters eliminated locally through their static condensation hence resulting in a very efficient solution of the global mechanical problem. A main advantage is that no remeshing is needed for the resolution of the discontinuity.

We have presented in [4,6] a new strategy for the development of these enhancements in the infinitesimal range of small strains. The approach is based on the direct introduction in the discrete strain field of the finite elements of the strain modes necessary for the accurate resolution of the kinematics associated with a discontinuous displacement field. Piece-wise linear interpolations of the discontinuity jumps are considered along the discontinuity, in contrast with the piece-wise constant interpolations existing to date. The new numerical approach leads, in particular, to quadrilateral finite elements able to represent the separation of the discontinuities without a spurious transfer of stresses (or stress locking).

The extension of these considerations to the finite deformation has been presented in [9]. In this case, the key aspect has been the development of a new enhancement of the deformation gradient, that conforms with the geometric structure of the problem, leading in particular to frame indifferent formulations. Furthermore, the new strategy has shown to be particularly appropriate for the analysis of failure and fracture of solids in the dynamic range. Preliminary results can be found in the technical report [11] for the infinitesimal case. These results have motivated and defined the research lines to follow in this effort as describe in the following section.

3. Current and Future Work

The results obtained in this project have allowed to identify a number of extensions and new lines of research for the near future. As indicated at the end of the last section, the numerical analysis of the failure and fracture of solids defines an important problem to be addressed, given the many applications of interest to the Air Force. In particular, the

numerical resolution of the highly non-smooth solutions observed in the ultimate stages of the deformation of solids sets out a very challenging problem. These solutions involve strong discontinuities whose modeling in a numerically discrete context require the design of special numerical methods for their resolution. Typical examples of these considerations are cracks in brittle or quasi-brittle materials, or shear bands (and similar localization bands) in ductile failures.

As noted above, we are already involved in the development of new finite elements to capture these discontinuities at the element interiors. This is accomplished through a multi-scale treatment of the mechanical problem at hand, with the consideration of the discontinuities at the local (element) level, thus leading to very efficient numerical techniques, easily accommodating existing numerical methods for the large scale.

The dynamic range defines a particularly difficult setting for the different additional effects to be resolved accurately and in a stable manner. For example, crack branching defines a difficult problem to be captured numerically, because of both the spatial discretization and the time-stepping scheme. In the former, and in the context of the considered finite elements with embedded strong discontinuities, the design of new element enhancements that can accommodate a bifurcating discontinuity defines a clear objective for the continuing effort. Similarly, the development of stable temporal discretizations (extending the energy-dissipative momentum-conserving schemes developed in this project to cases involving an inelastic cohesive law along discontinuity surface) is another clear objective for future work. In addition, the need to consider additional physical effects (like coupled thermoplastic responses at high strain rates) motivates also the consideration of the extension of the work develop here to those cases (e.g. EDMC time-stepping algorithms for nonlinear coupled thermoplasticity).

This continuing effort will widen the range of application to the methods that we have developed in the current research project. The overall approach followed in it (that is, the mathematical analysis of the discrete equations drives the design of new numerical schemes) will be crucial in all of our future developments in this area.

4. Personnel

The P.I., Francisco Armero, was partially supported during the summer months of the project. Two graduate students have been funded under this grant: Christian Linder and Christian Zambrana-Rojas. Christian Linder continued as a Postdoc for three months after completion of his PhD Dissertation.

5. Publications under AFOSR Support

The following papers have appeared and/or have been prepared during the performance of this grant acknowledging AFOSR support (2005/2008):

1. Armero, F. [2005] "Energy-Dissipative Momentum-Conserving Time-Stepping Algorithms for Dynamic Plastic Finite Strain Plasticity," Proceedings of the VIII International Conference on Computational Plasticity (COMPLAS 8), Barcelona, Spain.

2. Armero, F. [2006] "Energy-Dissipative Momentum-Conserving Time-Stepping Algorithms for Finite Strain Multiplicative Plasticity," *Computer Methods in Applied Mechanics and Engineering,* 195, 4862-4889.

3. Armero, F. & Zambrana, C. [2006] "Numerical Integration of the Nonlinear Dynamics of Elastoplastic Solids," Proceedings of the III European Conference on Computational Mechanics (ECCM-06), Lisbon, Portugal.

4. Armero, F. & Linder, C. [2006] "Recent Developments in the Formulation of Finite Elements with Embedded Strong Discontinuities," IUTAM Symp. on Discretization Methods for Evolving Discontinuities, IUTAM Book series, Springer, contributed refereed article.

5. Armero, F. & Zambrana, C. [2007] "Volume-Preserving Energy-Momentum Schemes for Isochoric Multiplicative Plasticity," *Computer Methods in Applied Mechanics and Engineering,* 196, 4130-4159.

6. Linder, C. & Armero, F. [2007] "Finite Elements with Embedded Strong-Discontinuities for the Modeling of Failure of Solids," *International Journal for Numerical Methods Engineering,* 72, 1391-1433.

7. Armero, F. [2007] "Energy-Momentum Algorithms for Nonlinear Solid Dynamics and their Assumed Strain Finite Element Formulation," Proceedings of COMPDYN07, Rethymno, Greece (to appear in the book *Progress in Computational Dynamics and Earthquake Engineering,* ed. by M. Papadrakakis et al, Taylor & Francis).

8. Armero, F. [2008] "Assumed Strain Finite Element Methods for Conserving Temporal Integrations in Nonlinear Solid Dynamics," *International Journal for Numerical Methods in Engineering,* 74, 1795-1847.

9. Armero, F. & Linder, C. [2008] "New Finite Element Methods with Embedded Strong Discontinuities in the Finite Deformation Range," *Computer Methods in Applied Mechanics and Engineering,* 197, 3138-3170.

10. Armero, F. [2008] "Energy-Momentum Algorithms for the Nonlinear Dynamics of Elastoplastic Solids," IUTAM Symp. Theoretical, Modeling and Computational Aspects of Inelastic Media, IUTAM Book series, Springer, contributed refereed article.

11. Armero, F. & Linder C. [2008] "Numerical Simulation of Dynamic Fracture with Finite Elements with Embedded Strong Discontinuities," report no. UCB/SEMM-2008/01, UC Berkeley (to be submitted).

12. Armero, F. [2008] "Energy-Momentum Algorithms for Nonlinear Coupled Thermoelasticity," report no. UCB/SEMM-2008/03, UC Berkeley (to be submitted).

6. Interactions, Conference Contributions

The results obtained in this research project have been presented in the following conferences/seminars during the performance of this grant (2005/2008):

1. "Numerical Integration of the Nonlinear Dynamics of Solids and Structures," invited seminar, Department of Aerospace and Mechanical Engineering, University of Southern California, January 20, 2005.

2. "Energy-Dissipative Momentum-Conserving Time-Stepping Algorithms for Dynamic Plastic Finite Strain Plasticity," invited contribution, VIII International Conference on Computational Plasticity (COMPLAS 8), Barcelona, Spain, September 4-6 2005.

3. "Finite Element Locking and the Enhanced Strain Formulation," CISM course on Mixed Finite Element Technologies, CISM Udine, Italy, September 26-30, 2005.

4. "Numerical Integration of the Nonlinear Dynamics of Inelastic Solids and Structures," Department of Civil and Environmental Engineering, University of California at Los Angeles (UCLA), February 14 2006.

5. "Numerical Integration of the Nonlinear Dynamics of Elastoplastic Solids," keynote lecture, 3^{rd} European Conference on Computational Mechanics (ECCM 3), Lisbon, Portugal, June 5-9 2006.

6. "Energy-Momentum Schemes for Finite Strain Plasticity," keynote lecture, 7^{th} World Congress on Computational Mechanics (WCCM 7), Los Angeles CA, July 17-21 2006.

7. "Finite Elements with Embedded Strong Discontinuities of Higher Order Kinematics," invited contribution, 7^{th} World Congress on Computational Mechanics (WCCM 7), Los Angeles CA, July 17-21 2006.

8. "Recent Developments in the Formulation of Finite Elements with Embedded Strong Discontinuities," invited contribution, IUTAM Symposium on Discretization Methods for Evolving Discontinuities, Lyon, France, September 4-7 2006.

9. "Energy-Momentum Algorithms for Nonlinear Solid Dynamics and their Assumed Strain Finite Element Formulation," invited semi-plenary lecture, Computational Meth-

ods in Structural Dynamics and Earthquake Engineering (COMPDYN07), Rethymno, Greece, June 13-16 2007.

10. "New Finite Elements with Embedded Strong Discontinuities," invited contribution, 9^{th} US National Congress on Computational Mechanics (USNCCM 9), San Francisco, CA, July 23-26, 2007.

11. "Dynamic Fracture Using Finite Elements Enhanced with Cohesive Discontinuities," 9^{th} US National Congress on Computational Mechanics (USNCCM 9), San Francisco, CA, July 23-26, 2007.

12. "Finite Elements with Embedded Discontinuities and Dynamic Fracture," invited contribution, IX International Conference on Computational Plasticity (COMPLAS 9), Barcelona, Spain, September 5-7 2007.

13. "Numerical Integration in Nonlinear Solid and Structural Dynamics," Department of Civil and Environmental Engineering, Johns Hopkins University, December 17 2007.

14. "Energy-Momentum Algorithms for Nonlinear Dynamics of Elastoplastic Solids," invited contribution, IUTAM Symposium on Theoretical, Modeling and Computational Aspects of Inelastic Media, Cape Town, South Africa, January 14-18 2008.

15. "Finite Element Modeling of Kirchhoff Rods," invited contribution, 6^{th} International Conference on Computation of Shell and Spatial Structures (IASS-IACM 2008), Cornell University, Ithaca, NY, May 28-31 2008.

16. "Energy-Momentum Algorithms for Nonlinear Coupled Thermo-Elastodynamics," invited keynote lecture, 8^{th} World Congress on Computational Mechanics (WCCM 8), Venice, Italy, June 30-July 4 2008.

17. "Modeling of Dynamic Fracture using Finite Elements with Embedded Strong Discontinuities," invited contribution, 8^{th} World Congress on Computational Mechanics (WCCM 8), Venice, Italy, June 30-July 4 2008.

7. Honors and Awards

The PI, Francisco Armero was elected Fellow of the International Association of Computational Mechanics (IACM) in 2004. The Fellows Award was given to him during the 6^{th} World Congress on Computational Mechanics that took place in Beijing, China, September 5-11, 2004. Additionally, Francisco Armero was awarded in the past the Young Investigator Award by the International Association for Computational Mechanics (IACM) in July 2002, the Juan C. Simó award and medal by SEMNI (Spanish Society for Numerical Methods in Engineering) in June 1999, the NSF CAREER award (National Science

Foundation) in June 1997, and the ONR Young Investigator Award (Office of the Naval Research) in June 1996. He also received the best paper award for "the most outstanding paper published in *Engineering Computations* in the year 1997".

Additional honors to the PI, Francisco Armero, related to this research project during the performance of the grant include service as:

1. Member of the editorial/advisory board of:
   - Communications in Numerical Methods in Engineering, April 2005-present.
   - ASCE Journal of Engineering Mechanics, Associate Editor, Sept. 2003-Oct. 2005.
   - Informes de la Construcción, December 2006-present.
   - Computers & Concrete, April 2003-present.
   - Finite Elements in Analysis and Design, February 2002-present.
   - Computer Methods in Applied Mechanics and Engineering, June 2001-present.
   - International Journal for Numerical Methods in Engineering, January 2001-present.
   - Computers & Structures, November 1998-present.
   - International Journal of Numerical Methods in Fluids, November 1997-January 2008.

2. Committee service:
   - Committee on Computational Mechanics, ASCE Engineering Mechanics Division (August 1999-present), vice-chair (2003-2004, 2006-present), chair (August 2004-2006).
   - Technical Advisory Committee, 10^{th} International Conference on Computational Plasticity (COMPLAS X), Barcelona, Spain, September 2-4, 2009.
   - International Advisory Board, Computational Methods in Structural Dynamics and Earthquake Engineering (COMPDYN09), Island of Rhodes, Greece, June 22-24, 2009.
   - International Advisory Board, 1^{st} International Conference on Computational Technologies in Concrete Structures (CTCS09), Seoul, Korea, May 2009.
   - Scientific Advisory Committee, 9^{th} International Conference on Computational Structures Technology, Athens, Greece, September 2-5, 2008.
   - Local Organizing Committee, 9 US National Congress on Computational Mechanics (USNCCM 9), San Francisco CA, July 17-19, 2007.
   - International Advisory Board, Computational Methods in Structural Dynamics and Earthquake Engineering (COMPDYN07), Rethymnon, Crete, Greece, June 13-15, 2007.
   - Technical Advisory Committee, International Conference on Coupled Problems, Ibiza, Spain, May 21-23, 2007.

- Technical Advisory Committee, 9^{th} International Conference on Computational Plasticity (COMPLAS IX), Barcelona, Spain, September 5-7, 2007.
- Scientific Programme Committee, 7^{th} World Congress on Computational Mechanics (WCCM7), Los Angeles CA, U.S.A., July 16-22, 2006.
- Scientific Committee, III European Conference on Computational Mechanics, Lisbon, Portugal, June 5-9, 2006.
- Scientific Advisory Committee, 8^{th} International Conference on Computational Structures Technology, Las Palmas de Gran Canaria, Spain, September 12-15, 2006.
- Scientific Committee, 5^{th} International Conference on Computation of Shells and Spatial Structures (IASS-IACM 2005), Salzburg, Austria, June 1-4, 2005.
- Technical Advisory Committee, International Conference on Coupled Problems, Santorini Island, Greece, May 25-28, 2005.
- Technical Advisory Committee, 8^{th} International Conference on Computational Plasticity (COMPLAS VIII), Barcelona, Spain, September 5-8, 2005.
- Scientific Advisory Committee, 7^{th} International Conference on Computational Structures Technology, Lisbon, Portugal, September 7-9, 2004.

3. Organizer of symposia:
   - "Numerical Techniques for the Modeling of Material Failure," 7 sessions, 38 contributions, 8^{th} World Congress on Computational Mechanics (VIII WCCM), Venice, Italy, June 30-July 4, 2008.
   - "Numerical Techniques for the Modeling of Material Failure in Solids: Symposium in Honor of Professor Kaspar Willam on the Occasion of his 65^{th} birthday," 7 sessions, 32 contributions, 9^{th} US National Congress on Computational Mechanics (IX USNCCM), San Francisco CA, July 23-26 2007.
   - "Modeling and Numerical Simulation of of Failure in Inelastic Shells and Spatial Structures," 5^{th} International Conference on Computation of Shell and Spatial Structures (IASS-IACM 2005), Salzburg, Austria, June 1-4 2005.

8. Outline of the Rest the Report

We have added two appendices to this report to illustrate in more detail some of the technical results obtained in this project. Appendix I describes the formulation of energy-dissipative momentum-conserving schemes for finite strain plasticity that also conserve the plastic volumetric response of the underlying model (Item 2 in Section 2). Appendix II describes the development of the new assumed strain finite element methods for the conserving time-stepping algorithms (Item 3 in Section 2). A more detailed description follows.

8.1. Appendix I: Volume-Preserving Energy-Dissipative Momentum-Conserving Time-Stepping Algorithms for Isochoric Plastic Models of Multiplicative Plasticity

This appendix presents a new energy-dissipative momentum-conserving algorithm for multiplicative finite strain plasticity ($\boldsymbol{F} = \boldsymbol{F}^e\boldsymbol{F}^p$) that also preserves exactly the plastic volume for isochoric plastic models. The new algorithm exhibits exactly the conservation laws of linear and angular momentum of the underlying physical problem as well as its energy evolution. A strictly positive energy dissipation, in fact the exact energy dissipation, is obtained by design during plastic steps while enforcing the plastic consistency (i.e. the yield condition) on the final stress appearing in the equations of motion. Exact energy conservation is attained, in particular, during elastic steps. The aforementioned preservation of the plastic volume is obtained by a new treatment of the geometric structure behind the considered multiplicative models of finite strain plasticity. Namely, we present a new approximation of the reference and elastic metrics whose contractions with the incremental total and elastic strains lead exactly to the increment of the total and elastic natural volumetric strains, respectively. The elastic metric is defined in the intermediate configuration, defined itself by the proper discrete approximation in time of the plastic deformation gradient $\boldsymbol{F}^p$. The new algorithm extends to the plastic range existing energy-momentum conserving schemes for nonlinear elastic problems, but incorporating a new modified elastic stress formula consistent with this new geometric setting. The inherited conservation laws of momenta and, especially, the non-negative character of the energy dissipation leads to an improved performance over existing, more classical schemes showing numerical instabilities in the considered highly nonlinear geometric setting of large deformations and strains. Several numerical simulations are presented illustrating these properties.

8.2. Appendix II: Assumed Strain Finite Element Methods for Conserving Time-Stepping Algorithms

This appendix presents a new assumed strain finite element formulation (or B-bar method) for the locking-free simulation of nearly incompressible elastic and inelastic solids in the finite deformation dynamic range that also preserves the conservation/dissipation properties of the so-called energy-dissipative momentum-conserving (EDMC) time-stepping algorithms. The general setting of finite strain plasticity is considered, including hyperelastic models as a particular case. The main motivation of this work is to avoid the nonlinear numerical instabilities observed in classical numerical schemes with unbounded growth of the energy (even in the plastic case) by introducing the exact dissipation/conservation of the energy in the discrete system by design. The incorporation of the conservation laws of linear and angular momenta, and the preservation of the associated relative equilibria, is also obtained. The paper identifies the conditions that the linearized strain operator (or, simply, the B-bar operator as it is usually known) has to satisfy for the preserva-

tion of these properties in time. These conditions require the definition of the assumed strain operator, originally developed by with spatial considerations only, accounting for the temporal discretization in the definition of the associated strain variations. As a result, we arrive to a fully discrete system in space and time that shows exactly all these conservation/dissipation laws of the underlying physical system, including the exact plastic dissipation of the energy, with exact energy conservation for elastic steps. Numerical simulations are presented to illustrate the performance of the new formulation.

APPENDIX I

Volume-Preserving Energy-Dissipative Momentum-Conserving Time-Stepping Algorithms for Isochoric Plastic Models of Multiplicative Plasticity

Based on the papers:

Armero, F. & Zambrana, C. [2007] "Volume-Preserving Energy-Momentum Schemes for Isochoric Multiplicative Plasticity," *Computer Methods in Applied Mechanics and Engineering,* 196, 4130-4159.

Armero, F. & Zambrana, C. [2006] "Numerical Integration of the Nonlinear Dynamics of Elastoplastic Solids," Proceedings of the III European Conference on Computational Mechanics (ECCM-06), Lisbon, Portugal.

I.1. Introduction

Classical time-stepping algorithms for the numerical integration of problems in solid and structural dynamics, like the Newmark scheme NEWMARK [1959] and its variations (see HUGHES [1987] for a complete account), have been shown to exhibit serious limitations when applied to geometrically nonlinear problems despite their good performance in the linear setting. These limitations include not only the lack of preserving important conservation laws of the motion, like the conservation law of angular momentum, but also to numerical instabilities in the form of an unbounded growth of energy. These instabilities limit severely the time step size that can be used in the simulations, even in algorithms that have been proven to be unconditionally stable in the linear range. This situation has motivated the development of the so-called energy-momentum schemes, where the conservation laws of momenta and energy are embedded in the algorithm by design; see CRISFIELD & SHI [1994],GONZÁLEZ [2000],SIMO & TARNOW [1992], among others, and ARMERO & ROMERO [2001a],ARMERO & ROMERO [2001b]],KUHL & CRISFIELD [1997],KUHL & RAMM [1996] for extensions exhibiting a controllable numerical dissipation in the high-frequency to handle the high numerical stiffness of the systems of interest. We note in this respect that classical high-frequency dissipative schemes, like the HHT (see HUGHES [1987]), loose also their unconditional stability in the nonlinear range ARMERO & ROMERO [2001a].

These numerical instabilities have also been observed in the elastoplastic range at finite strains, thus motivating the extensions of the above energy-momentum schemes for elastic systems to this inelastic setting, as considered in MENG& LAURSEN [2002],NOELS ET AL [2004]. A major challenge in these problems is the proper integration of the plastic evolution equations for the plastic internal variables giving also the stresses or, in other words, the proper return mapping algorithm. In this context, the work presented in MENG& LAURSEN [2002] considers standard existing return mapping algorithms with an additional projection step on the stress, along the lines presented in GONZÁLEZ [2000] for elastic problems, to recover the proper energy dissipation in the plastic range. This step, however, disturbs the satisfaction of the initially enforced plastic consistency condition for the final resulting stress. The algorithms presented in NOELS ET AL [2004] considered hypoelastic based models, thus being able to impose only the conservation/dissipation in very specific particular cases.

We have recently presented in ARMERO [2006],ARMERO [2005] an alternative strategy leading to new energy-dissipative momentum-conserving time-stepping algorithm for multiplicative plasticity ($\boldsymbol{F} = \boldsymbol{F}^e\boldsymbol{F}^p$) that exhibits the exact energy dissipation of the underlying physical system, while enforcing exactly the consistency condition on the final stresses. The development of the new algorithm follows the same arguments leading to these conservation/dissipation properties for the continuum problem, identifying in the process the proper discrete approximation of the plastic strain rate that preserves the dissipative character of the (discrete) plastic flow. The final scheme is implemented following the classical

structure of return mapping algorithms consisting of an elastic trial state followed a plastic corrector imposing the yield condition on the stresses (or its viscoplastic regularization). However, in contrast with existing exponential return mapping algorithms, originally proposed in ETEROVICH & BATHE [1990],CUITINHO & ORTIZ [1992],SIMO [1992],WEBER & ANAND [1990] (see complete details in the monograph SIMO [1998]), the new scheme involves an algebraic approximation of the flow rule in the updated plastic deformation gradient $\boldsymbol{F}^p_{n+1}$, not enforcing automatically the isochoric character of the plastic flow in isochoric plastic models like the models of J_2-flow theory for metals.

It is precisely the goal of this contribution to develop alternative algorithms that also exhibit this volume-preserving property. As shown in the developments below, the crucial observation in the accomplishment of this goal is the proper approximation of the geometric structure behind the considered multiplicative models of finite strain plasticity. In this way, the new algorithm considers explicitly the approximation of the metrics in the reference and intermediate configurations that define the change of volumetric strains, total and elastic respectively, in these models. The actual definition of the intermediate configuration in the discrete setting of a time step requires special considerations for the proper approximation of this geometric structure. Altogether, we develop in this work a new volume-preserving energy-dissipative momentum-conserving scheme that exactly preserves the isochoric character of the plastic flow in the aforementioned models of metal plasticity while still preserving exactly the conservation laws of linear and angular momenta, and also recovering the exact energy dissipation of the physical system. This means, in particular, that exact energy conservation is obtained for elastic steps, extending to the elastoplastic case existing energy-momentum schemes with the aforementioned improved stability properties.

An outline of the rest of the paper is as follows. Section I.2 presents a summary of the governing equations of finite strain multiplicative plasticity in the dynamic range with an outline of the arguments leading to the conservation/dissipation properties of interest here, including the geometric structure behind these equations. Following the approach advocated here, it is the analog of these very same arguments that leads to the formulation of the new volume-preserving energy-dissipative momentum-conserving scheme, as developed in Section I.3. Section I.4 present representative numerical simulations illustrating the performance of the new algorithm in comparison with existing schemes. Finally, Section I.5 includes some final remarks.

I.2. Problem Definition

We summarize in this section the problem of interest in this work. In this way, Section I.2.1 describes the governing equations, including the equations of motion and the relations defining the multiplicative models of finite strain plasticity. Important in our developments is to fully characterize the dissipative character of the final equations, as

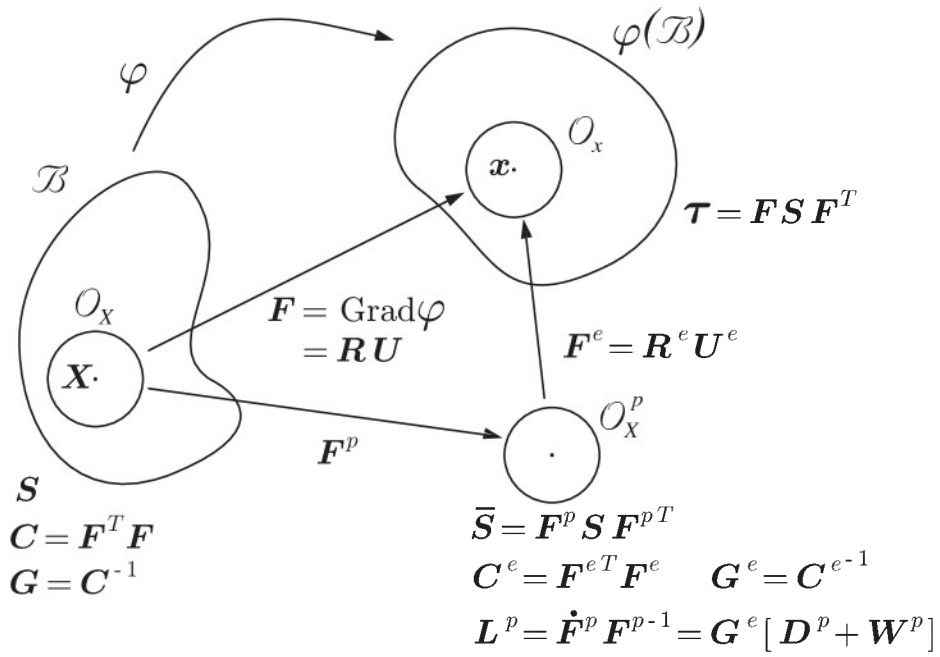

FIGURE I.2.1 Finite strain multiplicative plasticity. Problem definition

done in that section, and the geometric setting defining the volumetric strain changes in their elastic and plastic parts. This is discussed in Section I.2.2. We refer to SIMO [1998] for complete details on the results summarized here.

I.2.1. The governing equations and energy dissipation in multiplicative plasticity

We are interested in the motion $\boldsymbol{\varphi} : \mathcal{B} \times [0,T] \to \mathbb{R}^3$ of a solid represented by $\mathcal{B} \subset \mathbb{R}^3$ in the time interval T, determined by the weak equation

$$\int_{\mathcal{B}} \rho_o \ddot{\boldsymbol{\varphi}} \cdot \delta\boldsymbol{\varphi}\, dV + \int_{\mathcal{B}} \boldsymbol{S} : \left(\boldsymbol{F}^T \mathrm{GRAD}(\delta\boldsymbol{\varphi})\right)^s\, dV = G_{ext}(\boldsymbol{\varphi}, \delta\boldsymbol{\varphi})\ , \tag{I.2.1}$$

for all admissible variations $\delta\boldsymbol{\varphi}$, that is, $\delta\boldsymbol{\varphi} = 0$ on $\partial_\varphi\mathcal{B} \subset \partial\mathcal{B}$ (the part of the boundary where the deformation $\boldsymbol{\varphi}$ is imposed). Here we have considered the deformation gradient $\boldsymbol{F} = \mathrm{GRAD}(\boldsymbol{\varphi})$, the second Piola-Kirchhoff stress tensor $\boldsymbol{S} = \boldsymbol{S}^T$ (symmetric), the reference density ρ_o and the solid's acceleration $\ddot{\boldsymbol{\varphi}} = \partial^2\boldsymbol{\varphi}/\partial t^2$. The right-hand-side of (I.2.1) corresponds to the virtual work of the external loading denoted generically by G_{ext}.

We are interested in models of multiplicative plasticity defined by the elastoplastic decomposition

$$\boldsymbol{F} = \boldsymbol{F}^e\boldsymbol{F}^p\ , \tag{I.2.2}$$

defining locally the intermediate configuration $\mathcal{O}_X^p$ by the plastic deformation gradient $\boldsymbol{F}^p$; see Figure I.2.1. The elastic part of the deformation gradient $\boldsymbol{F}^e$ defines the stresses $\boldsymbol{S}$

through the hyperelastic relations

$$\boldsymbol{S} = \boldsymbol{F}^{p^{-1}}\bar{\boldsymbol{S}}\boldsymbol{F}^{p^{-T}} \quad \text{with} \quad \bar{\boldsymbol{S}} = 2\frac{\partial W^e}{\partial \boldsymbol{C}^e} \,, \tag{I.2.3}$$

in the intermediate configuration $\mathcal{O}_X^p$ for the elastic potential $W^e(\boldsymbol{C}^e)$ in terms of the elastic right Cauchy-Green tensor $\boldsymbol{C}^e = \boldsymbol{F}^{e^T}\boldsymbol{F}^e$ (by frame indifference). We note the relation

$$\dot{W}^e = \bar{\boldsymbol{S}} : \frac{1}{2}\dot{\boldsymbol{C}}^e \,, \tag{I.2.4}$$

giving the change of elastic strain energy.

Assuming for simplicity the case of no external loading (that is, $G_{ext} = 0$ and $\partial_\varphi \mathcal{B} = \emptyset$), the insertion of the velocity $\dot{\boldsymbol{\varphi}}$ (now an admissible variation) in the variation slot of (I.2.1) leads to the energy relation

$$\frac{d}{dt}\underbrace{\left[\int_{\mathcal{B}} \frac{1}{2}\rho_o \|\dot{\boldsymbol{\varphi}}\|^2 \, dV + W^e(\boldsymbol{C}^e) + \mathcal{H}(\alpha)\right]}_{\textit{total energy } H(t)} = -\underbrace{\int_{\mathcal{B}} \left[\bar{\boldsymbol{S}} : \boldsymbol{D}^p + q\ \dot{\alpha}\right] \, dV}_{\textit{plastic dissipation } \mathcal{D}} \,, \tag{I.2.5}$$

identifying the plastic strain rate

$$\boldsymbol{D}^p := \text{sym}\left[\boldsymbol{G}^{e^{-1}}\boldsymbol{L}^p\right] = \frac{1}{2}\left(\boldsymbol{F}^{p^{-T}}\dot{\boldsymbol{C}}\boldsymbol{F}^{p^{-1}} - \dot{\boldsymbol{C}}^e\right) \,, \tag{I.2.6}$$

for $\boldsymbol{L}^p = \dot{\boldsymbol{F}}^p\boldsymbol{F}^{p^{-1}}$ and $\boldsymbol{G}^e := \boldsymbol{C}^{e^{-1}}$. In (I.2.5) we have introduced the hardening potential $\mathcal{H}(\alpha)$ in terms of the strain-like internal variable α and its conjugate stress-like variable $q = -\partial\mathcal{H}/\partial\alpha$. We assume for simplicity the case of isotropic hardening in terms of the scalar equivalent plastic strain α.

The role of $\boldsymbol{G}^e$ in the definition of the plastic strain rate $\boldsymbol{D}^p$ in (I.2.6) is to be noted, defining the proper geometric setting in the intermediate configuration $\mathcal{O}_X^p$. Indeed, we can identify this (symmetric positive definite) tensor $\boldsymbol{G}^e = \boldsymbol{C}^{e^{-1}}$ as the metric in that configuration, allowing to define the "two-cova" tensor associated with $\boldsymbol{L}^p$ before taking its symmetric part. Similarly, we identify the metric $\boldsymbol{G} = \boldsymbol{C}^{-1}$ for $\boldsymbol{C} = \boldsymbol{F}^T\boldsymbol{F}$ in the reference configuration $\mathcal{O}_X$; see Figure I.2.1.

For the developments below, it is important to emphasize that the actual calculation of the energy evolution (I.2.5) identifies the plastic strain rate (I.2.6) as it appears in the plastic dissipation $\mathcal{D}$. It is precisely the physical requirement

$$\mathcal{D} \geq 0 \quad \text{(second law)} \tag{I.2.7}$$

that motivates the use of this plastic strain rate $\boldsymbol{D}^p$ in the formulation of plastic models. A general elastoplastic model can be written as

$$\boldsymbol{D}^p = \gamma\ \boldsymbol{N}_{\phi_{\bar{S}}}(\bar{\boldsymbol{S}}, q; \boldsymbol{G}^e) \,, \tag{I.2.8}$$

$$\boldsymbol{W}^p = \gamma\ \widehat{\boldsymbol{M}}_{W^p}(\bar{\boldsymbol{S}}, q; \boldsymbol{G}^e) \,, \tag{I.2.9}$$

$$\dot{\alpha} = \gamma\ n_{\phi_q}(\bar{\boldsymbol{S}}, q; \boldsymbol{G}^e) \,, \tag{I.2.10}$$

in the intermediate configuration $\mathcal{O}_X^p$. Here, we have introduced the plastic spin $\boldsymbol{W}^p$

$$\boldsymbol{W}^p := \text{skew}\left[\boldsymbol{G}^{e^{-1}}\boldsymbol{L}^p\right] , \tag{I.2.11}$$

in (I.2.9) so the whole plastic deformation gradient rate $\dot{\boldsymbol{F}}^p$ is determined by the plastic evolution equations (I.2.8)-(I.2.9). This requires nine components in three-dimensional problems, given by the six components of the (symmetric) plastic strain rate $\boldsymbol{D}^p$ and the three components associated to the skew plastic spin $\boldsymbol{W}^p$. Equation (I.2.8) corresponds to the flow rule whereas equation (I.2.10) defines the so-called hardening law.

The plastic multiplier γ in equations (I.2.8)-(I.2.9) is determined by the Kuhn-Tucker loading/unloading and consistency conditions

$$\phi(\bar{\boldsymbol{S}}, q; \boldsymbol{G}^e) \leq 0 , \quad \gamma \geq 0 , \quad \phi\gamma = 0 , \quad \dot{\phi}\gamma = 0 \tag{I.2.12}$$

for a general yield function $\phi(\bar{\boldsymbol{S}}, q; \boldsymbol{G}^e)$. Note the dependence on the metric $\boldsymbol{G}^e$ of the intermediate configuration $\mathcal{O}_X^p$ of both the yield function and the plastic flow vectors in (I.2.8)-(I.2.9), besides the stress variables $\bar{\boldsymbol{S}}$ and q. The Perzyna regularization of equations (I.2.12) defines the viscoplastic model

$$\gamma = \frac{g(\phi)}{\eta} , \quad \text{for} \quad g(\phi) = \begin{cases} 0 & \text{for } \phi \leq 0 , \\ \text{monotonically increasing} & \text{for } \phi > 0 , \end{cases} \tag{I.2.13}$$

and a viscous parameter $\eta > 0$, recovering the elastoplastic equations (I.2.12) in the limit $\eta \to 0$.

A typical choice for the flow vectors in (I.2.8)-(I.2.9) is given by the so-called associated relations

$$\boldsymbol{N}_{\phi_{\bar{S}}} = \frac{\partial \phi}{\partial \bar{S}} \qquad \text{and} \qquad n_{\phi_q} = \frac{\partial \phi}{\partial q} , \tag{I.2.14}$$

with a vanishing plastic spin $\widehat{\boldsymbol{M}}_{W^p} = 0$, especially for isotropic models. The flow vectors (I.2.14) result also from the classical principle of maximum plastic dissipation; see SIMO [1998].

Remark I.2.1 The physical condition (I.2.7) is easily satisfied by the associated plastic flow vectors (I.2.14) for yield functions of the form

$$\phi(\bar{\boldsymbol{S}}, q; \boldsymbol{G}^e) = \widehat{\phi}(\bar{\boldsymbol{S}}; \boldsymbol{G}^e) - \sqrt{\frac{2}{3}}\left[\sigma_y - q\right] , \tag{I.2.15}$$

for the initial yield limit $\sigma_y > 0$ and a positively homogeneous function of degree one (i.e. $\widehat{\phi}(\lambda\bar{\boldsymbol{S}}; \boldsymbol{G}^e) = \lambda\widehat{\phi}(\lambda\bar{\boldsymbol{S}}; \boldsymbol{G}^e)$ for $\lambda \geq 0$). After using Euler's theorem of homogeneous functions, the plastic dissipation reads then,

$$\mathcal{D} = \int_{\mathcal{B}} \sqrt{\frac{2}{3}}\, \gamma\, \sigma_y\, dV \geq 0 , \tag{I.2.16}$$

by the Kuhn-Tucker condition $(\text{I.2.12})_4$. A similar argument gives the non-negative character of the dissipation in (I.2.5) for the viscoplastic case (I.2.13). □

Remark I.2.2 The equation of motion (I.2.1) has also additional conservation laws of momenta given the symmetries in the resulting dynamical system. In this way, for the case of no external loading ($G_{ext} = 0$ and $\partial_\varphi \mathcal{B} = \emptyset$), we have

$$\boldsymbol{l} = \int_{\mathcal{B}} \rho_o \boldsymbol{\varphi} \, dV = constant \quad \text{and} \quad \boldsymbol{j} = \int_{\mathcal{B}} \boldsymbol{\varphi} \times \rho_o \dot{\boldsymbol{\varphi}} \, dV = constant \, , \tag{I.2.17}$$

along the solutions of the problem. The vectors in (I.2.17) correspond to the linear and angular momentum, respectively. Their conservation follows easily by inserting the variations $\delta\boldsymbol{\varphi} = \boldsymbol{c}$ and $\delta\boldsymbol{\varphi} = \boldsymbol{c} \times \boldsymbol{\varphi}$ for all $\boldsymbol{c} \in \mathbb{R}^3$ in (I.2.1), admissible variations for the case considered here. □

I.2.2. The volume change and isochoric plastic models

Metals are known to exhibit no plastic change of volume in the strain ranges of interest. In the finite deformation setting considered in the previous section, the natural volumetric strain is given by

$$\varepsilon_v := \log J \quad \text{for} \quad J = \det[\boldsymbol{F}] \, , \tag{I.2.18}$$

the Jacobian J and its natural logarithm $\log$. The multiplicative decomposition (I.2.2) leads to the additive decomposition

$$\varepsilon_v = \varepsilon_v^e + \varepsilon_v^p \, , \tag{I.2.19}$$

for the elastic and plastic parts

$$\varepsilon_v^e = \log J^e \quad \text{and} \quad \varepsilon_v^p = \log J^p \, , \tag{I.2.20}$$

in terms of the elastic and plastic Jacobians $J^e = \det[\boldsymbol{F}^e]$ and $J^p = \det[\boldsymbol{F}^p]$, respectively.

Fundamental to the developments below are the rate relations

$$\dot{\varepsilon}_v = \frac{1}{2}\dot{\boldsymbol{C}} : \boldsymbol{G} \qquad \text{and} \qquad \dot{\varepsilon}_v^e = \frac{1}{2}\dot{\boldsymbol{C}}^e : \boldsymbol{G}^e \, , \tag{I.2.21}$$

for the total and elastic metrics $\boldsymbol{G}$ and $\boldsymbol{G}^e$ in the reference $\mathcal{O}_X$ and intermediate configurations $\mathcal{O}_X^p$, respectively. Given the plastic strain rate (I.2.6), we can write

$$\boldsymbol{G}^e : \boldsymbol{D}^p = \frac{1}{2}\dot{\boldsymbol{C}} : \left(\boldsymbol{F}^{p^{-1}} \boldsymbol{G}^e \boldsymbol{F}^{p^{-T}}\right) - \frac{1}{2}\dot{\boldsymbol{C}}^e : \boldsymbol{G}^e = \dot{\varepsilon}_v - \dot{\varepsilon}_v^e = \dot{\varepsilon}_v^p \, , \tag{I.2.22}$$

after noting the relation

$$\boldsymbol{G} = \boldsymbol{F}^{p^{-1}} \boldsymbol{G}^e \boldsymbol{F}^{p^{-T}} \, , \tag{I.2.23}$$

as a simple algebraic calculation shows. The general flow rule (I.2.8) leads then

$$\dot{\varepsilon}_v^p = \gamma \, \boldsymbol{N}_{\phi_{\bar{S}}} : \boldsymbol{G}^e \, , \tag{I.2.24}$$

and hence we have

$$J^p \equiv 1 \qquad \text{if} \qquad \boldsymbol{N}_{\phi_{\bar{S}}} : \boldsymbol{G}^e = 0 \,, \tag{I.2.25}$$

recovering the desired isochoric character of the plastic flow when this last condition holds. It is the goal of this work to develop integration algorithms for the plastic evolution equations (I.2.8)-(I.2.10) that conforms with this estimate while exhibiting the energy dissipation (I.2.5) and the momentum conservation laws discussed in Remark I.2.2.

Relation (I.2.23) allows also to define the plastic deformation gradient $\boldsymbol{F}^p$ in terms of the metrics $\boldsymbol{G}$ and $\boldsymbol{G}^e$. Indeed, introducing the polar decompositions

$$\boldsymbol{F} = \boldsymbol{R}\boldsymbol{U} \qquad \text{and} \qquad \boldsymbol{F}^e = \boldsymbol{R}^e\boldsymbol{U}^e \,, \tag{I.2.26}$$

we can write

$$\boldsymbol{F}^p = \boldsymbol{G}^{e^{1/2}} \boldsymbol{\Lambda}\, \boldsymbol{G}^{-1/2} \quad \text{for the rotation} \quad \boldsymbol{\Lambda} = \boldsymbol{R}^{e^T} \boldsymbol{R} \,, \tag{I.2.27}$$

as a simple calculation shows.

Remark I.2.3 A typical example of isochoric plastic model is given by the von Mises yield function, written in the form (I.2.15) with

$$\begin{aligned} \widehat{\phi}(\bar{\boldsymbol{S}}; \boldsymbol{G}^e) &= \sqrt{\boldsymbol{G}^{e^{-1}}\ \mathrm{DEV}_{G^e}[\bar{\boldsymbol{S}}] : \mathrm{DEV}_{G^e}[\bar{\boldsymbol{S}}]\ \ \boldsymbol{G}^{e^{-1}}} \\ &= \sqrt{\mathrm{dev}\,[\boldsymbol{\tau}] : \mathrm{dev}\,[\boldsymbol{\tau}]} = \|\mathrm{dev}\,[\boldsymbol{\tau}]\,\| \,, \end{aligned} \tag{I.2.28}$$

where we have introduced the deviatoric part of the stress $\bar{\boldsymbol{S}}$ in the intermediate configuration $\mathcal{O}_X^p$

$$\mathrm{DEV}_{G^e}[\bar{\boldsymbol{S}}] = \bar{\boldsymbol{S}} - \frac{1}{3}\ \left(\bar{\boldsymbol{S}} : \boldsymbol{G}^{e^{-1}}\right)\ \boldsymbol{G}^e \,, \tag{I.2.29}$$

in the metric $\boldsymbol{G}^e$ of that configuration, and the corresponding classical deviatoric part in the current configuration

$$\mathrm{dev}\,[\boldsymbol{\tau}] = \boldsymbol{F}^e\ \mathrm{DEV}_{G^e}[\bar{\boldsymbol{S}}]\ \boldsymbol{F}^{e^T} = \boldsymbol{\tau} - \frac{1}{3}\ (\boldsymbol{\tau} : \boldsymbol{1})\ \boldsymbol{1} \,, \tag{I.2.30}$$

of the Kirchhoff stresses $\boldsymbol{\tau} = \boldsymbol{F}\boldsymbol{S}\boldsymbol{F}^T = \boldsymbol{F}^e\bar{\boldsymbol{S}}\boldsymbol{F}^{e^T}$. The associated plastic flow vector is then given by

$$\boldsymbol{N}_{\phi_{\bar{S}}} = \frac{\partial \widehat{\phi}}{\partial \bar{\boldsymbol{S}}} = \frac{1}{\widehat{\phi}}\ \boldsymbol{G}^{e^{-1}}\ \mathrm{DEV}_{G^e}[\bar{\boldsymbol{S}}]\ \ \boldsymbol{G}^{e^{-1}} = \boldsymbol{F}^{e^T}\, \frac{\mathrm{dev}\,[\boldsymbol{\tau}]}{\|\mathrm{dev}\,[\boldsymbol{\tau}]\,\|} \boldsymbol{F}^e \,, \tag{I.2.31}$$

which can be easily seen to satisfy the condition (I.2.25). □

I.3. Volume-Preserving Energy-Dissipative Momentum-Conserving Schemes

We develop in this section the new EDMC scheme for the integration of the plasticity problem summarized in the previous section. Section I.3.1 presents general energy-dissipative momentum-conserving approximations in this context, while Section I.3.2 discusses approximations of the corresponding geometric structure that, in addition, preserves the volume change of the plastic flow. Section I.3.3 discusses briefly the numerical implementation of the resulting scheme.

I.3.1. Energy-dissipative momentum-conserving approximations

The interest here is the development of one-step time-stepping algorithms for the solution of the governing equation (I.2.1). To this purpose, we consider the general approximation

$$\boldsymbol{\varphi}_{n+1} - \boldsymbol{\varphi}_n = \Delta t\ \boldsymbol{v}_* \tag{I.3.1}$$

$$\int_{\mathcal{B}} \left[\rho_o \frac{\boldsymbol{v}_{n+1} - \boldsymbol{v}_n}{\Delta t} \cdot \delta\boldsymbol{\varphi} + \boldsymbol{S}_* : \left(\boldsymbol{F}_*^T \mathrm{GRAD}(\delta\boldsymbol{\varphi}) \right)^s \right] dV = G_{ext_*} \tag{I.3.2}$$

for all admissible variations $\delta\boldsymbol{\varphi}$ in a generic time step $[t_n, t_{n+1}]$ with $\Delta t = t_{n+1} - t_n$ and a generic second-order approximation of the external loading (say the original G_{ext} evaluated at the mid-point $(t_n + t_{n+1})/2$). The quantities $(\cdot)_*$ need to be defines such that the conservation/dissipation laws described in the previous section are inherited by the discrete equations (I.3.1)-(I.3.2).

The conservation of linear momentum ($\boldsymbol{l}_{n+1} = \boldsymbol{l}_n$) for no external loading is trivially satisfied as it corresponds to the discrete equation (I.3.1). Following an argument completely analogous to the one discussed in Remark I.2.2 leading to the conservation laws (I.2.17) for the continue, we obtain the conservation law of angular momentum (i.e. $\boldsymbol{j}_{n+1} = \boldsymbol{j}_n$ for no external loading) for a symmetric stress tensor $\boldsymbol{S}_*$ and the choice

$$\boldsymbol{F}_* = \boldsymbol{F}_{n+\frac{1}{2}} = \frac{1}{2}\left(\boldsymbol{F}_n + \boldsymbol{F}_{n+1}\right) \quad \text{and} \quad \boldsymbol{v}_* \parallel \boldsymbol{v}_{n+\frac{1}{2}} = \frac{1}{2}\left(\boldsymbol{v}_n + \boldsymbol{v}_{n+1}\right)\ , \tag{I.3.3}$$

as an algebraic calculation shows; see Simo & Tarnow [1992], Armero & Romero [2001a]. The fact that the velocity approximation $\boldsymbol{v}_*$ needs only to be a vector parallel to the mid-point value $\boldsymbol{v}_{n+\frac{1}{2}}$ has been exploited in Armero & Romero [2001a], Armero & Romero [2001b]] as a way to introduce numerical dissipation to handle the high numerical stiffness of the system of equations (I.3.1)-(I.3.2).

Similarly, following the same arguments leading to the energy evolution equation (I.2.5), we obtain for the case of no external loading ($G_{ext} = 0$ and $\partial_\varphi \mathcal{B} = \emptyset$) the incremental energy relation

$$H_{n+1} - H_n = \int_{\mathcal{B}} \left[\left(W^e_{n+1} - W^e_n \right) - \bar{\boldsymbol{S}}_* : \frac{1}{2}\Delta \boldsymbol{C}^e \right] dV$$

$$\underbrace{-\int_{\mathcal{B}} \left[\bar{\boldsymbol{S}}_* : \frac{1}{2} \left(\boldsymbol{F}_*^{p^{-T}} \Delta \boldsymbol{C} \boldsymbol{F}_*^{p^{-1}} - \Delta \boldsymbol{C}^e \right) + q_* \Delta \alpha \right] dV}_{\hat{\mathcal{D}}} , \tag{I.3.4}$$

for the total energy $H_\ni$ ($i = \{0, 1\}$) defined in (I.2.5), after introducing the stress

$$\bar{\boldsymbol{S}}_* = \boldsymbol{F}_*^p \boldsymbol{S}_* \boldsymbol{F}_*^{p^T} , \tag{I.3.5}$$

for some approximation $\boldsymbol{F}_*^p$ defining the discrete intermediate configuration $\mathcal{O}_{X*}^p$, and the hardening variable

$$q_* = -\frac{\mathcal{H}_{n+1} - \mathcal{H}_n}{\alpha_{n+1} - \alpha_n} , \tag{I.3.6}$$

so $q_* \Delta \alpha = \Delta \mathcal{H}$. Here, we have used the notation $\Delta(\cdot) = (\cdot)_{n+1} - (\cdot)_n$.

A first step in recovering the continuum estimate (I.2.5) consists in the proper approximation of the stress formula $(\text{I.2.3})_2$ so the first integral of the right-hand-side of (I.3.4) vanishes (or it is negative to account for numerical dissipation; see Remark I.3.1 below). Here we consider the discrete formula

$$\boxed{\bar{\boldsymbol{S}}_* = \bar{\boldsymbol{S}}(\boldsymbol{C}^e_{n+\frac{1}{2}}) + 2 \frac{W^e(\boldsymbol{C}^e_{n+1}) - W^e(\boldsymbol{C}^e_n) - \bar{\boldsymbol{S}}(\boldsymbol{C}^e_{n+\frac{1}{2}}) : \frac{1}{2} \Delta \boldsymbol{C}^e}{\boldsymbol{G}^e_* \Delta \boldsymbol{C}^e : \Delta \boldsymbol{C}^e \boldsymbol{G}^e_*} \boldsymbol{G}^e_* \Delta \boldsymbol{C}^e \boldsymbol{G}^e_*} \tag{I.3.7}$$

for an approximation of the elastic metric $\boldsymbol{G}^e_*$ as developed in the next section. Here $\bar{\boldsymbol{S}}(\boldsymbol{C}^e_{n+\frac{1}{2}})$ denotes the gradient formula $(\text{I.2.3})_2$ evaluated at $\boldsymbol{C}^e_{n+\frac{1}{2}} = (\boldsymbol{C}^e_n + \boldsymbol{C}^e_{n+1})/2$. The stress formula (I.3.7) can be seen to be a projection of this value to give the incremental elastic strain energy when contracted with $\frac{1}{2}\Delta \boldsymbol{C}^e$. It is a modification of the formula originally proposed in GONZÁLEZ [2000] accounting for the presence of the elastic metric $\boldsymbol{G}^e_*$, hence leading to a properly invariant formula. We note that the denominator in (I.3.7) only vanishes when $\Delta \boldsymbol{C}^e$ does since

$$\boldsymbol{G}^e_* \Delta \boldsymbol{C}^e : \Delta \boldsymbol{C}^e \boldsymbol{G}^e_* = \| \boldsymbol{G}_*^{e^{1/2}} \Delta \boldsymbol{C}^e \boldsymbol{G}_*^{e^{1/2}} \|^2 \geq 0 , \tag{I.3.8}$$

given the positive-definite character of the metric $\boldsymbol{G}^e_*$. Therefore, the second-term in (I.3.7) vanishes when $\Delta \boldsymbol{C}^e = 0$.

The key aspect of the discrete energy evolution (I.3.4) is that it reveals the proper approximation of the plastic strain rate (I.2.6) so the exact energy dissipation is recovered. Indeed, following the same arguments as for the continuum problem we consider the discrete plastic evolution equations

$$\boxed{\left.\begin{aligned} \tfrac{1}{2} \left[\boldsymbol{F}_*^{p^{-T}} \Delta \boldsymbol{C} \boldsymbol{F}_*^{p^{-1}} - \Delta \boldsymbol{C}^e \right] &= \Delta\gamma \, \boldsymbol{N}_{\phi_{\bar{S}}}(\bar{\boldsymbol{S}}_*, q_*; \boldsymbol{G}^e_*) \\ \text{skew} \left[\boldsymbol{G}_*^{e^{-1}} \left(\boldsymbol{F}^p_{n+1} - \boldsymbol{F}_n \right) \boldsymbol{F}_*^{p^{-1}} \right] &= \Delta\gamma \, \widehat{\boldsymbol{M}}_{W^p}(\bar{\boldsymbol{S}}_*, q_*; \boldsymbol{G}^e_*) \\ \alpha_{n+1} - \alpha_n &= \Delta \, \gamma \, n_{\phi_q}(\bar{\boldsymbol{S}}_*, q_*; \boldsymbol{G}^e_*) \end{aligned}\right\}} \tag{I.3.9}$$

for the discrete plastic multiplier $\Delta\gamma$ defined by the loading/unloading conditions

$$\phi_* = \phi(\bar{\boldsymbol{S}}_*, q_*; \boldsymbol{G}^e_*) \leq 0 \ , \quad \Delta\gamma \geq 0 \quad \Delta\gamma \ \phi_* = 0 \ . \tag{I.3.10}$$

As in the continuum case, these relations are replaced for a viscoplastic model of the form (I.2.13) by

$$\Delta\gamma = \frac{g(\phi_*)}{\eta} \ , \tag{I.3.11}$$

where ϕ_* is defined by $(\text{I.3.10})_1$.

The flow vectors in the left-hand-side of the discrete plastic evolution equations (I.3.9) are defined by the assumed plastic model. The inclusion of these equations in the energy evolution equation (I.3.4) leads to the exact energy dissipation for the discrete equations. In particular, for the associated plastic models based on yield functions of the form (I.2.15) we recover

$$\widehat{\mathcal{D}} = \int_{\mathcal{B}} \sqrt{\frac{2}{3}} \ \Delta\gamma \ \sigma_y \ dV \geq 0 \ , \tag{I.3.12}$$

thus recovering (I.2.16), and resulting in the exact energy conservation for elastic steps ($\Delta\gamma = 0$). We note that these dissipation/conservation properties hold for any approximation of the metric $\boldsymbol{G}^e_*$ and the plastic deformation gradient $\boldsymbol{F}^p_*$ defining the discrete intermediate configuration $\mathcal{O}^p_{X*}$. A second-order approximation is given by the values

$$\boldsymbol{F}^p_* = \frac{1}{2}\left(\boldsymbol{F}^p_n + \boldsymbol{F}^p_{n+1}\right) \quad \text{and} \quad \boldsymbol{G}^e_* = \left(\boldsymbol{C}^e_{n+\frac{1}{2}}\right)^{-1} \ , \tag{I.3.13}$$

as originally proposed in Armero [2006]. We develop alternative definitions of these quantities that lead to the proper treatment of the plastic volume in the next section.

Remark I.3.1 We refer to Armero [2006] for a discussion on additional considerations for the inclusion of a controllable high-frequency energy dissipation along the lines of the EDMC methods proposed in Armero & Romero [2001a], Armero & Romero [2001b]] for nonlinear elastodynamics. □

Remark I.3.2 For simplicity in the presentation, we have considered the semi-discrete in time equations (I.3.1)-(I.3.2). However, the fully discrete equations, accounting for the spatial discretization, need to be considered. The basic displacement finite element model is trivially recovered from (I.3.1)-(I.3.2). However, this basic approach is known to lead to locking in the considered elastoplastic context, as first noted in Nagtegaal et al [1974]. The simulations presented in Section I.4 consider the mixed treatment presented in González [2000] adapted to the elastoplastic problem considered here. Alternative assumed strain treatments preserving the conservation/dissipation properties of the momenta and energy can be found in Armero [2008]. The very same conservation/dissipation properties of the time discrete schemes, the interest in this paper, apply to these cases. □

I.3.2. The discrete geometric structure

It remains to define the proper geometric structure of the discrete equations so the volumetric properties of the continuum plastic flow are preserved. The key aspect is given by the relations (I.2.21), whose discrete analog we seek. That is, we require that the discrete metrics $\boldsymbol{G}_*$ and $\boldsymbol{G}^e_*$ in the reference and intermediate configurations, respectively, satisfy the incremental relations

$$\Delta\varepsilon_v = \frac{1}{2}\Delta\boldsymbol{C} : \boldsymbol{G}_* \qquad \text{and} \qquad \Delta\varepsilon^e_v = \frac{1}{2}\Delta\boldsymbol{C}^e : \boldsymbol{G}^e_* \,, \tag{I.3.14}$$

for the increments of total and elastic volumetric strains in (I.2.20), while defining a second-order approximation of the continuum values $\boldsymbol{C}^{-1}$ and $\boldsymbol{C}^{e^{-1}}$, respectively.

Following the same strategy as for the stresses in the previous section, we consider a mid-point approximation of these values with a projection term enforcing the relations (I.3.14). In this way, we define

$$\boxed{\boldsymbol{G}_* = \boldsymbol{C}^{-1}_{n+\frac{1}{2}} + 2\frac{\log\left(J_{n+1}/J_n\right) - \boldsymbol{C}^{-1}_{n+\frac{1}{2}} : \frac{1}{2}\Delta\boldsymbol{C}}{\boldsymbol{C}^{-1}_{n+\frac{1}{2}}\Delta\boldsymbol{C} : \Delta\boldsymbol{C}\, \boldsymbol{C}^{-1}_{n+\frac{1}{2}}}\boldsymbol{C}^{-1}_{n+\frac{1}{2}}\Delta\boldsymbol{C}\, \boldsymbol{C}^{-1}_{n+\frac{1}{2}}} \tag{I.3.15}$$

for the metric in the reference configuration $\mathcal{O}_{X*}$, with $\boldsymbol{C}_{n+\frac{1}{2}} = (\boldsymbol{C}_n + \boldsymbol{C}_{n+1})/2$ and its inverse $\boldsymbol{C}^{-1}_{n+\frac{1}{2}}$, $J_{n+1} = \left(\det\left[\boldsymbol{C}_{n+1}\right]\right)^{1/2}$ and $J_n = \left(\det\left[\boldsymbol{C}_n\right]\right)^{1/2}$ and

$$\boxed{\boldsymbol{G}^e_* = \boldsymbol{C}^{e^{-1}}_{n+\frac{1}{2}} + 2\frac{\log\left(J^e_{n+1}/J^e_n\right) - \boldsymbol{C}^{e^{-1}}_{n+\frac{1}{2}} : \frac{1}{2}\Delta\boldsymbol{C}^e}{\boldsymbol{C}^{e^{-1}}_{n+\frac{1}{2}}\Delta\boldsymbol{C}^e : \Delta\boldsymbol{C}^e\, \boldsymbol{C}^{e^{-1}}_{n+\frac{1}{2}}}\boldsymbol{C}^{e^{-1}}_{n+\frac{1}{2}}\Delta\boldsymbol{C}^e\, \boldsymbol{C}^{e^{-1}}_{n+\frac{1}{2}}} \tag{I.3.16}$$

for the metric in the intermediate configuration $\mathcal{O}^p_X$, with $\boldsymbol{C}^e_{n+\frac{1}{2}} = (\boldsymbol{C}^e_n + \boldsymbol{C}^e_{n+1})/2$ and its inverse $\boldsymbol{C}^{e^{-1}}_{n+\frac{1}{2}}$, $J^e_{n+1} = \left(\det\left[\boldsymbol{C}^e_{n+1}\right]\right)^{1/2}$ and $J^e_n = \left(\det\left[\boldsymbol{C}^e_n\right]\right)^{1/2}$. We note again that the denominators in these expressions are well-defined, vanishing when the respective numerators vanish, that is, when $\Delta\boldsymbol{C}$ and $\Delta\boldsymbol{C}^e$ vanish, respectively.

The use of the metrics (I.3.15) and (I.3.16) in combination with the discrete flow rule $(\text{I.3.9})_1$ leads directly to the relation

$$\begin{aligned}\Delta\gamma\ \boldsymbol{N}_{\phi_{\bar{S}}} : \boldsymbol{G}^e_* &= \frac{1}{2}\Delta\boldsymbol{C} : \left(\boldsymbol{F}^{p^{-1}}_* \boldsymbol{G}^e_* \boldsymbol{F}^{p^{-T}}_*\right) - \frac{1}{2}\Delta\boldsymbol{C}^e : \boldsymbol{G}^e_* \\ &= \frac{1}{2}\Delta\boldsymbol{C} : \boldsymbol{G}_* - \frac{1}{2}\Delta\boldsymbol{C}^e : \boldsymbol{G}^e_* = \Delta\varepsilon - \Delta\varepsilon^e = \Delta\varepsilon^p \,,\end{aligned} \tag{I.3.17}$$

the complete analog of the continuum relation (I.2.24), as long as (I.2.23) holds in this discrete setting, that is, as long as $\boldsymbol{G}_* = \boldsymbol{F}^{p^{-1}}_* \boldsymbol{G}^e_* \boldsymbol{F}^{p^{-T}}_*$. This is obtained by considering the approximation of the continuum relation (I.2.27) given by

$$\boxed{\boldsymbol{F}^p_* = \boldsymbol{G}^{e^{1/2}}_* \boldsymbol{\Lambda}_* \boldsymbol{G}^{-1/2}_* \qquad \text{with} \qquad \boldsymbol{\Lambda}_* = \left(\boldsymbol{\Lambda}_{n+1}\boldsymbol{\Lambda}^T_n\right)^{1/2}\boldsymbol{\Lambda}_n \,.} \tag{I.3.18}$$

The rotation $\boldsymbol{\Lambda}_*$ corresponds to a second-order interpolation of the rotation $\boldsymbol{\Lambda}$ in (I.2.27) from the end values $\boldsymbol{\Lambda}_n = \boldsymbol{R}_n^{e^T}\boldsymbol{R}_n$ and $\boldsymbol{\Lambda}_{n+1} = \boldsymbol{R}_{n+1}^{e^T}\boldsymbol{R}_{n+1}$. Formula $(I.3.18)_2$ can be efficiently implemented (with algebraic operations only) using quaternions:

$$\boldsymbol{q}_* = \frac{\boldsymbol{q}_n + \boldsymbol{q}_{n+1}}{\|\boldsymbol{q}_n + \boldsymbol{q}_{n+1}\|} , \tag{I.3.19}$$

for the quaternions $\boldsymbol{q}$ associated to the different rotations $\boldsymbol{\Lambda}$; see SHOEMAKE [1985]. We refer to ARMERO & ZAMBRANA [2007] for complete details, including the linearization of the rotation interpolation formulas (I.3.18) and (I.3.19).

These relations define completely the new volume-preserving energy-dissipative momentum-conserving scheme and prove the following theorem.

Proposition I.3.1 *The one-step time-stepping algorithm defined by the global relations (I.3.1)-(I.3.2) with the stresses $\boldsymbol{S}_*$ defined by (I.3.5) in terms of $\bar{\boldsymbol{S}}_*$ given by the elastic stress formula (I.3.7) and the approximation (I.3.9)-(I.3.10) (or (I.3.9)-(I.3.11) for the viscoplastic case) with the hardening variable q_* defined by (I.3.6) satisfy:*

i. The conservation laws of linear and angular momentum are exactly preserved.

ii. The energy evolves following the relation ($G_{ext} = 0$)

$$H_{n+1} - H_n = -\widehat{\mathcal{D}} , \tag{I.3.20}$$

for the exact physical dissipation $\widehat{\mathcal{D}} \geq 0$, with $\widehat{\mathcal{D}} = 0$ for elastic steps.

iii. The plastic volume is exactly preserved, that is,

$$J^p_{n+1} = J^p_n \equiv 1 \qquad \text{for isochoric plastic models,} \tag{I.3.21}$$

with the last property holding for the approximations (I.3.15) and (I.3.16) of the reference and elastic metrics, respectively, the latter defined in the intermediate configuration $\mathcal{O}^p_{X*}$ determined by the plastic deformation gradient (I.3.18).

Remark I.3.3 Other formulas for the discrete metrics (I.3.15) and (I.3.16) satisfying the relations (I.3.14) are possible. For example, the projection terms can be defined in terms of the metrics themselves, giving an implicit definition of these metrics. Similarly, the stress projection term in the elastic stress formula (I.3.7) can be defined with the value $\boldsymbol{C}^{e^{-1}}_{n+\frac{1}{2}}$ instead of the metric $\boldsymbol{G}^e_*$ and still results in all the properties summarized in Theorem I.3.1. □

Remark I.3.4 We note that the volume-preserving property (I.3.17) is not only important for the isochoric plastic models as emphasized in (I.3.21), but also in models where the plastic volume change is an important physical aspect to capture correctly, like in dilatant models of soil mechanics. □

I.3.3. The numerical implementation

The numerical solution of the discrete plastic evolution equations (I.3.9) can be approached through the common structure of return mapping algorithms consisting of an elastic trial state followed by a plastic corrector if necessary. Some calculations show that the solution for an elastic step $\Delta\gamma = 0$ is given by $\boldsymbol{F}^p_* = \boldsymbol{F}^p_n$. The plastic corrector requires the solution of the system of equations (I.3.9) for $\{\boldsymbol{F}^p_{n+1}, \alpha_{n+1}\}$ while evaluating the stresses $\bar{\boldsymbol{S}}_*$ through (I.3.7) and the hardening variable q_* through (I.3.6).

This solution is efficiently accomplished through a two-level scheme with two nested Newton iterations. The "upper level" iteration drives the residual

$$R_\phi(\alpha_{n+1}) = \phi(\bar{\boldsymbol{S}}_*(\alpha_{n+1}), q_*(\alpha_{n+1}); \boldsymbol{G}^e_*(\alpha_{n+1})) \tag{I.3.22}$$

to zero, solving for the updated equivalent strain α_{n+1} while enforcing the consistency condition (or the equivalent relation for the viscoplastic problem). The evaluation of the stresses and internal variables for a fixed value of α involves the evaluation of the plastic flow and plastic spin rules $(I.3.9)_{1,2}$. These equations are solved for the updated value $\boldsymbol{F}^p_{n+1}$ through the "lower level" Newton iteration driving the residual

$$\boldsymbol{R}_{F^p}(\boldsymbol{F}^p_{n+1}) = \begin{bmatrix} \boldsymbol{F}^{p^{-T}}_* (\boldsymbol{C}_{n+1} - \boldsymbol{C}_n) \boldsymbol{F}^{p^{-1}}_* - (\boldsymbol{C}^e_{n+1} - \boldsymbol{C}^e_n) - 2\Delta\gamma \boldsymbol{N}_{\phi_{\bar{S}}} \\ \\ \text{AXIAL}\left[\boldsymbol{G}^{e^{-1}}_* \left(\boldsymbol{F}^p_{n+1} - \boldsymbol{F}^p_n\right) \boldsymbol{F}^{p^{-1}}_* - \Delta\gamma\, \widehat{\boldsymbol{M}}_{W^p}\right] \end{bmatrix} \tag{I.3.23}$$

to zero with $\Delta\gamma = (\alpha_{n+1} - \alpha_n)/n_{\phi_q}$ for the fixed value α_{n+1} at this lower level. Here we used the notion of the axial vector of a tensor through its skew part (denoted by AXIAL $[\cdot]$), so the residual in (I.3.23) has nine components for the nine components of $\boldsymbol{F}^p_{n+1}$ after noting the symmetry of the first component of the residual in this equation. We refer to ARMERO & ZAMBRANA [2007] for complete details of the numerical implementation, including the consistent tangents in the solution of the problems (I.3.22) and (I.3.23), as well as the global algorithmic consistent tangent used in the construction of the stiffness matrix in typical Newton-Raphson solutions of the global equations (I.3.1)-(I.3.2).

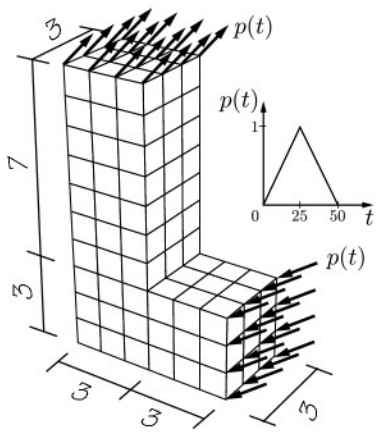

FIGURE I.3.1 Tumbling L-shaped block. Initial configuration and loading with finite element mesh (117 constant volume mixed trilinear bricks).

I.4. Representative Numerical Simulations

To illustrate the numerical properties of the newly developed volume-preserving energy-dissipative momentum-conserving scheme (referred simply in what follows as the EDMC-VP scheme) we consider the problem of a tumbling L-shaped block, first considered in SIMO & TARNOW [1992] in the elastic range and in MENG& LAURSEN [2002],NOELS ET AL [2004] in the context of elastoplasticity. Figure I.3.1 depicts the initial configuration of the block, with its geometry and loading. This consists of point loads at the nodes of the block bases given by

$$\boldsymbol{p}(t) = \begin{cases} \boldsymbol{p}_o \times t & \text{for } 0 \leq t \leq 25, \\ \boldsymbol{p}_o \times (50 - t) & \text{for } 25 \leq t \leq 50, \\ 0 & \text{for } t \geq 50, \end{cases} \tag{I.4.1}$$

for the vector $\boldsymbol{p}_o = [4\ 10\ 12]^T$ and the opposite vector in the opposite base of the block, in the Cartesian system defined by the three orthogonal directions along the block edges. The block is then in free-flight after an initial period of loading. Figure I.3.1 depicts also the assumed finite element discretization, consisting of 117 brick elements. The mixed finite element strategy indicated in Remark I.3.2 has been considered with a piece-wise constant interpolation for the volume in combination with a trilinear displacement interpolation.

We consider J_2-flow theory for the material response, characterized by the von Mises yield function (I.2.28) and the associated flow vectors (I.2.14). Linear isotropic hardening is assumed, that is, $y(\alpha) = \sigma_y - q = \sigma_y + H\alpha$ for the initial yield limit σ_y and linear hardening modulus H. We consider Hencky's law for the hyperelastic response, characterized by the elastic potential

$$W^e(\boldsymbol{C}^e) = \frac{1}{2}\kappa \left(\log J^e\right)^2 + \mu \sum_{A=1}^{3} \left(\widehat{\boldsymbol{\varepsilon}}_A^e\right)^2 \ , \tag{I.4.2}$$

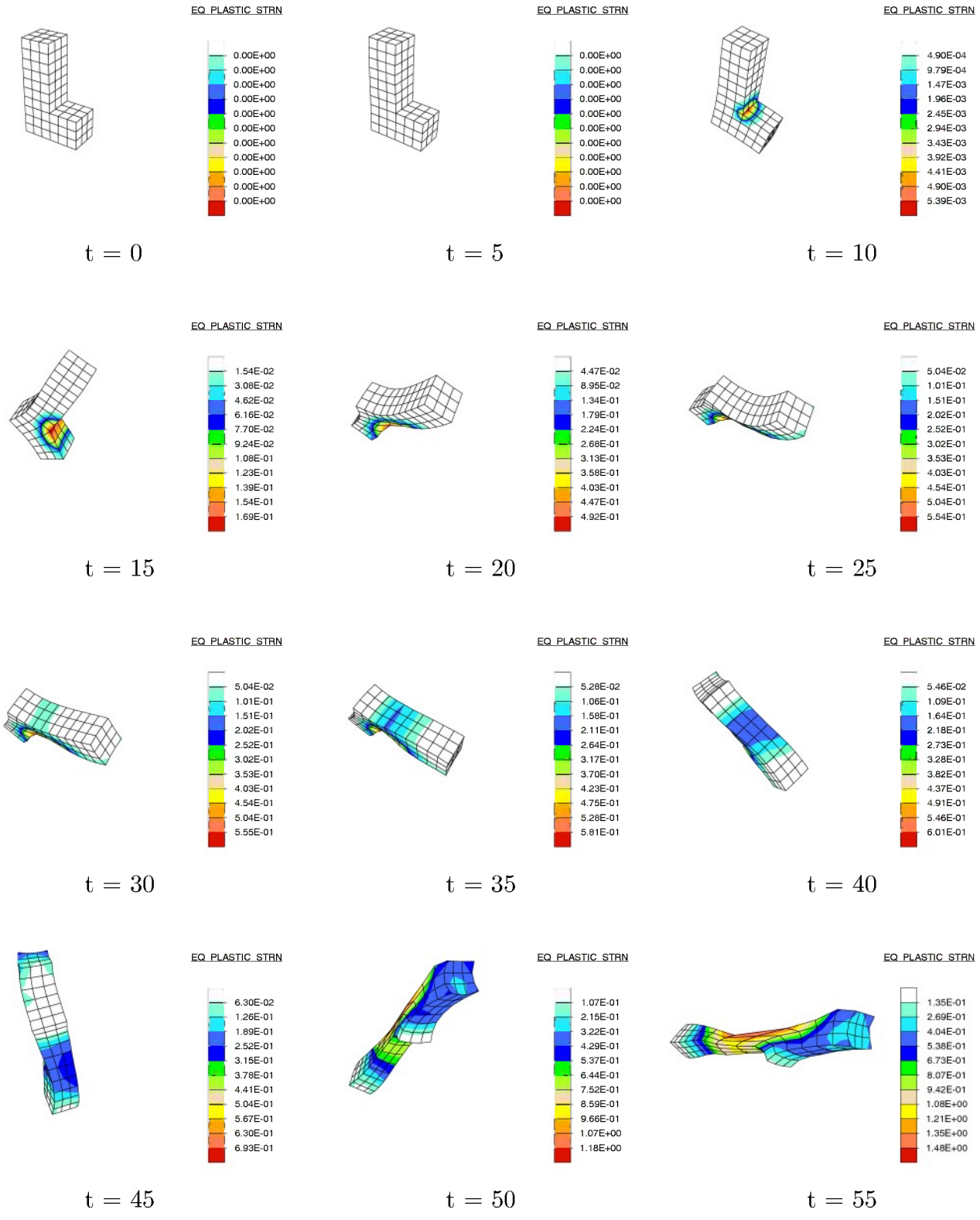

FIGURE I.3.2 Tumbling L-shaped block. Deformed configurations with the distribution of the equivalent plastic strain α during the early stages of the motion computed with the new EDMC-VP scheme.

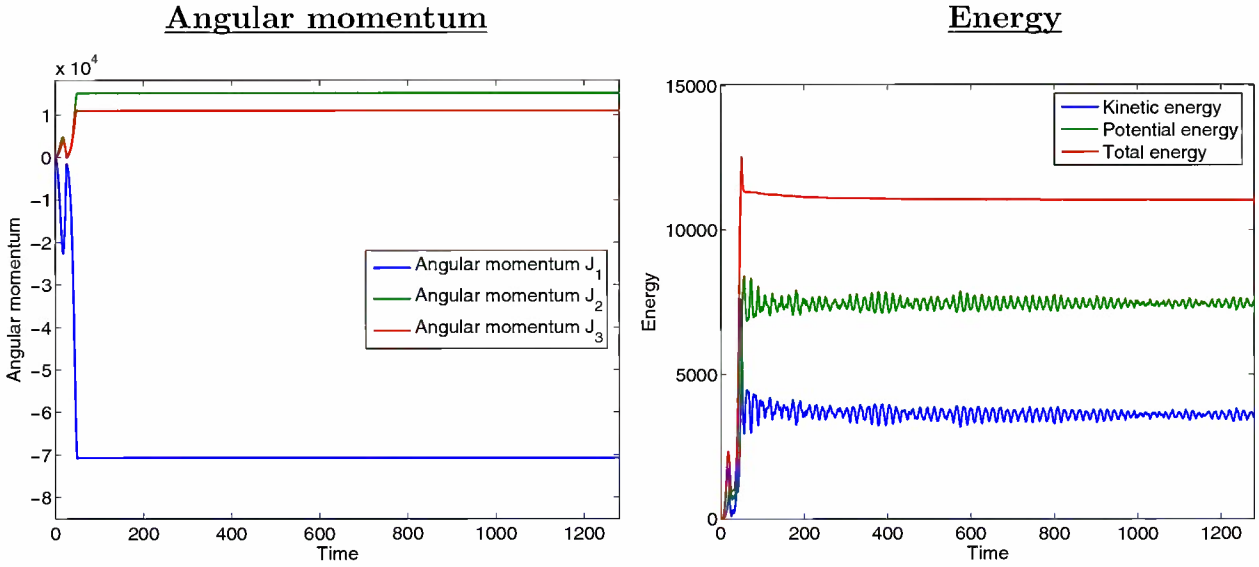

FIGURE I.3.3 Tumbling L-shaped block. Temporal evolution of the three components of the angular momentum (left) and the kinetic, potential and total energies (right) for the solution computed with the new EDMC-VP scheme.

for the bulk and shear moduli κ and μ, respectively, and the regularized logarithmic principal strains

$$\widetilde{\varepsilon}^e_A := \log\left[J^{e^{-1/3}}\lambda^e_A\right] \qquad A = 1, 2, 3\,, \tag{I.4.3}$$

where λ^e_A are the elastic principal stretches defined by the eigenvalues of $\boldsymbol{C}^e$ (i.e. $\boldsymbol{C}^e\boldsymbol{N}_A = (\lambda^e_A)^2\,\boldsymbol{N}_A$, no sum in A). Table I.4.1 includes the values of the different material parameters assumed in the simulations presented here.

We consider several runs at constant time steps Δt. Figure I.3.2 includes several snapshots of the solution computed with the new ENDC-VP scheme with $\Delta t = 0.5$ in the early stages of the motion. The distribution of the equivalent plastic strain α is depicted over the deformed configuration, thus showing the extend of the plasticity. The large displacements and strains involved in the solution are to be noted.

Figure I.3.3 shows the evolution of the three components of the angular momentum $\boldsymbol{j}$ and the energy, including the kinetic and potential energies, for the solution depicted in Figure I.3.2, that is, the solution computed with the new EDMC-VP scheme and a constant time step of $\Delta t = 0.5$. The potential energy consists of the elastic strain energy plus the hardening potential integrated over the solid. The exact conservation of the angular momentum after the initial loading period is confirmed, as it is the conservation of the linear momentum (not shown). Similarly, the monotonic non-negative energy dissipation after this loading period is confirmed by these plots. The plastic volume (not shown) is also confirmed to be exactly preserved at all quadrature points: $J^p \equiv 1$ everywhere and all times for the assumed isochoric model of J_2-flow theory.

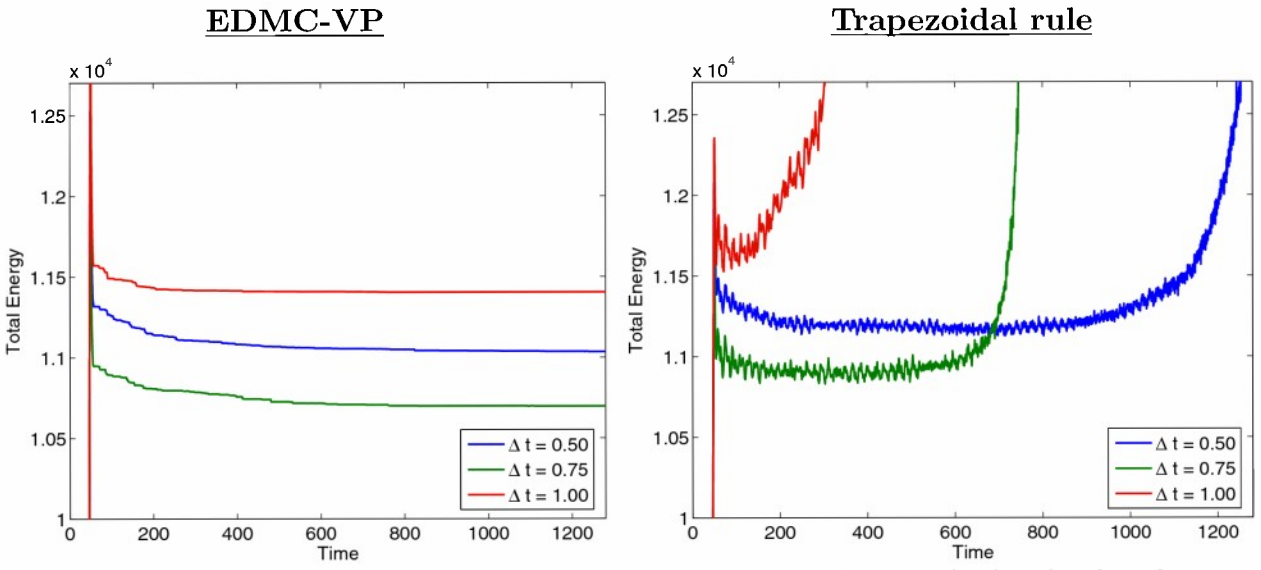

FIGURE I.4.1 Tumbling L-shaped block. Evolution of the total energy in time for the solutions computed with the new EDMC-VP scheme (left) and the classical trapezoidal rule (right) for different time steps. The instabilities of the trapezoidal rule is to be contrasted with the strictly non-negative energy dissipation of the new EDMC-VP scheme.

TABLE I.4.1 Tumbling of a L-shaped block. Material parameters

Bulk modulus	κ	2500
Shear modulus	μ	500
Initial uniaxial yield limit	σ_y	100.0
Linear hardening modulus	H	200
Reference density	ρ_o	100

Table I.4.2 shows the norm of the residual during a typical time step of the global Newton-Raphson scheme employed in the solution of the global nonlinear equations. An asymptotic quadratic rate of convergence is observed, confirming the use of the algorithmic consistent tangent (see ARMERO & ZAMBRANA [2007]). Table I.4.3 includes the residual during the nested Newton iterations of the return mapping in a typical quadrature point undergoing plastic deformation. The "upper level" iteration enforces the consistency condition, requiring the evaluation of the stresses with the corresponding update $\boldsymbol{F}^p_{n+1}$ for a given equivalent plastic strain α. This is done in the "lower level" enforcing the plastic flow and spin rules. A quadratic rate of convergence can be observed, with a maximum of four iterations per level, as all the steps are linearized consistently, easing on the added computational cost involved with the new EDMC-VP scheme. In this respect, we note that a substantial part of this added cost can be traced to the non-symmetry of the algorithmic

TABLE I.4.2 Tumbling of a L-shaped block. Convergence of the Newton-Raphson scheme in a typical time step

1	$2.1521743 \cdot 10^{+03}$
2	$1.6642863 \cdot 10^{+02}$
3	$1.0519854 \cdot 10^{+00}$
4	$1.9821388 \cdot 10^{-04}$
5	$5.5203698 \cdot 10^{-08}$
6	$3.3582068 \cdot 10^{-11}$

TABLE I.4.3 Tumbling of a L-shaped block. Convergence of the two nested Newton schemes to solve the local return mapping equations in a typical quadrature point for a plastic step. The "upper level" iteration imposes consistency, calling the "lower level" to evaluate the stresses and internal variables by enforcing the flow and plastic spin rules.

1	$0.33562 \cdot 10^{+01}$		
		1	$0.12540 \cdot 10^{-01}$
		2	$0.72429 \cdot 10^{-04}$
		3	$0.29601 \cdot 10^{-08}$
		4	$0.14922 \cdot 10^{-12}$
2	$0.35841 \cdot 10^{+00}$		
		1	$0.14982 \cdot 10^{-02}$
		2	$0.10431 \cdot 10^{-05}$
		3	$0.40102 \cdot 10^{-11}$
3	$0.86176 \cdot 10^{-04}$		
		1	$0.36027 \cdot 10^{-06}$
		2	$0.81996 \cdot 10^{-13}$
4	$0.66080 \cdot 10^{-11}$		
		1	$0.27060 \cdot 10^{-13}$

consistent tangent characteristic of energy-momentum schemes, even in elastic problems. An efficient strategy to avoid this unsymmetry, relying on staggered symmetric iterations, can be found in ARMERO & ROMERO [2001b]].

We present in Figure I.4.1 a zoom of the evolution of the total energy computed with different time steps ($\Delta t = 0.5$, 0.75 and 1.00). In all cases, we observe the monotonic dissipation of the new EDMC-VP scheme, confirming the exact energy conservation during elastic steps. These solutions are to be compared with the solution computed with the classical trapezoidal rule (Newmark $\gamma_{NW} = 1/2$ $\beta_{NW} = 1/4$) in combination with an exponential return mapping for the integration of the plastic evolution equations as also

shown in Figure I.4.1; see SIMO [1992],SIMO [1998] for a complete description of the implementation of this classical algorithm. The instabilities of this scheme in the nonlinear range under consideration are clear: a blow up of the energy is observed at a finite time, forcing the stoppage of the of the simulation. The superior, more stable, performance of the new EDMC-VP scheme is concluded.

I.5. Concluding Remarks

We have presented in this paper a new energy-dissipative momentum-conserving time-stepping algorithm for finite strain multiplicative plasticity that also preserves the volume change of the plastic flow. In particular, it reproduces exactly the isochoric plastic response of isochoric plastic models for metals. The new scheme relies on a new integration scheme of the plastic evolution equations (flow and plastic spin rules and hardening law), whose implementation can also be recast in the classical structure of return mapping algorithms consisting of an elastic trial step followed by a plastic corrector. The scheme is constructed by following the discrete analogs of the arguments that build the energy-momentum dissipation/conservation properties in the underlying continuum problem. Similarly, the volume-preserving character is constructed by the proper approximation of the geometric structure behind the multiplicative plasticity models of interest in this work. The new scheme thus developed exhibits the aforementioned dissipation/conservation properties by design, rigorously and independently of the time step and model. In fact, the scheme is completely general, applying to isotropic or anisotropic elastic and/or plastic models of the associated or non-associated type. The improved stability properties of the new scheme have been illustrated for a representative numerical simulation, where standard schemes like the trapezoidal rule exhibit numerical instabilities in the form of an unbounded growth of the energy even in the dissipative plastic range considered here.

References

Armero, F. [2005] "Energy-dissipative momentum-conserving time-stepping algorithms for dynamic finite strain plasticity," Proceedings VIII International Conference on Computational Plasticity, COMPLAS VIII, ed. by E. Oñate and D.R.J. Owen, Barcelona.

Armero, F. [2006] "Energy-dissipative momentum-conserving time-stepping algorithms for finite strain multiplicative plasticity," Computer Methods in Applied Mechanics and Engineering, 195:4862-4889.

Armero, F. [2008] "Assumed Strain Finite Element Methods for Conserving Temporal Integrations in Nonlinear Solid Dynamics," International Journal for Numerical Methods in Engineering, 74:1795-1847.

Armero, F. & Romero, I. [2001a] "On the formulation of high-frequency dissipative time-stepping algorithms for nonlinear dynamics. Part I: Low order methods for two model problems and nonlinear elastodynamics," Computer Methods in Applied Mechanics and Engineering, 190:2603–2649.

Armero, F. & Romero, I. [2001b] "On the formulation of high-frequency dissipative time-stepping algorithms for nonlinear dynamics. Part II: High order methods," Computer Methods in Applied Mechanics and Engineering, 190:6783–6824.

Armero, F. & Zambrana, C. [2007] "Volume–preserving energy–dissipative momentum–conserving algorithms for isochoric multiplicative plasticity," Computer Methods in Applied Mechanics and Engineering, 196:4130-4159.

Crisfield, M. & Shi, J. [1994] "A co-rotational element/time-integration strategy for non-linear dynamics," International Journal for Numerical Methods in Engineering, 37:1897-1913.

Cuitinho, A.M. & Ortiz, M. [1992] "A material independent method for extending stress update algorithms form small strain plasticity to finite plasticity with multiplicative kinematics," Engineering Computations, 17:437–451.

Eterovich, A.L. & Bathe, K.J. [1990] "A hyperelastic based large strain elasto-plastic constitutive formulation with combined isotropic-kinematic hardening using logarithmic stresses and strain measures," International Journal for Numerical Methods in Engineering, 30:1099–1115.

González, O. [2000] "Exact energy-momentum conserving algorithms for general models in nonlinear elasticity," Computer Methods in Applied Mechanics and Engineering, 190:1763–1783.

Hughes, T.J.R. [1987] The Finite Element Method,, Prentice-Hall.

Kuhl, D. & Crisfield, M.A. [1997] "Energy Conserving and Decaying Algorithms in Non-Linear Structural Dynamics," International Journal for Numerical Methods in Engineering,, 45:569-599.

Kuhl, D. & Ramm, E. [1996] "Constraint Energy Momentum Algorithm and its Application to Non-Linear Dynamics of Shells," Computer Methods in Applied Mechanics and Engineering, 136:293-315.

Meng, X.N. & Laursen, T.A. [2002] "Energy consistent algorithms for dynamic finite deformation plasticity," Computer Methods in Applied Mechanics and Engineering, 191:1639-1675.

Nagtegaal, J.C.; Parks, D.M & Rice, J.R. [1974] "On numerically accurate finite element solutions in the fully plastic range," Computer Methods in Applied Mechanics and Engineering, 4:153–177.

Newmark, N.M. [1959] "A Method of Computation for Structural Dynamics," ASCE J. Eng. Mech., 85:67–94.

Noels, L.; Stainier, L. & Ponthot, J.P. [2004] "An Energy-Momentum Conserving Algorithm for Non-Linear Hypoelastic Constitutive Models," International Journal for Numerical Methods in Engineering, 59:83–114.

Shoemake, K. [1985] "Amimating rotations with quaternion curves," Proceedings of the 12th annual international conference on computer graphics and interactive techniques SIGGRAPH'85, ACM, 19:245-254.

Simo, J.C. [1992] "Algorithms for static and dynamic multiplicative plasticity that preserve the classical return mapping schemes of the infinitesimal theory," Computer Methods in Applied Mechanics and Engineering, 90:61-112.

Simo, J.C. [1998] "Numerical Analysis of Classical Plasticity," Handbook for Numerical Analysis, Volume IV,, ed. by P.G. Ciarlet and J.J. Lions, Elsevier, Amsterdam.

Simo, J.C. & Tarnow, N. [1992] "The discrete energy–momentum method. conserving algorithms for nonlinear elastodynamics," ZAMP, 43:757-793.

Weber, G. & Anand, L. [1990] "Finite deformation constitutive equations and time integration procedure for isotropic hyperelastic-viscoelastic solids," Computer Methods in Applied Mechanics and Engineering, 79:173–202.

APPENDIX II

Assumed Strain Finite Element Methods for Conserving Time-Stepping Algorithms

Based on the papers:

Armero, F. [2008] "Assumed Strain Finite Element Methods for Conserving Temporal Integrations in Nonlinear Solid Dynamics," *International Journal for Numerical Methods in Engineering,* 74, 1795-1847.

Armero, F. [2007] "Energy-Momentum Algorithms for Nonlinear Solid Dynamics and their Assumed Strain Finite Element Formulation," Proc. COMPDYN07, Rethymno, Greece.

II.1. Introduction

Classical time-stepping algorithms, like the Newmark or HHT schemes, developed originally in the context of linear elastodynamics, are known to lead to severe numerical instabilities in the nonlinear finite deformation range, even for schemes that are unconditionally stable in the linear range; see e.g. Simo & Tarnow [1992], Armero & Romero [2001a], among others, or the results presented here. These instabilities are characterized by an unbounded growth of the energy, and have been observed even in the context of elastoplastic models (Meng & Laursen [2002], Armero [2006]). This situation, and the lack of the conservation law of angular momentum in many of these classical schemes, has motivated a large amount of recent literature on the formulation of the so-called energy-momentum schemes. These schemes inherit the conservation laws of energy and momenta of the underlying physical system by design.

We refer to Simo & Tarnow [1992], Crisfield & Shi [1994], González [2000] for an illustration of energy-momentum methods in nonlinear elastic problems, and to Meng & Laursen [2002], Noels et al [2004], Armero [2006], Armero & Zambrana [2007] for formulations considering the elastoplastic range where the goal is to capture the exact plastic dissipation (with exact conservation for elastic steps) while still preserving the momentum conservation laws. Extensions of these methods to incorporate an additional controllable numerical energy dissipation in the high-frequency range in order to handle the characteristic numerical stiffness of typical mechanical and structural system of interest have been proposed in Armero & Romero [2001a], Armero & Romero [2001b] for nonlinear continuum elastodynamics and in Armero & Romero [2003], Romero & Armero [2002] in the context of rod and shell Cosserat models of nonlinear structural dynamics. We refer to these time-stepping algorithms as EDMC schemes (for **E**nergy-**D**issipative **M**omentum-**C**onserving). They include, as a particular case, some of the aforementioned energy-momentum schemes.

All these references consider the finite element method for the spatial discretization. The consideration of a nearly incompressible material response, like the one observed in plastically deforming metals and captured by classical elastoplastic models of J_2-flow theory, requires the consideration of finite element formulations more sophisticated than the basic displacement model to avoid the characteristic volumetric locking of this basic formulation. To this end, the so-called assumed strain approach, as developed originally by Nagtegaal et al [1974], Hughes [1980] in the infinitesimal range and Simo et al [1988],Armero [2000] in the finite deformation range (both for static problems), becomes very convenient as it only requires the proper definition of the numerical approximation of the strains and their variations regardless of the material model under consideration. In the continuum nearly incompressible context of interest here, these formulations are also known as "B-bar" methods.

B-bar methods that lead to locking-free finite elements in general configurations are

well-known by now, including general linear and quadratic quadrilateral and triangular elements for two dimensional problems, and similarly in 3D. Unfortunately, their direct consideration in the dynamic range of interest here destroys completely the conservation/dissipation properties outlined above when used in combination of the aforementioned energy-momentum or EDMC schemes. These time-stepping algorithms rely on specific incremental properties of the linearized strain operator appearing in the equation of motion for a typical time step, properties that a straightforward evaluation of the B-bar operator, say at the mid-point, does not have. This situation can be traced back to the nonlinear definition of the assumed deformation gradient defining the assumed strain. For the incompressible limit of interest here, the assumed deformation gradient involves a nonlinear scaling with its determinant or Jacobian (another nonlinear operation) and the assumed Jacobian defined through a weighted average over the element.

All these considerations lead to the need of a new B-bar operator if the fundamental conservation laws of energy and momentum are to be preserved. The new operator needs to account not only for the discrete finite element interpolations in space, but also the discrete structure in time of the EDMC time-stepping algorithms, as presented in this paper.

II.2. The governing equations and their conservation laws

We consider a solid $\mathcal{B} \subset \mathbb{R}^{n_{\rm dim}}$ ($n_{\rm dim} = 1, 2$ or 3) and its motions $\boldsymbol{\varphi}(\boldsymbol{X}, t)$ in time t for the material particles $\boldsymbol{X} \in \mathcal{B}$, which satisfy the weak equation

$$\int_{\mathcal{B}} \rho_o \ddot{\boldsymbol{\varphi}} \cdot \delta\boldsymbol{\varphi}\, dV + \int_{\mathcal{B}} \boldsymbol{S} : \underbrace{\left(\boldsymbol{F}^T \mathrm{GRAD}\,[\delta\boldsymbol{\varphi}]\right)^s}_{=:\frac{1}{2}\delta\boldsymbol{C}(\boldsymbol{\varphi},\delta\boldsymbol{\varphi})} dV = \int_{\mathcal{B}} \rho_o \boldsymbol{b} \cdot \delta\boldsymbol{\varphi}\, dV + \int_{\mathcal{B}} \overline{\boldsymbol{T}} \cdot \delta\boldsymbol{\varphi}\, dA\ , \quad \text{(II.2.1)}$$

for all admissible variations $\delta\boldsymbol{\varphi}$, that is, $\delta\boldsymbol{\varphi} = 0$ on the part of boundary $\partial_\varphi\mathcal{B}$ with imposed deformation $\boldsymbol{\varphi} = \overline{\boldsymbol{\varphi}}$, complementary to the part of the boundary $\partial_t\mathcal{B}$ in (II.2.1) where the tractions $\overline{\boldsymbol{T}}$ are imposed. We have introduced in (II.2.1) the reference density of the solid ρ_o, the acceleration $\ddot{\boldsymbol{\varphi}} = \partial^2\boldsymbol{\varphi}/\partial t^2$, the specific body force $\boldsymbol{b}$ and the second Piola-Kirchhoff stress tensor $\boldsymbol{S}$, a symmetric tensor in the reference configuration $\mathcal{B}$ of the solid. We observe the appearance of the conjugate variations $\delta\boldsymbol{C}/2$ of the right Cauchy-Green tensor $\boldsymbol{C} = \boldsymbol{F}^T\boldsymbol{F}$ for the deformation gradient $\boldsymbol{F} = \mathrm{GRAD}\,[\boldsymbol{\varphi}]$.

The particular form of the governing equation (II.2.1) leads to a number of physical conservation laws, very characteristic of the motions of solids and structures. In particular, denoting the velocity field by $\boldsymbol{V} = \dot{\boldsymbol{\varphi}}$, we easily obtain for the case of a free solid for brevity (i.e. for $\boldsymbol{b} = 0$, $\overline{\boldsymbol{T}} = 0$ and $\partial_\varphi\mathcal{B} = \emptyset$) the conservation laws

$$\boldsymbol{l} := \int_{\mathcal{B}} \rho_o \boldsymbol{V}\, dV = \textit{constant} \qquad \text{and} \qquad \boldsymbol{j} := \int_{\mathcal{B}} \boldsymbol{\varphi} \times \rho_o \boldsymbol{V}\, dV = \textit{constant}, \quad \text{(II.2.2)}$$

corresponding to the linear and angular momentum, respectively, after using the crucial properties

$$\delta \boldsymbol{C}(\boldsymbol{\varphi}, \boldsymbol{c}) = 0 \qquad \text{and} \qquad \delta \boldsymbol{C}(\boldsymbol{\varphi}, \boldsymbol{c} \times \boldsymbol{\varphi}) = 0 \, , \tag{II.2.3}$$

for all constant vector fields $\boldsymbol{c} \in \mathbb{R}^{n_{\text{dim}}}$. The relations (II.2.3) correspond to the infinitesimal generators of the action of the Euclidean group $\mathbb{R}^{n_{\text{dim}}} \times SO(n_{\text{dim}})$ associated with the symmetry of the governing equations (II.2.1) under translations and rotations, respectively; see e.g. MARSDEN [1992]. This leads to the existence of special (dynamic) equilibrium solutions given by the group motion

$$\boldsymbol{\varphi}_{et}(\boldsymbol{X}, t) = \text{EXP}\left[t \ \text{SPIN}\left[\boldsymbol{\Omega}_e\right]\right] \boldsymbol{\varphi}_e(\boldsymbol{X}) + \left(\int_O^t \text{EXP}\left[\eta \ \text{SPIN}\left[\boldsymbol{\Omega}_e\right]\right] \, d\eta \right) \boldsymbol{V}_e \, , \tag{II.2.4}$$

in terms of two fixed vectors $\boldsymbol{\Omega}_e$ and $\boldsymbol{V}_e$, the angular and translational velocities , respectively, and the relative equilibrium configuration $\boldsymbol{\varphi}_e(\boldsymbol{X})$ satisfying the equilibrium equation

$$\int_{\mathcal{B}} \rho_o \boldsymbol{\Omega}_e \times [\boldsymbol{\Omega}_e \times \boldsymbol{\varphi}_e + \boldsymbol{V}_e] \cdot \delta\boldsymbol{\varphi} \ dV + \int_{\mathcal{B}} \boldsymbol{S}(\boldsymbol{\varphi}_e) : \boldsymbol{F}_e^T \text{GRAD}\left[\delta\boldsymbol{\varphi}\right] \ dV = 0 \, , \tag{II.2.5}$$

again for all admissible variations $\delta\boldsymbol{\varphi}$; see SIMO ET AL [1991]. The existence of these relative equilibria relies again on the critical property of the strain variations

$$\delta \boldsymbol{C}(\boldsymbol{\varphi}_{et}, \delta\boldsymbol{\varphi}) = \delta \boldsymbol{C}\left(\boldsymbol{\varphi}_e, \text{EXP}\left[- t \ \text{SPIN}\left[\boldsymbol{\Omega}_e\right]\right] \delta\boldsymbol{\varphi}\right) \, , \tag{II.2.6}$$

along the group motion $\boldsymbol{\varphi}_{et}(\boldsymbol{X}, t)$ in (II.2.4). Here, $\text{SPIN}\left[\boldsymbol{\Omega}_e\right]$ denotes the skew tensor with axial vector $\boldsymbol{\Omega}_e$, and $\text{EXP}\left[\text{SPIN}\left[\boldsymbol{\Omega}_e\right]\right]$ the rotation defined by the exponential map between skew and rotation tensors.

Finally, we note that we always have the relation

$$\frac{d}{dt} \underbrace{\left[\int_{\mathcal{B}} \left[\frac{1}{2} \rho_o \| \boldsymbol{V} \|^2 + W \right] \, dV \right]}_{=:H} = - \int_{\mathcal{B}} \mathcal{D} \, dV \qquad \text{for} \qquad \mathcal{D} = \boldsymbol{S} : \frac{1}{2} \dot{\boldsymbol{C}} - \dot{W} \, , \tag{II.2.7}$$

for a general function W. Crucial again for obtaining the stress power in (II.2.7) is the relation

$$\delta \boldsymbol{C}(\boldsymbol{\varphi}, \dot{\boldsymbol{\varphi}}) = \dot{\boldsymbol{C}} \, , \tag{II.2.8}$$

for the strain variations. The interest here is the consideration of material models with W corresponding to the (internal) stored energy (H being the total energy with the kinetic energy) and $\mathcal{D}$ the energy dissipation, a non-negative quantity by the second law of thermodynamics.

In particular, we are interested in the case of finite strain plasticity characterized by the multiplicative decomposition $\boldsymbol{F} = \boldsymbol{F}^e \boldsymbol{F}^p$ of the deformation gradient in an elastic and

plastic part; see ARMERO [2006] and references therein. The stresses are then given in terms of an elastic potential $W^e(\boldsymbol{C}^e)$ for $\boldsymbol{C}^e = \boldsymbol{F}^{e^T}\boldsymbol{F}^e$ as

$$\widetilde{\boldsymbol{S}} = \boldsymbol{F}^p \boldsymbol{S} \boldsymbol{F}^{p^T} = 2\frac{\partial W^e}{\partial \boldsymbol{C}^e} \ , \tag{II.2.9}$$

with the plastic part $\boldsymbol{F}^p$ defined by the plastic evolution equations ($\boldsymbol{L}^p = \dot{\boldsymbol{F}}^p \boldsymbol{F}^{p^{-1}}$)

$$\boldsymbol{D}^p := \text{sym}\,[\boldsymbol{C}^e \boldsymbol{L}^p] = \boldsymbol{F}^{p^{-T}} \dot{\boldsymbol{C}} \boldsymbol{F}^{p^{-1}} - \dot{\boldsymbol{C}}^e = \gamma\ \boldsymbol{N}_\phi(\widetilde{\boldsymbol{S}}, q) \ , \tag{II.2.10}$$

$$\boldsymbol{W}^p := \text{skew}\,[\boldsymbol{C}^e \boldsymbol{L}^p] = \gamma\ \boldsymbol{M}_{W^p}(\widetilde{\boldsymbol{S}}, q) \ , \tag{II.2.11}$$

$$\dot{\alpha} = \gamma\ n_\phi(\widetilde{\boldsymbol{S}}, q) \ , \tag{II.2.12}$$

$$\phi(\widetilde{\boldsymbol{S}}, q) \leq 0 \ , \quad \gamma \geq 0 \ , \quad \gamma\phi = 0 \text{and} \gamma\dot{\phi} = 0 \ , \tag{II.2.13}$$

for the yield surface $\phi(\widetilde{\boldsymbol{S}}, q)$ characterizing the elastic domain in stress space. We have considered isotropic hardening, modeled by the equivalent plastic strain α and the conjugate stress-like variable $q := -\partial\mathcal{H}/\partial\alpha$ for a hardening potential $\mathcal{H}(\alpha)$. In this setting, the internal energy $W = W^e + \mathcal{H}$ with the plastic dissipation given by $\mathcal{D} = \widetilde{\boldsymbol{S}} : \boldsymbol{D}^p + q\dot{\alpha}$. The hyperelastic case is recovered for a fixed $\boldsymbol{F}^p$, which is the case assumed for the relative equilibria (II.2.5) (i.e. vanishing of the plastic evolution or $\gamma = 0$ in (II.2.10)-(II.2.13)).

II.3. EDMC time-stepping algorithms

The numerical solution of the governing equations (II.2.1) proceeds with the consideration of their spatial and temporal discretizations. The spatial discretization of interest here starts with the finite element discretizations of the deformation and velocity fields

$$\boldsymbol{\varphi}(\boldsymbol{X}, t_{n+i}) \approx \boldsymbol{\varphi}^h_{n+i}(\boldsymbol{X}) = \sum_{A=1}^{n_{node}} N^A(\boldsymbol{X})\ \underbrace{\left(\boldsymbol{X}^A + \boldsymbol{d}^A_{n+i}\right)}_{=:\boldsymbol{x}^A_{n+i}} \ , \tag{II.3.1}$$

and

$$\boldsymbol{V}(\boldsymbol{X}, t_{n+i}) \approx \boldsymbol{V}^h_{n+i}(\boldsymbol{X}) = \sum_{A=1}^{n_{node}} N^A(\boldsymbol{X})\ \boldsymbol{v}^A_{n+i} \ , \tag{II.3.2}$$

with $i = 0$, or 1, and for the shape functions $N^A(\boldsymbol{X})$ associated to the n_{node} nodes with nodal (reference) coordinates $\boldsymbol{X}^A$, displacements $\boldsymbol{d}_{n+i}$ and velocities $\boldsymbol{v}_{n+i}$ in a typical time step $[t_n, t_{n+1}]$ with $\Delta t = t_{n+1} - t_n$, not necessarily constant.

Using standard procedures, together with a one-step mid-point interpolation in time ($\boldsymbol{v}_{n+\frac{1}{2}} := (\boldsymbol{v}_n + \boldsymbol{v}_{n+1})/2$), we obtain the discrete algebraic system of equations

$$\frac{1}{\Delta t}\boldsymbol{M}\ (\boldsymbol{v}_{n+1} - \boldsymbol{v}_n) + \int_{\mathcal{B}^h} \overline{\boldsymbol{B}}^T_* \boldsymbol{S}_*\ dV = \boldsymbol{f}_{ext} \quad , \tag{II.3.3}$$

$$\boldsymbol{d}_{n+1} - \boldsymbol{d}_n = \Delta t\ \boldsymbol{v}_{n+\frac{1}{2}} \ , \tag{II.3.4}$$

for a (symmetric) stress approximation $\boldsymbol{S}_*$ to be defined. Here, we have introduced the standard nodal external force $\boldsymbol{f}_{ext}$ and the mass matrix $\boldsymbol{M}$ defined as usual by the assembly of element contributions $\boldsymbol{M} = \mathbf{A}_{e=1}^{n_{elem}} M_e^{AB}\mathbf{1}$ with

$$M_e^{AB} = \int_{\mathcal{B}_e^h} \rho_o N^A N^B \, dV \, , \qquad \text{or} \qquad M^{AB} = \int_{\mathcal{B}_e^h} \rho_o N^A dV \delta_{AB} \text{ (no sum)} \, , \tag{II.3.5}$$

for the consistent or lump forms of the mass. We have also considered an assumed linearized strain operator $\overline{\boldsymbol{B}}_*$ (or, simply, the B-bar operator) defined by the relations

$$\frac{1}{2}\delta \boldsymbol{C} \approx \frac{1}{2}\delta \overline{\boldsymbol{C}} \approx \overline{\boldsymbol{B}}_* \delta \boldsymbol{d} \, , \tag{II.3.6}$$

for the nodal variations $\delta \boldsymbol{d}$. Note the approximate signs in this equation, indicating numerically consistent approximations (in fact, second order approximations of the mid-point values). In particular, the stresses are assumed to be given in terms of the assumed strains $\overline{\boldsymbol{C}} = \overline{\boldsymbol{F}}^T \overline{\boldsymbol{F}}$ for an assumed deformation gradient $\overline{\boldsymbol{F}} \approx \text{GRAD}[\boldsymbol{\varphi}^h]$ as considered in the following section.

The goal is the development of numerical approximations that preserve the conservation/dissipation laws of energy and momenta identified in the previous section for the problem at hand, the so-called EDMC schemes. The conservation laws of linear and angular momenta, defined in this discrete setting

$$\boldsymbol{l}_{n+i}^h = \sum_{A,B=1}^{n_{node}} M^{AB} \, \boldsymbol{v}_{n+i}^B \qquad \text{and} \qquad \boldsymbol{j}_{n+i}^h = \sum_{A,B=1}^{n_{node}} M^{AB} \boldsymbol{x}_{n+i}^A \times \boldsymbol{v}_{n+i}^B \, , \tag{II.3.7}$$

(i.e. $\boldsymbol{l}_{n+1}^h = \boldsymbol{l}_n^h$ and $\boldsymbol{j}_{n+1}^h = \boldsymbol{j}_n^h$ for $\boldsymbol{f}_{ext} = 0$), follow easily from the considered mid-point approximation (II.3.4), as long as the B-bar operator satisfies the relations

$$\boxed{\overline{\boldsymbol{B}}_* \widehat{\boldsymbol{c}} = 0 \qquad \text{and} \qquad \overline{\boldsymbol{B}}_* \Big(\widehat{\boldsymbol{c} \times \boldsymbol{x}_{n+\frac{1}{2}}} \Big) = 0 \, ,} \tag{II.3.8}$$

for a constant vector $\boldsymbol{c} \in \mathbb{R}^{n_{\text{dim}}}$ (here, $\widehat{(\cdot)}$ denotes the global vector of nodal values given by $(\cdot)$). We observe that the conditions (II.3.8) are the discrete counterparts of the relations (II.2.3) for the continuum problem.

The group motion associated to the relative equilibria of the discrete equations (II.3.3)-(II.3.4) were obtained in Armero & Romero [2001a] and are given by

$$\boldsymbol{x}_{en}^A = \boldsymbol{\Lambda}_n \boldsymbol{\varphi}_e^{hA} + \boldsymbol{u}_n \quad \text{and} \quad \boldsymbol{v}_{en}^A = \boldsymbol{\Lambda}_n \left[\boldsymbol{\Omega}_e \times \boldsymbol{\varphi}_e^{hA} + \boldsymbol{V}_e \right] \, , \tag{II.3.9}$$

for fixed vectors $\boldsymbol{\Omega}_e$ and $\boldsymbol{V}_e$, and a sequence of rotations $\{\boldsymbol{\Lambda}_n\}$ and displacements $\{\boldsymbol{u}_n\}$ defined recursively by the relations

$$\boldsymbol{\Lambda}_{n+1} = \boldsymbol{\Lambda}_n \, \text{CAY} \Big[\Delta t \, \text{SPIN} \left[\boldsymbol{\Omega}_e \right] \Big] \qquad \text{and} \qquad \boldsymbol{u}_{n+1} = \boldsymbol{u}_n + \Delta t \, \boldsymbol{\Lambda}_{n+\frac{1}{2}} \, \boldsymbol{V}_e \, , \tag{II.3.10}$$

for $\boldsymbol{\Lambda}_{n+\frac{1}{2}} := (\boldsymbol{\Lambda}_n + \boldsymbol{\Lambda}_{n+1})/2$ (not a rotation in general) and the Cayley transform

$$\text{CAY}\left[\Delta t\ \text{SPIN}\left[\boldsymbol{\Omega}_e\right]\right] := \left[\mathbf{1} + \frac{\Delta t}{2}\text{SPIN}\left[\boldsymbol{\Omega}_e\right]\right]\left[\mathbf{1} - \frac{\Delta t}{2}\text{SPIN}\left[\boldsymbol{\Omega}_e\right]\right]^{-1} \quad \in SO(n_{\text{dim}})\ , \tag{II.3.11}$$

for the discrete relative equilibrium configuration $\boldsymbol{\varphi}_e^h$ given by the equation

$$\boldsymbol{M}\Big(\boldsymbol{\Omega}_e \times \widehat{(\boldsymbol{\Omega}_e \times \boldsymbol{\varphi}_e^h + \boldsymbol{v}_e)}\Big) + \int_{\mathcal{B}^h} \overline{\boldsymbol{B}}_e^T \boldsymbol{S}(\boldsymbol{\varphi}_e^h) dV = 0\ , \tag{II.3.12}$$

as long as the condition

$$\boxed{\overline{\boldsymbol{B}}_{*e} = \overline{\boldsymbol{B}}_e \boldsymbol{\Lambda}_{n+\frac{1}{2}}^T\ ,} \tag{II.3.13}$$

is satisfied along the group motion (II.3.9). We observe that equation (II.3.12) is the discrete counterpart of the equilibrium equation (II.2.5). Thus the algorithm preserves the relative equilibria of the system as long as the B-bar operator satisfies condition (II.3.13), the counterpart of relation (II.2.6).

Finally, the counterpart of the energy conservation/dissipation equation (II.2.7) is obtained as

$$H_{n+1} - H_n = -\int_{\mathcal{B}} \Delta\mathcal{D}\ dV \qquad \text{for} \qquad \Delta\mathcal{D} = \boldsymbol{S} : \frac{1}{2}\Delta\overline{\boldsymbol{C}} - \Delta W\ , \tag{II.3.14}$$

and

$$H_{n+i} = \frac{1}{2}\boldsymbol{v}_{n+i} \cdot \boldsymbol{M}\boldsymbol{v}_{n+i} + \int_{\mathcal{B}_e^h} W_{n+i}\ dV \qquad i = 0 \text{ or } 1\ , \tag{II.3.15}$$

for the discrete system (II.3.3)-(II.3.4), as long as we have the relation

$$\boxed{\overline{\boldsymbol{B}}_*\left(\boldsymbol{d}_{n+1} - \boldsymbol{d}_n\right) = \frac{1}{2}\Delta\overline{\boldsymbol{C}}\ ,} \tag{II.3.16}$$

for the B-bar operator $\overline{\boldsymbol{B}}_*$ and the increment of the assumed strain $\Delta\overline{\boldsymbol{C}}/2$.

Clearly, the interest here lies in the discrete dissipation (II.3.14) reproducing exactly the dissipation of the continuum system. For the elastoplastic model (II.2.10)-(II.2.13), this can be accomplished by considering the elastoplastic decomposition of the assumed deformation gradient $\overline{\boldsymbol{F}} = \boldsymbol{F}^e\boldsymbol{F}^p$ (see Section II.4.1 below) and the discrete equations

$$\frac{1}{2}\left(\left[\boldsymbol{F}^p\right]_{n+\frac{1}{2}}^{-T} \Delta\overline{\boldsymbol{C}} \left[\boldsymbol{F}^p\right]_{n+\frac{1}{2}}^{-1} - \Delta\boldsymbol{C}^e\right) = \Delta\gamma\ \boldsymbol{N}_\phi(\widetilde{\boldsymbol{S}}_*, q_*)\ , \tag{II.3.17}$$

$$\text{skew}\left[\left[\boldsymbol{C}^e\right]_{n+\frac{1}{2}}\left(\boldsymbol{F}_{n+1}^p - \boldsymbol{F}_n^p\right)\left[\boldsymbol{F}^p\right]_{n+\frac{1}{2}}^{-T}\right] = \Delta\gamma\ \boldsymbol{M}_{W^p}(\widetilde{\boldsymbol{S}}_*, q_*)\ , \tag{II.3.18}$$

$$\phi_* := \phi(\widetilde{\boldsymbol{S}}_*, q_*) \le 0\ , \quad \Delta\gamma \ge 0\ , \quad \Delta\gamma\phi_* = 0\ , \tag{II.3.19}$$

as proposed in ARMERO [2006], with $q_* = -\Delta\mathcal{H}/\Delta\alpha$ and the stresses given by $\boldsymbol{S}_* = \boldsymbol{F}^p_{n+\frac{1}{2}} \widetilde{\boldsymbol{S}}_* \boldsymbol{F}^{p^T}_{n+\frac{1}{2}}$ with

$$\boldsymbol{S}_* = 2\frac{\partial W}{\partial \boldsymbol{C}^e}\left([\boldsymbol{C}^e]_{n+\frac{1}{2}}\right) + 2\frac{W(\boldsymbol{C}^e_{n+1}) - W(\boldsymbol{C}_n) - 2\frac{\partial W}{\partial \overline{\boldsymbol{C}}^e}\left([\boldsymbol{C}^e]_{n+\frac{1}{2}}\right) : \Delta\boldsymbol{C}^e}{[\boldsymbol{C}^e]^{-1}_{n+\frac{1}{2}}\, \Delta\boldsymbol{C}^e : \Delta\overline{\boldsymbol{C}}^e\, [\boldsymbol{C}^e]^{-1}_{n+\frac{1}{2}}} [\boldsymbol{C}^e]^{-1}_{n+\frac{1}{2}}\, \Delta\boldsymbol{C}^e\, [\boldsymbol{C}^e]^{-1}_{n+\frac{1}{2}} \quad \text{(II.3.20)}$$

Here we have introduced the notation $[(\cdot)]_{n+\frac{1}{2}} = ((\cdot)_n + (\cdot)_{n+1})/2$. The formula (II.3.20) corresponds to a conserving approximation of the gradient formula (II.2.9) such that $\widetilde{\boldsymbol{S}} : \frac{1}{2}\Delta\boldsymbol{C}^e = \Delta W^e$. It is a modification of the the original conserving formula proposed in GONZÁLEZ [2000] by including the elastic metric $[\boldsymbol{C}^e]^{-1}_{n+\frac{1}{2}}$, as it will become crucial in the construction of the assumed B-bar operator in the following section. Again, the exact plastic dissipation (including exact energy conservation for an elastic step) is obtained by the return mapping algorithm (II.3.17)-(II.3.19) and the stress formula (II.3.20). This situation adds the desired numerical stability to the algorithms as illustrated with the numerical simulation presented in Section II.5.

A variation of the return mapping algorithm (II.3.17)-(II.3.19) that also imposes exactly the isochoric plastic response in isochoric plastic models, like the classical J_2-flow theory of metals, can be found in ARMERO & ZAMBRANA [2007]. Similarly, we refer to ARMERO & ROMERO [2001a], ARMERO & ROMERO [2001b] for variations of the stress formula (II.3.20) that incorporate a controllable high-frequency numerical energy dissipation to handle the usual high numerical stiffness in the systems of interest.

II.4. Conserving assumed strain finite element methods

II.4.1. The assumed deformation gradient and its variations

The interest here is the development of assumed strain finite element methods for the locking-free approximation of nearly incompressible material models, like the plasticity models outlined above combined with a Mises-type deviatoric yield surface, while exhibiting the conservation/dissipation laws obtained in the previous section. This can be accomplished with the now standard scaled deformation gradient (see e.g. ARMERO [2000], SIMO ET AL [1988])

$$\overline{\boldsymbol{F}}_{n+i} = \left(\frac{\Theta_{n+i}}{J_{n+i}}\right)^{\frac{1}{3}} \text{GRAD}\left[\boldsymbol{\varphi}^h_{n+i}\right] \qquad \text{for} \qquad J_{n+i} := \det\left[\text{GRAD}\left[\boldsymbol{\varphi}^h_{n+i}\right]\right], \quad \text{(II.4.1)}$$

(for $i = 0$, or 1) and the assumed Jacobian $\Theta = \det[\overline{\boldsymbol{F}}]$ defined by the weighted average at the element level

$$\Theta_{n+i}(\boldsymbol{X}) := \boldsymbol{\Gamma}^T(\boldsymbol{X})\, \boldsymbol{H}^{-1} \int_{\mathcal{B}^h_e} \boldsymbol{\Gamma}(\boldsymbol{Y}) J_{n+i}(\boldsymbol{Y})\, dV\,, \quad \text{(II.4.2)}$$

for a set of n_θ element interpolation functions $\boldsymbol{\Gamma}(\boldsymbol{X})$ and the corresponding matrix

$$\boldsymbol{H} := \int_{\mathcal{B}_e^h} \boldsymbol{\Gamma}(\boldsymbol{Y})\ \boldsymbol{\Gamma}^{\,T}(\boldsymbol{Y})\ dV \in \mathbb{R}^{n_\theta \times n_\theta}\ , \tag{II.4.3}$$

over a generic element $\mathcal{B}_e^h$. Typical choices are $n_\theta = 1$ and $\boldsymbol{\Gamma} = 1$ in combination with a bilinear quadrilateral or trilinear brick element (Q1/A0), and $n_\theta = 3$ with $\boldsymbol{\Gamma} = [1\ \xi\ \eta]^T$ for the isoparametric coordinates (ξ, η) in plane problems (and similarly for 3D) in combination with quadratic quadrilateral or triangular elements (Q2/A1 or P2/A1).

The consideration of the assumed right Cauchy-Green tensor $\overline{\boldsymbol{C}}_{n+i} = \overline{\boldsymbol{F}}^T_{n+i}\overline{\boldsymbol{F}}_{n+i}$ leads to the variations $\delta\overline{\boldsymbol{C}}_{n+i}/2 = \overline{\boldsymbol{B}}_{n+i}\delta\boldsymbol{d}_{n+i}$ for

$$\overline{\boldsymbol{B}}^A_{n+i} = \left(\frac{\Theta_{n+i}}{J_{n+i}}\right)^{\frac{2}{3}} \left[\boldsymbol{B}^A_{n+i} + \frac{1}{3}\ \boldsymbol{C}(\boldsymbol{\varphi}^h_{n+i}) \otimes \left(\overline{\boldsymbol{g}}^A_{n+i} - \boldsymbol{g}^A_{n+i}\right)\right]\ , \tag{II.4.4}$$

defining the classical B-bar operator $\overline{\boldsymbol{B}}_{n+i}$ in terms of the standard (displacement) linearized strain operator

$$\boldsymbol{B}^A_{n+i} := \begin{bmatrix} \left(\boldsymbol{\varphi}^h_{n+i}\right)^T_{,1}\ N^A_{,1} \\ \left(\boldsymbol{\varphi}^h_{n+i}\right)^T_{,2}\ N^A_{,2} \\ \left(\boldsymbol{\varphi}^h_{n+i}\right)^T_{,1}\ N^A_{,2} + \left(\boldsymbol{\varphi}^h_{n+i}\right)^T_{,2}\ N^A_{,1} \end{bmatrix} \qquad \text{for} \quad A = 1, n_{node}\ , \tag{II.4.5}$$

for plane problems (similarly for 3D), and the spatial gradients

$$\boldsymbol{g}^A_{n+i} := \boldsymbol{F}^{-T}_{n+i}\boldsymbol{G}^A \qquad \text{and} \qquad \overline{\boldsymbol{g}}^A_{n+i} := \boldsymbol{\Gamma}^{\,T}\ \boldsymbol{H}^{-1} \int_{\mathcal{B}_e^h} \boldsymbol{\Gamma}\ \boldsymbol{g}^A_{n+i}\ dV\ , \tag{II.4.6}$$

for the material gradients $\boldsymbol{G}^A := \text{GRAD}[N^A] = \left[N^A_{,1}\ N^A_{,2}\right]^T$ $(A = 1, n_{node})$ as used in (II.4.5). Here we consider $i = 0$, $1/2$ or 1, with $i = 1/2$ corresponding to the evaluation of the different quantities above in the mid-point configuration $\boldsymbol{\varphi}^h_{n+\frac{1}{2}} = (\boldsymbol{\varphi}^h_n + \boldsymbol{\varphi}^h_{n+1})/2$.

The standard choice $\overline{\boldsymbol{B}}_{n+\frac{1}{2}}$ in the governing equation (II.3.3) does not lead, however, to a conserving approximation. The conditions (II.3.8) can be easily seen to be satisfied, but the conditions (II.3.13) and (II.3.16) for the conservation of the relative equilibria and energy are not. This situation is to be traced to the spatial gradients $\boldsymbol{g}^A_{n+\frac{1}{2}}$ in (II.4.6). First, we observe that during the group motion (II.3.9) we have $\boldsymbol{F}_n = \boldsymbol{\Lambda}_n\boldsymbol{F}_e$ and $\boldsymbol{F}_{n+1} = \boldsymbol{\Lambda}_{n+1}\boldsymbol{F}_e$ for the equilibrium deformation gradient $\boldsymbol{F}_e$, but

$$\boldsymbol{g}^A_{n+\frac{1}{2}} = \boldsymbol{\Lambda}^{-T}_{n+\frac{1}{2}} \underbrace{\boldsymbol{F}_e^{-T}\boldsymbol{G}^A}_{=:\boldsymbol{g}^A_e} = \boldsymbol{\Lambda}^{-T}_{n+\frac{1}{2}}\boldsymbol{g}^A_e \neq \boldsymbol{\Lambda}_{n+\frac{1}{2}}\ \boldsymbol{g}^A_e\ , \tag{II.4.7}$$

as required for (II.3.13), since $\boldsymbol{\Lambda}_{n+\frac{1}{2}} = (\boldsymbol{\Lambda}_n + \boldsymbol{\Lambda}_{n+1})/2$ is not a rotation in general. Similarly, the condition (II.3.16) is not satisfied, in part because

$$\sum_{A=1}^{n_{node}} \boldsymbol{g}^A_{n+\frac{1}{2}} \cdot \left(\boldsymbol{d}^A_{n+1} - \boldsymbol{d}^A_n\right) \neq \frac{(J_{n+1} - J_n)}{[J]_{n+\frac{1}{2}}} \,, \tag{II.4.8}$$

for $[J]_{n+\frac{1}{2}} = (J_n + J_{n+1})/2$, as it would be expected from its continuum counterpart ($\dot{J} = J\ \nabla \boldsymbol{v} : \mathbf{1}$ for the spatial velocity gradient $\nabla \boldsymbol{v}$).

II.4.2. A new conserving B-bar operator

Faced with the difficulties observed in the previous section, we introduce the new modified spatial gradients

$$\boxed{\widehat{\boldsymbol{g}}^A_{n+\frac{1}{2}} := \boldsymbol{F}_{n+\frac{1}{2}}\, [\boldsymbol{C}]^{-1}_{n+\frac{1}{2}}\, \boldsymbol{G}^A + 2\frac{\frac{J_{n+1}-J_n}{[J]_{n+\frac{1}{2}}} - \frac{1}{2}\,[\boldsymbol{C}]^{-1}_{n+\frac{1}{2}} : \Delta \boldsymbol{C}}{[\boldsymbol{C}]^{-1}_{n+\frac{1}{2}}\, \Delta \boldsymbol{C} : \Delta \boldsymbol{C}\, [\boldsymbol{C}]^{-1}_{n+\frac{1}{2}}}\, \boldsymbol{F}_{n+\frac{1}{2}}\, [\boldsymbol{C}]^{-1}_{n+\frac{1}{2}}\, \Delta \boldsymbol{C}\, [\boldsymbol{C}]^{-1}_{n+\frac{1}{2}}\, \boldsymbol{G}^A \,,} \tag{II.4.9}$$

for $A = 1, n_{node}$, and their assumed counterparts

$$\overline{\widehat{\boldsymbol{g}}}^A_{n+\frac{1}{2}} = \frac{1}{[\Theta]_{n+\frac{1}{2}}} \boldsymbol{\Gamma}^T \boldsymbol{H}^{-1} \int_{\mathcal{B}^h_e} \boldsymbol{\Gamma}\, [J]_{n+\frac{1}{2}}\, \widehat{\boldsymbol{g}}^A_{n+\frac{1}{2}}\, dV \,, \tag{II.4.10}$$

where we note the use of the average Jacobian $[J]_{n+\frac{1}{2}} = (J_n + J_{n+1})/2$. We observe that these modified spatial gradients do satisfy, by construction, the relations

$$\sum_{A=1}^{n_{node}} \widehat{\boldsymbol{g}}^A_{n+\frac{1}{2}} \cdot \left(\boldsymbol{d}^A_{n+1} - \boldsymbol{d}^A_n\right) = \frac{J_{n+1} - J_n}{[J]_{n+\frac{1}{2}}} \quad \text{and} \quad \sum_{A=1}^{n_{node}} \overline{\widehat{\boldsymbol{g}}}^A_{n+\frac{1}{2}} \cdot \left(\boldsymbol{d}^A_{n+1} - \boldsymbol{d}^A_n\right) = \frac{\Theta_{n+1} - \Theta_n}{[\Theta]_{n+\frac{1}{2}}} \,, \tag{II.4.11}$$

and

$$\widehat{\boldsymbol{g}}^A_{n+\frac{1}{2}} = \boldsymbol{\Lambda}_{n+\frac{1}{2}} \boldsymbol{g}^A_e \quad \text{and} \quad \overline{\widehat{\boldsymbol{g}}}^A_{n+\frac{1}{2}} = \boldsymbol{\Lambda}_{n+\frac{1}{2}} \overline{\boldsymbol{g}}^A_e \,, \tag{II.4.12}$$

along the group motion (II.3.9), all for $A = 1, n_{node}$. We can observe the similarities with the stress formula (II.3.20) and, in particular, the use of the reference (convected) metric $[\boldsymbol{C}]_{n+\frac{1}{2}}$ to arrive at the proper transformation properties for the modified spatial gradients.

With these definitions at hand, we introduce the following new B-bar operator

$$\boxed{\begin{aligned}\overline{\boldsymbol{B}}^A_* = \left[\Theta^{\frac{2}{3}}\right]_{n+\frac{1}{2}} \left[J^{-\frac{2}{3}}\right]_{n+\frac{1}{2}} \boldsymbol{B}^A_{n+\frac{1}{2}} + \tfrac{1}{2} \left[\Theta^{\frac{2}{3}}\right]_{n+\frac{1}{2}} D_J^{(-\frac{2}{3})}\, [\boldsymbol{C}]_{n+\frac{1}{2}} \otimes \widehat{\boldsymbol{g}}^A_{n+\frac{1}{2}} \\ + \tfrac{1}{2} D_\theta^{(\frac{2}{3})} \left[J^{-\frac{2}{3}} \boldsymbol{C}\right]_{n+\frac{1}{2}} \otimes \overline{\widehat{\boldsymbol{g}}}^A_{n+\frac{1}{2}} \,,\end{aligned}} \tag{II.4.13}$$

for $A = 1, n_{node}$ where

$$D^{(a)}_{(\cdot)} := \begin{cases} [(\cdot)]_{n+\frac{1}{2}} \ \frac{\big((\cdot)_{n+1}\big)^a - \big((\cdot)_n\big)^a}{(\cdot)_{n+1} - (\cdot)_n} & \text{for} \quad (\cdot)_{n+1} \neq (\cdot)_n \ , \\ a \ \Big([(\cdot)]_{n+\frac{1}{2}}\Big)^a & \text{for} \quad (\cdot)_{n+1} = (\cdot)_n \ , \end{cases} \tag{II.4.14}$$

for a generic quantity $(\cdot)$ and exponent a. By the way, we note that the formulas (II.3.20) and (II.4.9) are well-defined, with the quotients vanishing when $\boldsymbol{C}^e_{n+1} = \boldsymbol{C}^e_n$ and $\boldsymbol{C}_{n+1} = \boldsymbol{C}_n$, respectively. No singularity occurs.

The different terms in the expression (II.4.13) can be seen to be second-order approximation of the variations of the assumed $\overline{\boldsymbol{C}}$. Some long algebraic manipulations show that this new B-bar operator satisfies the desired conditions (II.3.8), (II.3.13) and (II.3.16). In particular, the relation (II.3.13) for the relative equilibria is satisfied for the assumed B-bar operator

$$\overline{\boldsymbol{B}}^A_e = \left(\frac{\Theta_e}{J_e}\right)^{\frac{2}{3}} \left[\boldsymbol{B}^A_e + \frac{1}{3}\boldsymbol{C}_e \otimes \big(\overline{\boldsymbol{g}}^A_e - \boldsymbol{g}^A_e\big)\right] \qquad \text{for} \quad A = 1, n_{node} \ , \tag{II.4.15}$$

at the equilibrium configuration $\boldsymbol{\varphi}^h_e$. Hence, the new B-bar operator (II.4.13) leads to a fully energy-momentum assumed strain finite element formulation when combined with the EDMC time-stepping algorithms considered in Section II.3, obtaining in this way a (energy) stable formulation that avoids volumetric locking.

II.5. Representative numerical simulations

We present in this section several numerical simulations to illustrate and evaluate the performance of the assumed finite elements developed in this paper. In particular, we present in Section II.5.1 convergence tests showing the locking-free response of the proposed elements in the incompressible limit. Section II.5.2 evaluates the energy and momentum conservation properties in time for a plane elastic solid in free-flight, including the conservation of the relative equilibria. Finally, Section II.5.3 evaluates the energy dissipation and momentum conservation properties in time for an elastoplastic solid in the general three-dimensional case.

II.5.1. Cook's membrane problem: evaluation of the locking-free properties

We consider in this section the classical benchmark problem of the so-called Cook's membrane for the evaluation of the locking properties of finite elements in the incompressible limit. Figure II.5.1 depicts a sketch of the problem, consisting of a tapered slab fixed

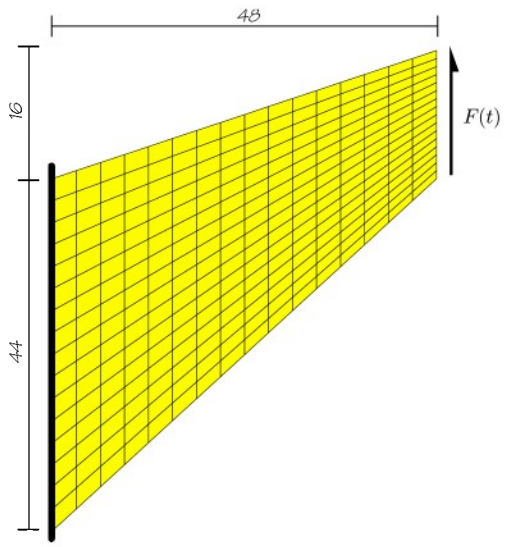

FIGURE II.5.1 Cook's membrane problem. Problem definition: geometry, boundary conditions and loading. Distances in mm. Plane strain conditions are assumed for a unit thickness in the perpendicular direction.

TABLE II.5.1 Cook's membrane. Material parameters.

Young modulus	E	210 GPa
Poisson ratio	ν	0.2–0.4999
Reference density	ρ_o	$1.0{\cdot}10^3$ kg/m^3

at one end and with an imposed transversal load $F(t)$ at the opposite end. The load is applied proportionally in time

$$F(t) = \bar{F}\ \frac{t}{\bar{t}_f}\ , \tag{II.5.1}$$

accounting for the dynamic effects as it is the interest in this work. It is a dead load, uniformly distributed along the reference configuration of the slab's right edge. The solid is assumed to be at rest in the undeformed configuration at $t = 0$. Plane strain conditions are assumed.

We consider the compressible Neo-Hookean hyperelastic model, defined by the potential

$$W(\boldsymbol{C}) = \frac{\Lambda}{2}\ (\ln J)^2 + \frac{\mu}{2}\ (\mathbf{trace}\,[\boldsymbol{C}] - 3) - \mu\ \ln J\ , \tag{II.5.2}$$

for the Lamé constants $2\mu = E/(1+\nu)$ and $\Lambda = 2\mu\nu/(1-2\nu)$ in terms of reference the Young modulus E and Poisson ratio ν. Table II.5.1 includes the values of these parameters assumed in the simulations presented here, including also the reference density ρ_o. To evaluate the performance of the elements in the incompressible limit, the values

of the Poisson ratio $\nu = 0.2$ and 0.4999 are considered, the latter leading effectively to a quasi-incompressible response.

We consider the three characteristic plane elements: the two quadrilateral elements Q1/A0 and Q2/A1 consisting of bi-linear and bi-quadratic displacement interpolations with piece-wise constant and linear interpolations for the volumetric strain interpolation, respectively. To illustrate the development of a triangular element, we consider the P2+/A1 element with 7-node quadratic displacements and a piece-wise linear interpolation for the volume. The simulations presented here for the quadratic elements Q2/A1 and P2+/A1 do consider the presence of an internal node and its contribution to the displacement, velocity and acceleration interpolations (and hence, with mass contributions). Other implementations where these contributions are treated in the context of enhanced strain elements as internal bubbles affecting only the strains can be easily devised. We consider a consistent mass matrix in all cases. The Q1/A0 and Q2/A1 quads consider a 2×2 and 3×3 (full) Gauss quadrature, respectively, whereas the quadratic P2+/A1 element considers the standard 6 point quadrature on triangles; see e.g. HUGHES [1987].

The interest in this section is the evaluation of the locking properties of the spatial interpolations defined by the assumed strain elements developed here. To this end, we consider simulations for different levels of spatial mesh refinement, all with a fixed time step. We run the problem with 100 equal time steps to the final time $t_f = 10\ ms$ and final load $\bar{F} = 100\ kN$, and measure the top corner vertical displacement. We consider regular structured spatial meshes with equal number of nodes per side. Figure II.5.2 depicts the solutions obtained with the three different elements and the mesh with 17 nodes per side for quasi-incompressible case $\nu = 0.4999$. We have included the distribution of the Mises (Cauchy) stress (i.e. $\|\text{dev}[\boldsymbol{\sigma}_{n+1}]\|$ for the Cauchy stress $\boldsymbol{\sigma}_{n+1} := \overline{\boldsymbol{F}}_{n+1}\boldsymbol{S}_*\overline{\boldsymbol{F}}^T_{n+1}/\Theta_{n+1}$ where, recall, $\Theta_{n+1} = \det\left[\overline{\boldsymbol{F}}_{n+1}\right]$) superposed to the deformed spatial configuration. A good agreement can be observed between the different solutions. We note the presence of large displacements and strains. The energy-momentum conserving formula (II.3.20) is considered for the evaluation of the stresses in the time-stepping scheme assumed for the temporal integration of the equation, thus leading to a fully conserving approximation in time. We evaluate these properties in the following sections.

Figure II.5.3 depicts the computed top corner displacement versus the number of nodes per side for the two Poisson's ratios of $\nu = 0.2$ and $\nu = 0.4999$. A fairly good performance is observed for the former case by all the elements. This performance deteriorates drastically in the quasi-incompressible case $\nu = 0.4999$ for the basic displacement finite elements Q1, Q2 and P2+. These elements simply consist of the evaluation of the linearized strain operator $\boldsymbol{B}_{n+\frac{1}{2}}$ in (II.4.5) at the mid-point configuration $t_{n+\frac{1}{2}}$. This choice leads also to the sought energy-momentum conservation properties in time but clearly to volumetric locking in the incompressible limit. As expected the performance of the simple bilinear displacement Q1 quad is particularly bad. The Q2/A1 and P2+/A1 also show a significant improvement over their displacement counterparts Q2 and P2+ elements, as a faster

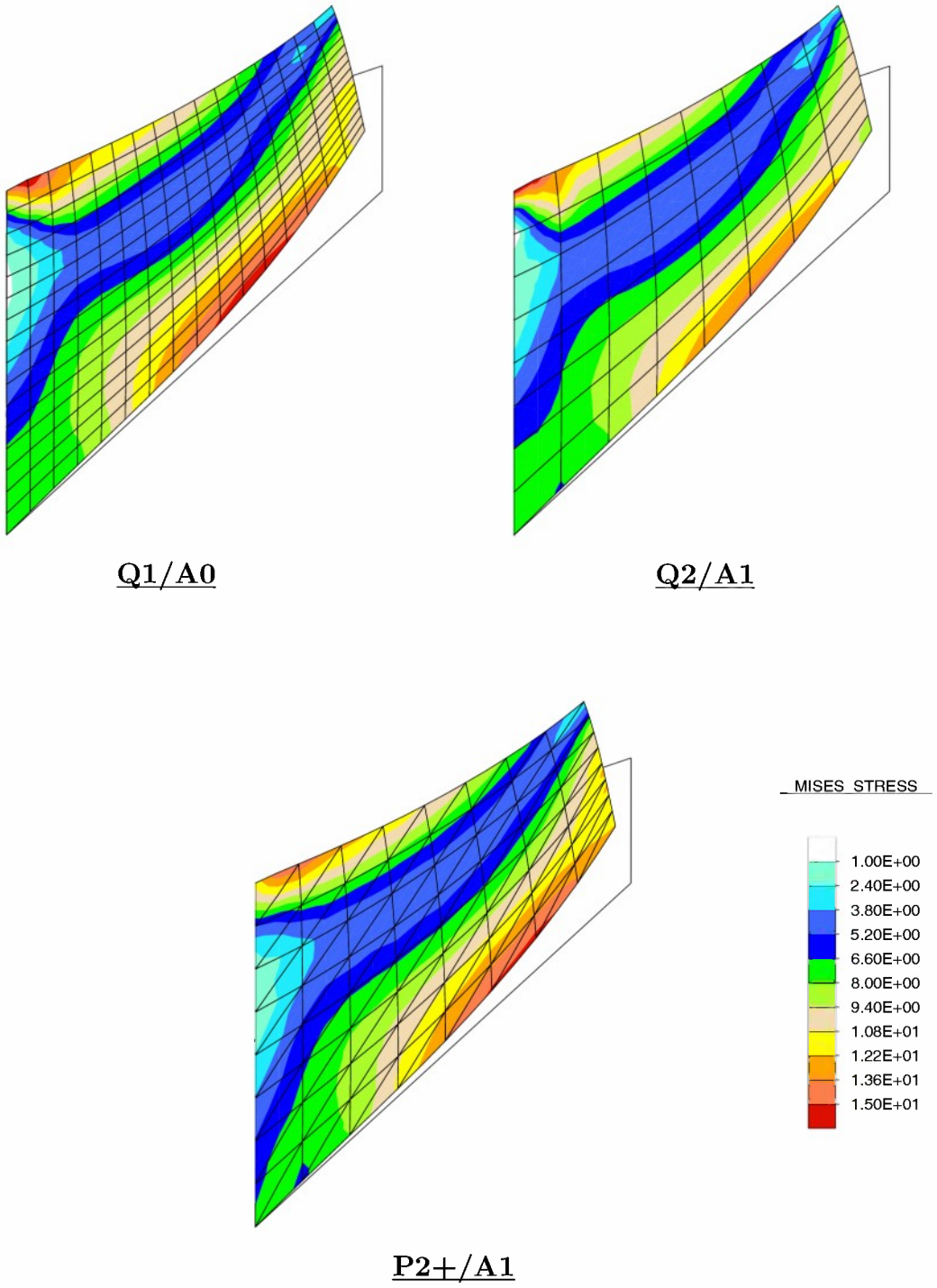

FIGURE II.5.2 Cook's membrane problem. Distribution of the Mises stress (in GPa) superimposed to the deformed configurations at the final time $t = 10s$ for the quasi-incompressible case ($\nu = 0.4999$) and for three different assumed strain elements: the bilinear Q1/A0 and quadratic Q2/A1 quads and the quadratic assumed P2+/A1 triangle. All correspond to the meshes with 17 nodes per side and follow the same scale shown.

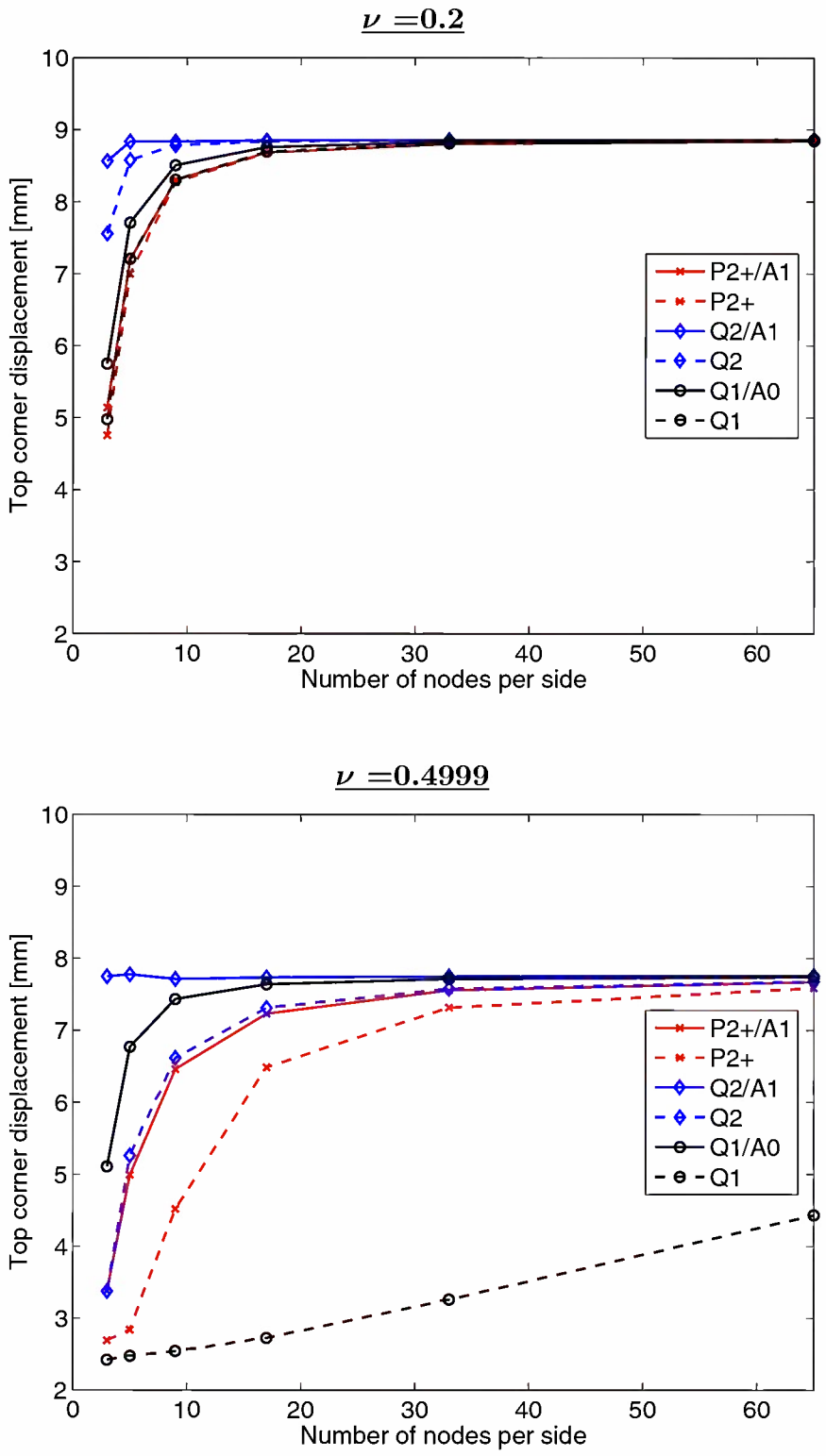

FIGURE II.5.3 Cook's membrane problem. Convergence plots for two different Poisson's ratios ($\nu = 0.2$ and $\nu = 0.4999$) and six different finite elements. The removal of the locking in the quasi-incompressible case $\nu = 0.4999$, to be contrasted with the corresponding basic displacement element, is to be noted.

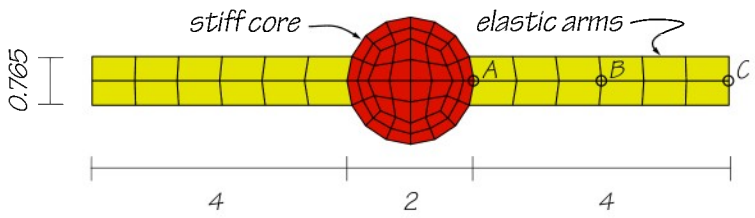

FIGURE II.5.4 Two-dimensional elastic solid in free flight. Problem definition: geometry and initial conditions. Distances in m. Plane strain conditions are assumed for a unit thickness in the perpendicular direction.

TABLE II.5.2 Two-dimensional elastic solid in free-flight. Material parameters for the elastic arms.

Young modulus	E	40	GPa
Poisson ratio	ν	0.45	
Reference density	ρ_o	$8.6{\cdot}10^3$	kg/m^3

convergence is observed for limit values obtained with finer meshes. When comparing the plots presented in Figure II.5.3, we conclude that the proposed assumed treatment of the volumetric strain leads to the desired locking-free response in volume.

II.5.2. Two-dimensional solid in free flight: evaluation of the conservation properties in time for the elastic case, including the relative equilibria

We evaluate in this section the conservation properties in time of the newly developed B-bar formulation for nonlinear elastic problems. We still consider plane strain conditions, leaving the consideration of three-dimensional problems for the next section. The interest here is the confirmation of the conservation of the energy and the preservation of the momentum conservation laws, and the associated relative equilibria, as shown in Proposition I.3.1.

To this purpose, we consider the plane solid depicted in Figure II.5.4 consisting of a rigid cylindrical core and two elastic arms. This figure also shows the finite element mesh considered in all the numerical simulations presented here. It consists of 72 quadrilateral assumed strain Q1/A0 elements, defined by bilinear displacements and the piece-wise constant volumetric strain. The consistent mass matrix (II.3.5) is considered.

The elastic arms follow the compressible Neo-Hookean response defined by the stored energy function (II.5.2). Table II.5.2 includes the values of the material parameters assumed in the simulations. In particular, we consider a Poisson ratio of $\nu = 0.45$ for the problem to be close to the incompressible limit, as evaluated in the previous section. The rigid core has been modeled by simply increasing the Young modulus to 100 times that of

the arms.

The solid is given the initial velocity defined by the nodal values

$$\boldsymbol{v}^A(0) = \Omega\ \boldsymbol{e}_3 \times \boldsymbol{x}^A(0) \qquad A = 1, n_{node}\ , \tag{II.5.3}$$

for an initial angular velocity Ω, the unit vector $\boldsymbol{e}_3$ corresponding to the thickness direction (i.e. the direction perpendicular to the plane of the problem) and the initial nodal positions $\boldsymbol{x}^A(0) = \boldsymbol{X}^A$ of the reference mesh in Figure II.5.4 in a Cartesian reference system with origin at the center of the rigid core. The solid is left then to evolve freely in the plane $\{\boldsymbol{e}_1, \boldsymbol{e}_2\}$, with $\boldsymbol{e}_1$ defined by the axis of the arms in their initial configuration. Figure II.5.5 shows the motion computed with the newly proposed B-bar method (II.4.13) for an initial angular velocity of $\Omega = 0.230\ rad/ms$ and a constant time step of $\Delta t = 0.5\ ms$. We observe that the rigid-body velocity distribution (II.5.3) is lost as the solid deforms from this initial velocity and undeformed configuration. We have included the distribution of the Mises Cauchy stress in the arms, defined as indicated in the previous section, over the deformed configuration of the solid. Large strains and displacements (rotations) around the center (by symmetry) can be observed.

Given the assumed free-flight conditions, the linear momentum $\boldsymbol{l}^h$ and the angular momentum $\boldsymbol{j}^h$ should be conserved along the motion. In particular, $\boldsymbol{j}^h = j^h\ \boldsymbol{e}_3$ for a scalar j^h in this plane setting and $\boldsymbol{l}^h = 0$ for the assumed initial conditions. Similarly, the total energy H^h in (II.3.14) should also be conserved for the assumed elastic response. These conservation properties are confirmed for the new B-bar method (II.4.13) as shown in Figure II.5.6, depicting the exact conservation of the angular momentum j^h and energy H^h along the motion. The different components of the linear momentum, not shown, are also exactly conserved. The kinetic and potential energies, see equation (II.2.7), are also included in the energy plot with their sum, the total energy, showing again its exact conservation. These results confirm Proposition I.3.1.

To illustrate the need of the new B-bar operator for the exact conservation of the energy (that is, to satisfy the relation exactly) we consider the standard (non-conserving) B-bar operator (II.4.4) evaluated at the mid-point $\overline{\boldsymbol{B}}_{n+\frac{1}{2}}$. As discussed above, this choice does conserve the linear and angular momenta but not the energy. This situation is confirmed by the numerical simulations. Figure II.5.7 shows the evolution of the total energy for this case and compares it with the new conserving B-bar method (II.4.13), for two different time steps ($\Delta t = 0.5$ and $0.3\ ms$). The conserving stress formula (II.3.20) is maintained, so the only difference is the B-bar operator. The lack of the conservation of the energy for the standard B-bar operator (II.4.4) is apparent, even though again a conserving stress formula is used.

It is interesting to note that the solutions in Figure II.5.7 begin to show high-frequency content in the long term, leading to a non-convergence of the simulation for the non-conserving B-bar operator at a higher energy content. It must be noted that these failures

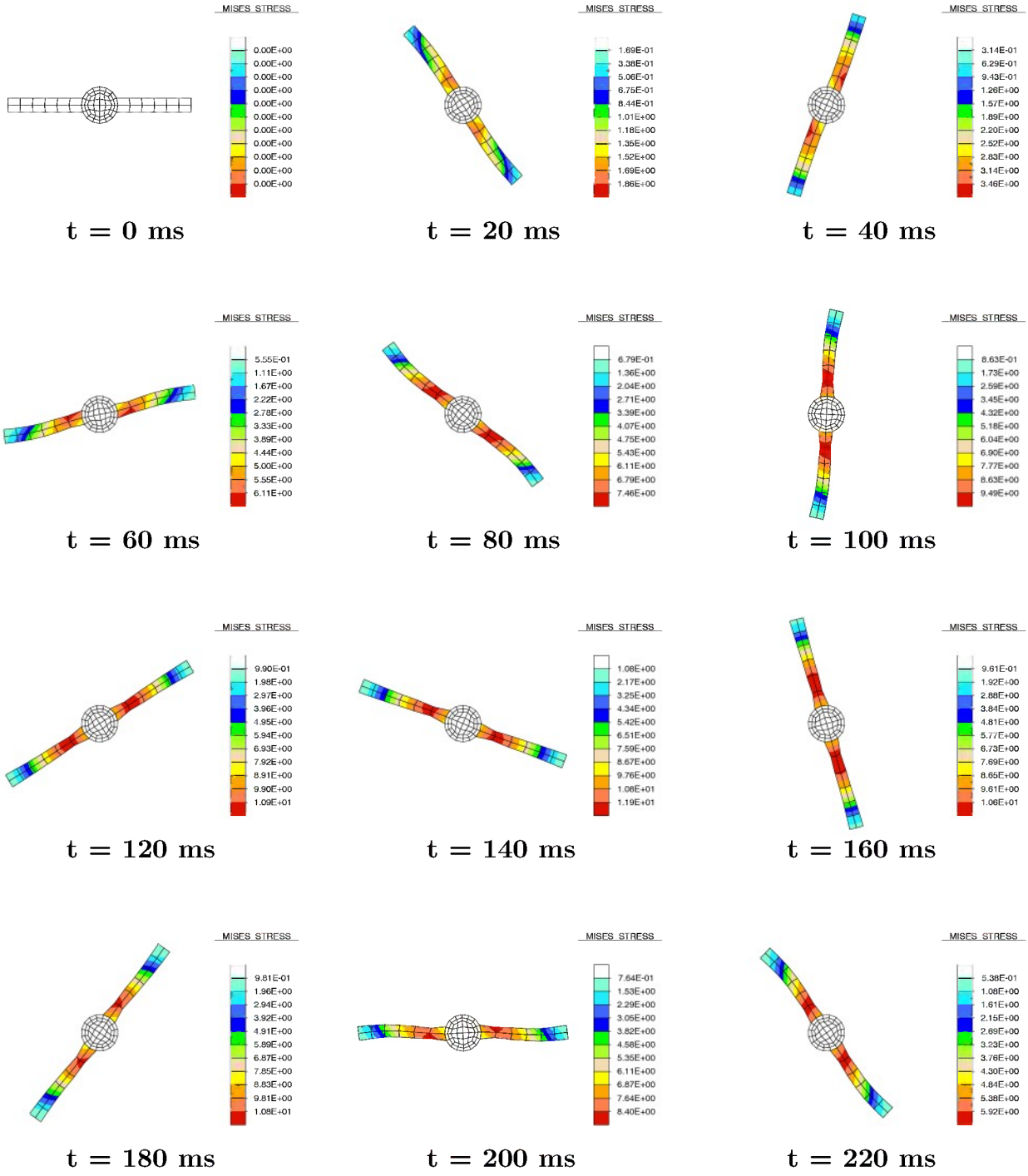

FIGURE II.5.5 Two-dimensional elastic solid in free flight: solution for an angular velocity $\Omega = 0.230\ rad/ms$ ($\Delta t = 0.5\ ms$). The distribution of the Mises stress (in GPa) in the arms is shown superimposed to the solid's deformed configuration at different times.

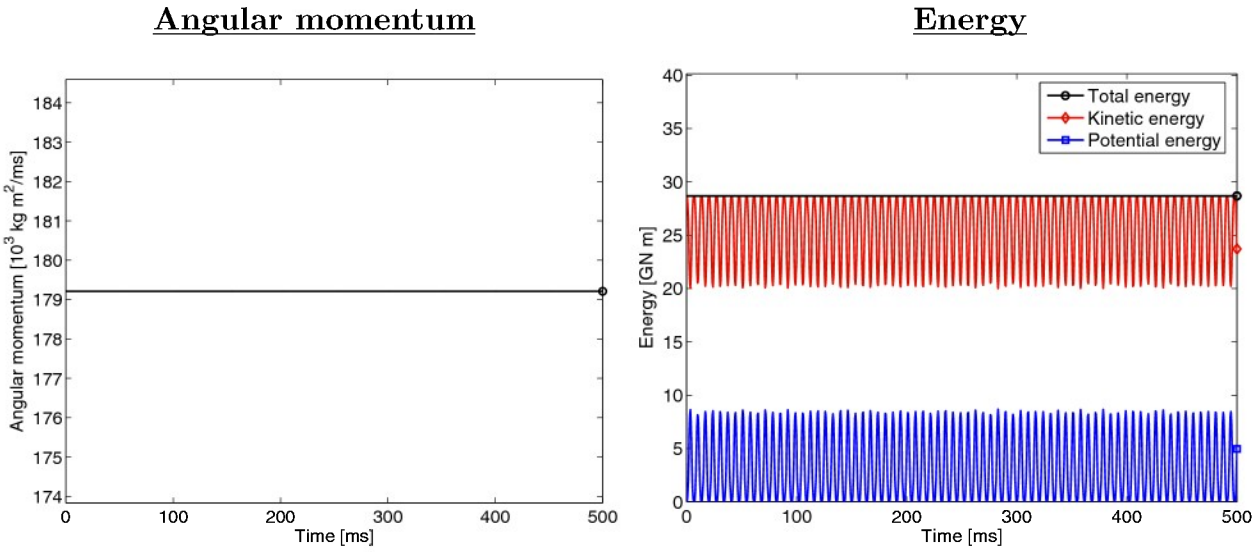

FIGURE II.5.6 Two-dimensional elastic solid in free flight: solution for an angular velocity $\Omega = 0.230\ rad/ms$ ($\Delta t = 0.5\ ms$). Evolution in time of the angular momentum (left) and the energy, including the kinetic, potential and total energies (right), computed with the new conserving assumed strain finite element in combination with an energy-momentum conserving time-stepping scheme. The exact conservation of the total energy and the angular momentum is to be noted.

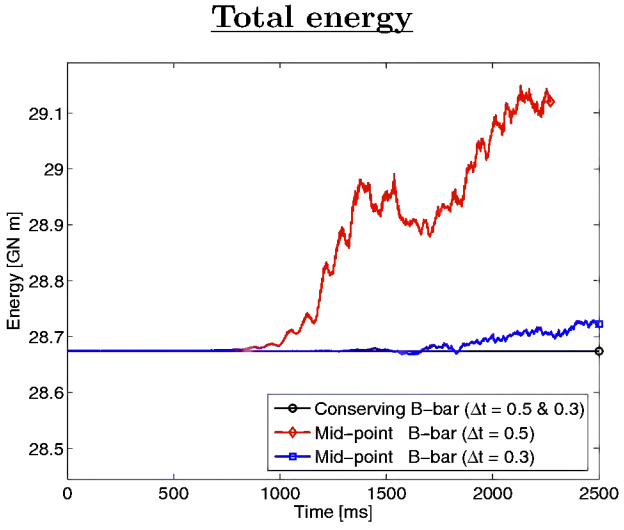

FIGURE II.5.7 Two-dimensional elastic solid in free flight. Solution for an angular velocity $\Omega = 0.230\ rad/ms$. Evolution in time of the total energy computed with the new conserving B-bar operator (II.4.13) and the basic mid-point B-bar operator (II.4.4), for different time steps.

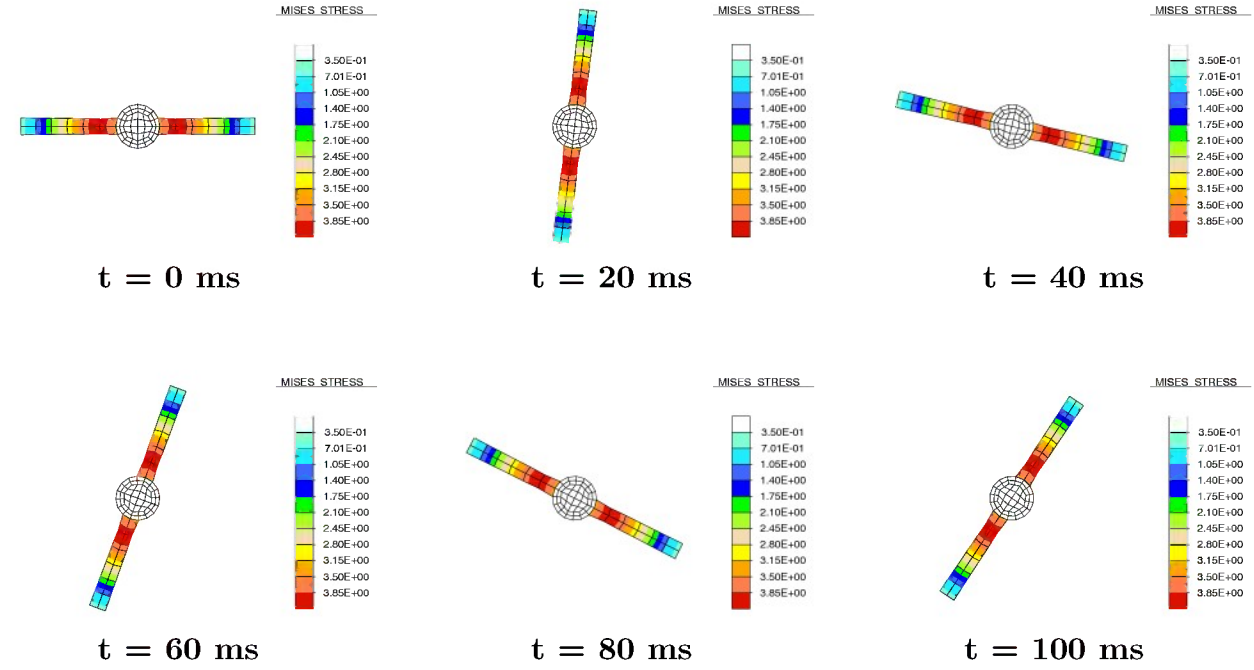

FIGURE II.5.8 Two-dimensional elastic solid in free flight: group motion associated with the relative equilibrium at an angular velocity $\Omega = 0.230\ rad/ms$ ($\Delta t = 0.5\ \ ms$). The distribution of the Mises stress (in GPa) in the arms is shown superimposed to the solid's deformed configuration at different times. An exact rotation can be observed for all times.

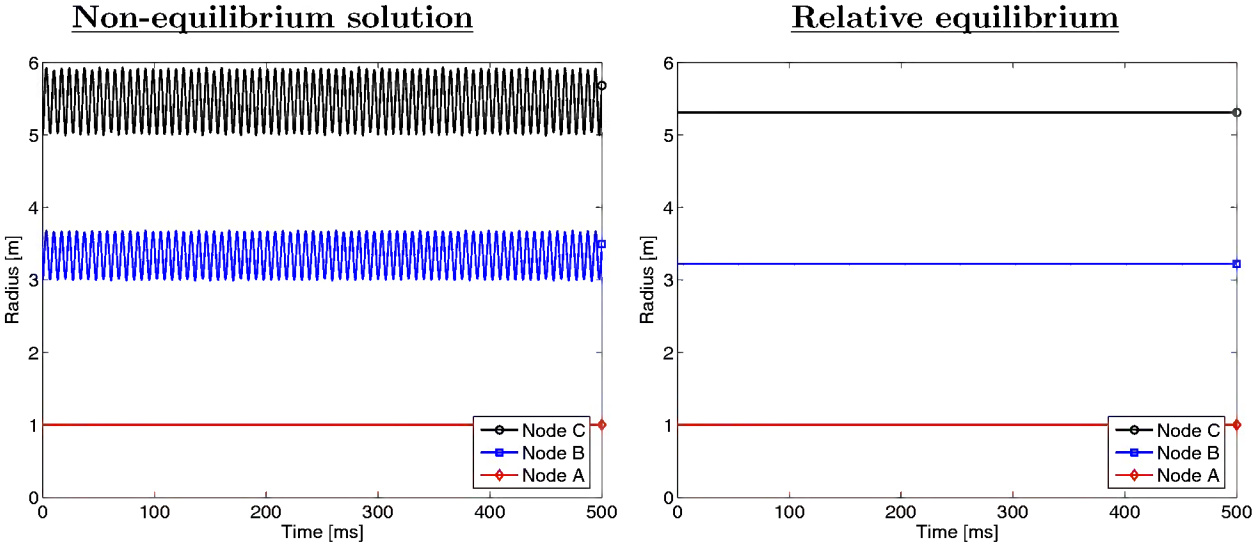

FIGURE II.5.9 Two-dimensional elastic solid in free flight. Evolution in time of the radius for nodes A, B and C (see Figure II.5.4) for the solutions starting from the undeformed configuration (left) and the relative equilibrium (right), both for the same initial angular velocity $\Omega = 0.230\ rad/ms$ ($\Delta t = 0.5\ ms$).

of convergence also affect fully energy conserving formulations (although they are observed to fail to converge at a later time), being a direct consequence of the high numerical stiffness of the problem. We refer to ARMERO & ROMERO [2001a], ARMERO & ROMERO [2001b] for a complete discussion of this issue as well as the formulation of EDMC time-stepping algorithms that exhibit the controllable high-frequency energy dissipation required to handle these situations. Briefly, this is accomplished with a modified stress formula (II.3.20), so the new stress approximation $\boldsymbol{S}_*$ satisfies the energy relation

$$\boldsymbol{S}_* : \frac{1}{2}\Delta\overline{\boldsymbol{C}} = \Delta W + \mathcal{D}_{num} \ , \tag{II.5.4}$$

for the numerical dissipation $\mathcal{D}_{num} \geq 0$, affecting the high-frequency response without perturbing the momentum conservation properties, being rigorously non-negative and fully controllable (i.e. $\mathcal{D}_{num} = 0$ is an option, recovering the original fully energy conserving approximation as a particular case). The important fact for the discussion here is that the B-bar operator still needs to satisfy the relation (II.3.16) for the numerical dissipation $\mathcal{D}_{num}$ in (II.5.4) to appear in the global energy evolution equation, and hence for the scheme to be rigorously energy dissipative (conservative as a particular case). Therefore, the consideration of these EDMC schemes requires also the use of the new conserving B-bar operator developed in this paper with the basic operator (II.4.4) still prone to exhibit numerical instabilities. The original references ARMERO & ROMERO [2001a], ARMERO & ROMERO [2001b] considered only displacement based finite element formulations, which do satisfy these conditions as discussed above but lead to locking elements.

To complete the confirmation of Proposition I.3.1, we study the conservation of relative equilibria for the problem at hand. To this purpose, we solve the relative equilibrium equation (II.3.12), obtaining the equilibrium deformation $\boldsymbol{\varphi}_e^h(\boldsymbol{X})$ for a given angular velocity Ω_e. Since this deformation is defined up to a translation and a rotation, and given the symmetry in the motions considered here (with the center of mass remaining fixed at the origin), the boundary conditions imposed while solving this equation consist of fixing the node at this center and the transversal displacement of Node C (see Figure II.5.4) at the tip of an arm (transversal to the axis of the arm), hence fixing the free rigid rotation.

We then compute the dynamic solution with the initial conditions defined by the computed equilibrium deformation (i.e. $\boldsymbol{x}^A(0) = \boldsymbol{\varphi}_e^h(\boldsymbol{X}^A)$) and the velocity distribution (II.5.3) for the equilibrium angular velocity Ω_e based on this equilibrium configuration. If the relative equilibria are preserved, the group motion given by the solution (II.3.9), corresponding to a rigid rotation in the deformed configuration $\boldsymbol{\varphi}_e^h(\boldsymbol{X})$ with a constant angular velocity Ω_e (note that $\boldsymbol{v}_e = 0$, i.e., no translation), must be recovered.

The new B-bar operator does obtain this solution, hence confirming the analyses leading to Proposition I.3.1. Figure II.5.8 depicts the solution obtained in this case with an angular velocity $\Omega_e = 0.230\, rad/ms$ ($\Delta t = 0.5\, ms$). The deformation at $t = 0\, ms$ shows the computed equilibrium configuration $\boldsymbol{\varphi}_e^h(\boldsymbol{X})$ with the distribution of the Mises (Cauchy)

stress in the arms; see Section II.5.1. The same configuration, with the very same stress distribution, is obtained at later times but rotated. The purely rigid rotational character of this motion is also confirmed by the plots in Figure II.5.9, showing the evolution in time of the radial coordinate from the center of the rigid core of Nodes A, B and C along the arms; see Figure II.5.4. These radii remain constant at all times at the initial value corresponding the initial deformed configuration $\boldsymbol{\varphi}_e^h(\boldsymbol{X})$. Note that these radii do not correspond to the values in the initial undeformed configuration, except for Node A since this node is on the rigid central core.

To illustrate better this equilibrium solution, we have included in Figure II.5.9 the radii of the same nodes for the dynamic solution depicted in Figure II.5.5. In contrast with the equilibrium solution, this non-equilibrium solution starts from the undeformed configuration shown in Figure II.5.4. The same initial angular velocity of $\Omega_e = 0.230\ rad/ms$ has been considered in both cases. The variation of these radii illustrate the non-equilibrium character of this solution in contrast with the solution depicted in Figure II.5.8. Note again that Node A is on the rigid central core. We also note that these two solutions, although defined by the same initial angular velocity, correspond to different angular momentum and energy, both conserved in the equilibrium and non-equilibrium solutions but different given the initial conditions for each.

II.5.3. Three-dimensional solid in free flight: evaluation of the conservation/ dissipation properties in time for the elastoplastic case

The purpose of this last numerical example is to evaluate the conservation properties in time of the formulation developed in this paper in the context of elastoplastic problems and in the three-dimensional case. As noted above, elastoplastic problems are of particular interest since the isochoric plastic flow in typical applications involving plastic models like J_2-flow theory leads effectively to quasi-incompressible problems, thus requiring special locking-free finite element interpolations as developed in this paper. We also consider a three-dimensional problem in contrast with the plane problem of the previous section. In this way, we consider the assumed strain brick Q1/A0 consisting of a trilinear interpolation of the displacement with a piece-wise constant volume over the element. The standard $2 \times 2 \times 2$ Gauss quadrature is considered in the evaluation of all the element arrays.

The solid under consideration consists of a stiff heavy inner ring with three equally spaced flexible arms in the configuration depicted in Figure II.5.10. Details of the geometric dimensions are shown in this figure. The flexible arms follow a finite strain elastoplastic model of J_2-flow theory based on a multiplicative decomposition of the deformation gradient $\boldsymbol{F} = \boldsymbol{F}^e\boldsymbol{F}^p$. Briefly, we consider the plastic evolution equations (II.2.10)-(II.2.13) for the von Mises yield function

$$\phi = \|\text{dev}\,[\boldsymbol{\tau}]\,\| - \sqrt{\frac{2}{3}}\,y(\alpha) \leq 0\,, \tag{II.5.5}$$

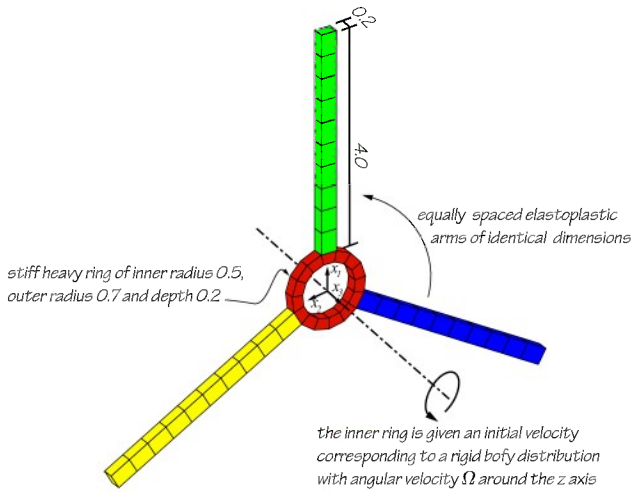

FIGURE II.5.10 Three-dimensional solid in free flight. Problem definition: geometry and initial conditions. Distances in m.

for the Kirchhoff stress $\boldsymbol{\tau} := \boldsymbol{F}^e \widetilde{\boldsymbol{S}} \boldsymbol{F}^{e^T}$, its (spatial) deviatoric part $\mathrm{dev}\,[\boldsymbol{\tau}]$ and the corresponding Euclidean tensor norm (i.e. $\|\boldsymbol{A}\|^2 := \boldsymbol{A} : \boldsymbol{A}$), with the plastic flow vectors

$$\boldsymbol{N}_\phi = \left.\frac{\partial \phi}{\partial \widetilde{\boldsymbol{S}}}\right|_{q,\boldsymbol{C}^e} = \boldsymbol{F}^e \frac{\mathrm{dev}\,[\boldsymbol{\tau}]}{\|\mathrm{dev}\,[\boldsymbol{\tau}]} \boldsymbol{F}^{e^T} , \qquad n_\phi = \left.\frac{\partial \phi}{\partial q}\right|_{\widetilde{\boldsymbol{S}},\boldsymbol{C}^e} = \sqrt{\frac{2}{3}} \qquad \text{and} \qquad \boldsymbol{M}_{W^p} = 0 , \tag{II.5.6}$$

(that is, an associated plastic model with no plastic spin), after noting that we have

$$\|\mathrm{dev}\,[\boldsymbol{\tau}]\,\|^2 = \boldsymbol{C}^e \mathrm{DEV}_{C^{e^{-1}}}\left[\widetilde{\boldsymbol{S}}\right] : \mathrm{DEV}_{C^{e^{-1}}}\left[\widetilde{\boldsymbol{S}}\right] \boldsymbol{C}^e , \tag{II.5.7}$$

for

$$\mathrm{DEV}_{C^{e^{-1}}}\left[\widetilde{\boldsymbol{S}}\right] := \widetilde{\boldsymbol{S}} - \frac{1}{3}\left(\widetilde{\boldsymbol{S}} : \boldsymbol{C}^e\right) \boldsymbol{C}^{e^{-1}} = \boldsymbol{F}^e \mathrm{dev}\,[\boldsymbol{\tau}]\, \boldsymbol{F}^{e^T} , \tag{II.5.8}$$

thus confirming the assumed functional dependence for the yield function (II.5.5) and flow vectors (II.5.6). The linear isotropic hardening law

$$y(\alpha) = \sigma_y + H\ \alpha , \tag{II.5.9}$$

and corresponding hardening potential $\mathcal{H}(\alpha) = H\ \alpha^2/2$ (so $q = -\partial\mathcal{H}/\partial\alpha = -H\alpha = \sigma_y - y(\alpha)$), for the initial uniaxial yield limit σ_y and linear hardening modulus H, has been assumed.

The elastic part (II.2.9) is defined by the Hencky's hyperelastic potential

$$W^e(\boldsymbol{C}^e) = \frac{\Lambda}{2}(\ln J^e)^2 + \frac{\mu}{4}\|\ln \boldsymbol{C}^e\|^2 , \tag{II.5.10}$$

for the elastic right Cauchy-Green tensor $\boldsymbol{C}^e = \boldsymbol{F}^{e^T} \boldsymbol{F}^e$, the elastic Jacobian $J^e = \det \boldsymbol{F}^e$, and the Lamé constants Λ and μ as in the previous section. Table II.5.3 includes the

TABLE II.5.3 Three dimensional solid in free-flight. Material parameters for the elastoplastic outer arms.

Young modulus	E	10 GPa
Poisson ratio	ν	0.2
Initial uniaxial yield limit	σ_y	975 GPa
Linear hardening modulus	H	200 MPa
Reference density	ρ_o	$2.0{\cdot}10^3$ kg/m^3

material parameters assumed for the arms. The inner ring is stiff and heavy, following the elastic Hencky's model (II.5.10) with a reference Young modulus 100 E_{arms} and reference density 10 ρ_o of the corresponding values for the arms, and with the same Poisson ratio of $\nu = 0.2$.

We refer to ARMERO [2006], ARMERO & ZAMBRANA [2007] and references therein for complete details on the elastoplastic model and the development of EDMC return mapping algorithms for their integration. In particular, we consider the EDMC return mapping algorithm developed in ARMERO [2006], and outlined above, in combination with the invariant stress formula (II.3.20) in terms of the elastic Cauchy-Green tensor $\boldsymbol{C}^e$ for the evaluation of the stresses (II.2.9) in its elastic part. The resulting global time-stepping algorithms show the exact plastic dissipation (including exact energy conservation in elastic steps) and the exact conservation laws of linear and angular momenta. The successful extension of these conservation/dissipation properties to the assumed strain elements needed for finite element simulations of problems considering this type of plastic model requires the developments presented in the current paper. We also note that, even though we present results here for the particular model given by (II.5.5)-(II.5.10), the algorithms considered here are completely general, with formulas like (II.3.20) and (II.3.17)-(II.3.19), applying to general isotropic or anisotropic models, associated or even non-associated plastic models. As noted in above, it is precisely the flexibility in handling different material models that motivates the development of the assumed strain framework considered here.

The simulations are started by considering the initial velocity given by the rigid-body distribution (II.5.3), in terms of the angular velocity Ω around the axis of symmetry $\boldsymbol{e}_3$ shown in Figure II.5.10, for *the inner ring only*. No loading or boundary conditions are imposed, thus leading to the free-flight of the solid in later times. In these conditions, the three components of both the linear and angular momenta are conserved as it is the total energy for elastic cases. A positive energy dissipation is to be observed if the plastic response of the arms is activated.

To illustrate the fully conserving properties in the elastic case in the considered three-dimensional setting, we first consider an initial angular velocity of $\Omega = 0.100$ rad/ms , which leads to a fully elastic response. The computed solution for a constant time step of

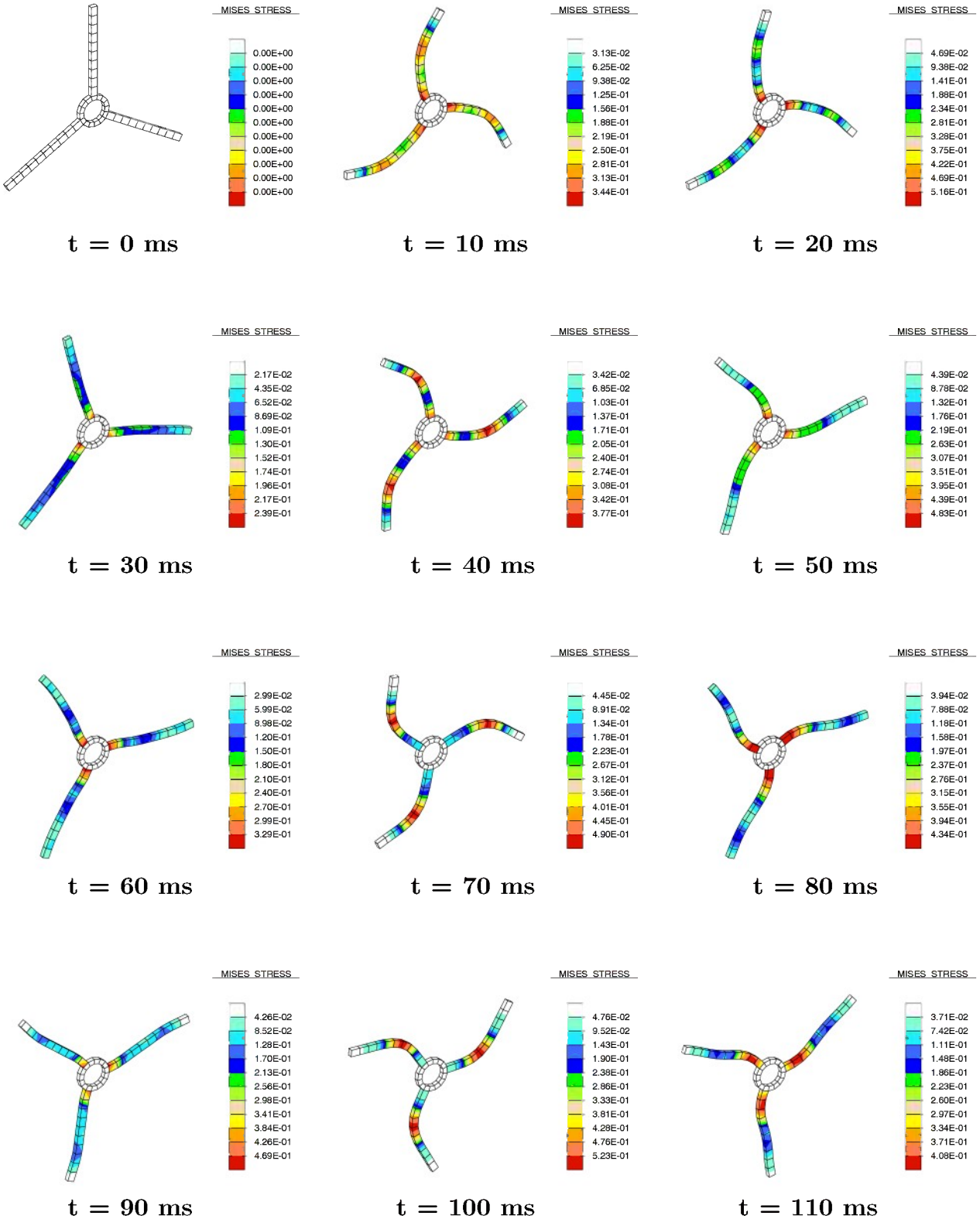

FIGURE II.5.11 Three-dimensional solid in free flight: solution for an angular velocity $\Omega = 0.100\ rad/ms$ leading to a purely elastic response of the solid. The distribution of the Mises (Cauchy) stress (in GPa) in the arms is shown superimposed to the solid's deformed configuration at different times.

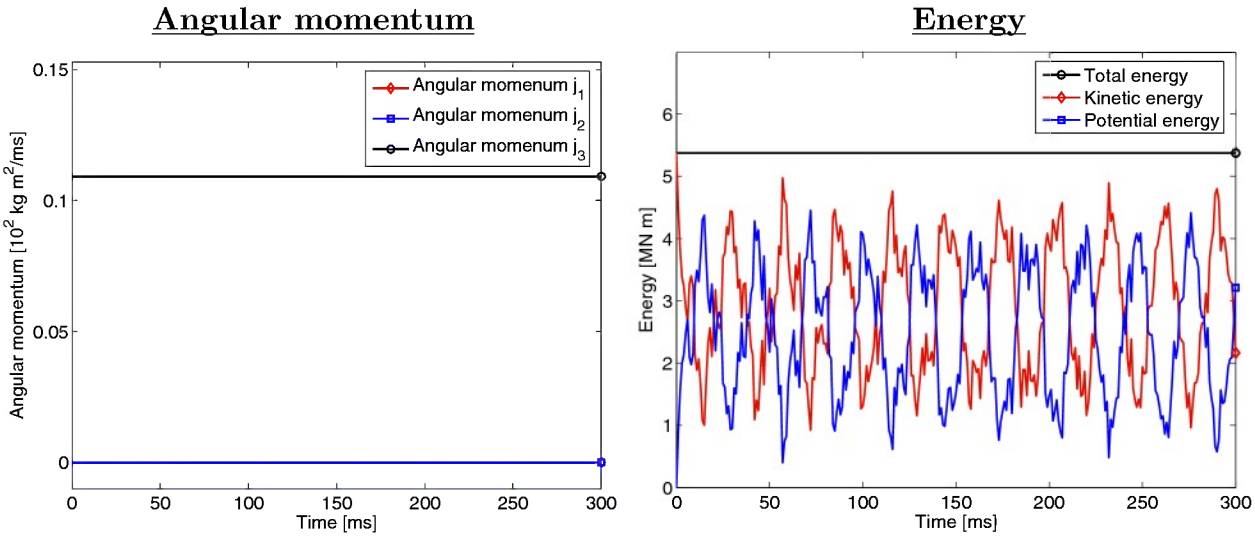

FIGURE II.5.12 Three-dimensional solid in free flight: solution for an angular velocity $\Omega = 0.100\ rad/ms$ leading to a purely elastic response of the solid. Evolution in time of the angular momentum components (left) and total energy (right) computed with the new conserving assumed strain finite element in combination with an energy-momentum conserving time-stepping scheme. The exact conservation of the total energy and the three components of the angular momentum is to be noted.

$\Delta t = 1.0\ ms$ is depicted in Figure II.5.11. The distribution of the Mises stress in the arms is again shown over the deformed configuration of the whole solid for different times. No activation of the plastic response is observed for these initial conditions, thus expecting a full conservation of the total energy. This conservation property is confirmed by the evolution plots shown in Figure II.5.12. The potential and kinetic energies are shown as they vary in time with their sum (the total energy) being exactly constant during the simulation. Figure II.5.12 shows also the evolution of the three components of the angular momentum $\boldsymbol{j}^h$, confirming again its exact conservation at all times. Note that, for the considered initial condition, the only non-zero component is the component j_3^h. The same situation applies to the linear momentum, not shown, with the three components vanishing given the assumed initial conditions ($\boldsymbol{l}^h = 0$).

The increase of the initial angular velocity to $\Omega = 0.200\ rad/ms$ leads to the solution depicted in Figure II.5.13. This initial velocity results in the development of plastic strains in the arms. Figure II.5.13 shows the distribution of the equivalent plastic strain α at different early stages of the motion. The large deformation and strains are to be noted. A constant time step of $\Delta t = 1.0\ ms$ has also been considered. Figure II.5.14 depicts the evolution of the total energy and the axial (non-zero) component of the angular momentum for this case. The exact conservation of the momentum is again obtained, with the total energy showing a strictly positive energy dissipation during plastic steps and exact conservation during elastic ones.

These results confirm the exact conservation properties of the assumed strain inter-

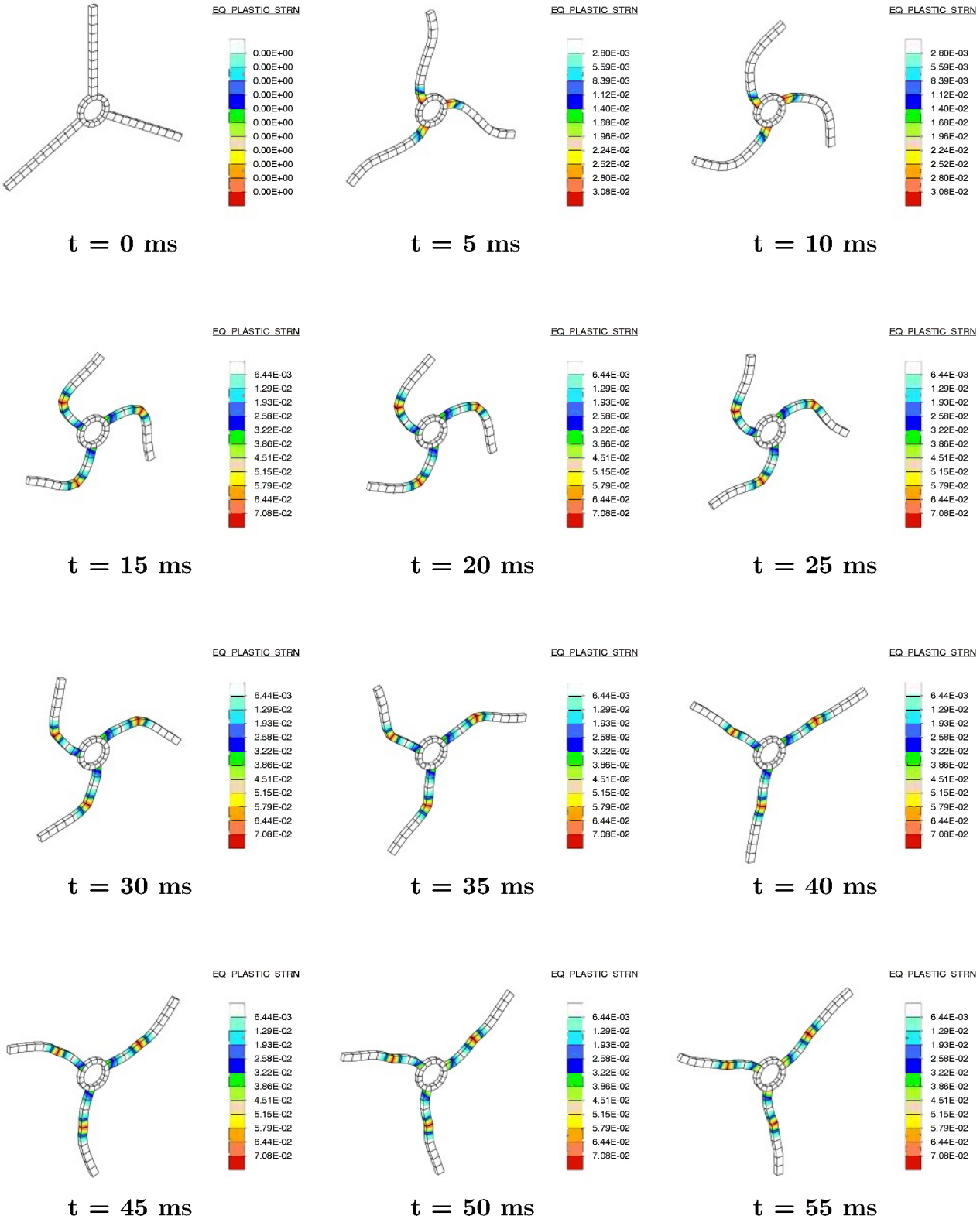

FIGURE II.5.13 Three-dimensional solid in free flight: early stages of the solution for an angular velocity $\Omega = 0.200\ rad/ms$ leading to an elastoplastic response of the solid. The distribution of the equivalent plastic strain is shown superimposed to the solid's deformed configuration at different times.

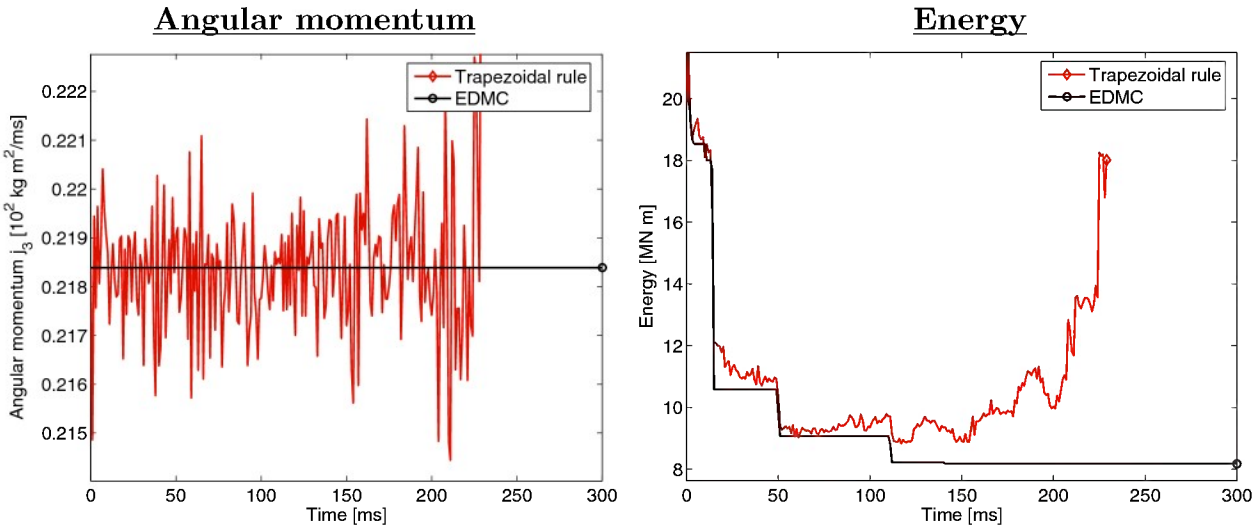

FIGURE II.5.14 Three-dimensional solid in free flight: solution for an angular velocity $\Omega = 0.200\ rad/ms$ leading to an elastoplastic response of the solid. Evolution in time of the angular momentum j_3^h (left) and total energy (right) for the new conserving assumed strain finite element in combination with an EDMC time-stepping scheme and the standard (non-conserving) assumed strain element with the classical trapezoidal rule. The latter exhibits an instability leading to the termination of the computation with a non-physical growth of the energy.

polations developed in this work in combination of EDMC time-stepping algorithms for the integration of the equations in time. This situation is to be contrasted with standard schemes currently available in the literature. As an illustration we have included in Figure II.5.14 the solution obtained with the classical trapezoidal rule (i.e. Newmark $\beta = 1/4$, $\gamma = 1/2$); see e.g. SIMO [1998] for an implementation in the finite strain plastic case of interest. In particular the simulation considers the exponential return mappings that can be found developed in this last reference. The spatial discretization considers the classical (non-conserving) B-bar approximation of Section (sub:NCBbar) evaluated at the end of the time step t_{n+1}, as required by this scheme. The lack of conservation/dissipation properties for both the angular momentum and energy become apparent in the solutions depicted in Figure II.5.14. In particular, we observe the nonlinear unstable character of the scheme as the unbounded growth of energy forces to stop the simulation at some time. The presence of this unphysical energy growth, even in the context of a dissipative elastoplastic as considered here, is to be noted and contrasted with the exact energy conservation/dissipation properties of the methods developed in this work.

II.6. Concluding remarks

We have presented in this appendix a new framework for the development of assumed strain finite elements for nearly incompressible problems in the finite deformation dynamic

range that preserves the conservation/dissipation properties in time of energy and momenta characteristic of recently developed energy-momentum and EDMC time-stepping algorithms. The proposed formulation relies on the proper definition of the linearized strain operator (or B-bar operator) accounting not only for the spatial interpolations but also for the temporal approximation of the governing equations. Standard existing treatments, with the B-bar operator defined through the standard variation of the assumed strains, have been shown to destroy the energy conservation, thus leading to difficulties in the form of instabilities with an energy growth. After identifying the general conditions that this operator must satisfy to lead to conserving approximations of the energy, the linear and angular momenta and the associated relative equilibria, we have undertaken the formulation of actual finite elements for plane and three-dimensional problems. The conservation properties in time have been proven rigorously, and evaluated numerically with several representative simulations in nonlinear elastodynamics and dynamic finite strain plasticity, illustrating also the locking-free character of the final elements in the incompressible limit of interest.

A main advantage of the considered assumed strain framework is its flexibility in terms of the involved constitutive models. Indeed, the kinematic considerations defining the new B-bar operator are completely independent of the considered material model, this being elastic or inelastic, isotropic or anisotropic, with coupled or uncoupled volumetric and deviatoric parts. This situation is to be contrasted with the more involved implementation of mixed formulations for general models; see e.g. Simo et al [1988]. We have only addressed in this paper the case of volumetric locking, without considering shear locking. The latter is not as a severe problem for the type of problems considered in this paper, namely, continuum problems; see e.g. Armero [2000], Armero [2004]. However, the assumed strain methods developed here for the volume response can be combined with enhanced strain formulations to address shear locking, as developed in Armero [2000] for static problems. We are currently exploring these extensions for the dynamic problems of interest here.

References

Armero, F. [2000] "On the locking and stability of finite elements in finite deformation plane strain problems," Computers & Structures, 75:261-290.

Armero F [2004] "Assumed strain finite element methods," in Finite Element Methods: 1970's and beyond, ed. by LP Franca, TE Tezduyar and A Masud, CIMNE, Barcelona.

Armero, F. [2006] "Energy-dissipative momentum-conserving time-stepping algorithms for finite strain multiplicative plasticity," Comp. Meth. Appl. Mech. Eng., 195:4862-4889.

Armero, F. & Romero, I. [2001a] "On the formulation of high-frequency dissipative time-stepping algorithms for nonlinear dynamics. Part I: Low order methods for two model problems and nonlinear elastodynamics," Comp. Meth. Appl. Mech. Eng., 190:2603–2649.

Armero, F. & Romero, I. [2001b] "On the formulation of high-frequency dissipative time-stepping algorithms for nonlinear dynamics. Part II: High order methods," Comp. Meth. Appl. Mech. Eng., 190:6783–6824.

Armero, F. & Romero, I. [2003] "Energy-dissipative momentum-conserving time-stepping algorithms for the dynamics of nonlinear Cosserat rods," Comp. Mech., 31:3–26.

Armero, F. & Zambrana, C. [2007] "Volume–preserving energy–dissipative momentum–conserving algorithms for isochoric multiplicative plasticity," Comp. Meth. Appl. Mech. Eng., 196:4130-4159.

Crisfield, M. & Shi, J. [1994] "A co-rotational element/time-integration strategy for non-linear dynamics," Int. J. Num. Meth. Eng., 37:1897-1913.

González, O. [2000] "Exact energy-momentum conserving algorithms for general models in nonlinear elasticity," Comp. Meth. Appl. Mech. Eng., 190:1763–1783.

Hughes, T.J.R. [1980] "Generalization of selective integration procedures to anisotropic and nonlinear media," Int. J. Num. Meth. Eng., 15:1413–1418.

Hughes TJR [1987] The Finite Element Method,, Prentice-Hall.

Marsden, J.E. [1992] Lectures on Mechanics, London Mathematical Society Lecture Note Series, 174: Cambridge University Press.

Meng, X.N. & Laursen, T.A. [2002] "Energy consistent algorithms for dynamic finite deformation plasticity," Comp. Meth. Appl. Mech. Eng., 191:1639-1675.

Nagtegaal, J.C.; Parks, D.M & Rice, J.R. [1974] "On numerically accurate finite element solutions in the fully plastic range," Comp. Meth. Appl. Mech. Eng., 4:153–177.

Noels, L.; Stainier, L. & Ponthot, J.P. [2004] "An Energy-Momentum Conserving Algorithm for Non-Linear Hypoelastic Constitutive Models," Int. J. Num. Meth. Eng., 59:83–114.

Romero, I. & Armero, F. [2002] "Numerical integration of the stiff dynamics of geometrically exact shells: an energy-dissipative momentum-conserving scheme," Int. J. Num. Meth. Eng., 54:1043–1086.

Simo JC [1998] "Numerical Analysis of Classical Plasticity," Handbook for Numerical Analysis, Volume VI, ed. by P.G. Ciarlet and J.J. Lions, Elsevier, Amsterdam.

Simo, J.C. & Tarnow, N. [1992] "The discrete energy–momentum method. conserving algorithms for nonlinear elastodynamics," ZAMP, 43:757-793.

Simo, J.C.; Posbergh, T.A. & Marsden, J.E. [1991] "Stability of relative equilibria. Part II: Application to nonlinear elasticity," Arch. Rational Mech. Anal., 115:61-100.

Simo, J.C.; Taylor, R.L. & Pister, K. [1988] "Variational and projection methods for the volume constraint in finite deformation elastoplasticity," Comp. Meth. Appl. Mech. Eng., 57:177-208.